Lost in a Crowd: Observations of Single DNA Knots and Single Mammalian Cells

Thesis by

Xiaoyan Robert Bao

In Partial Fulfillment of the Requirements

for the Degree of

Doctor of Philosophy

California Institute of Technology

Pasadena, California

2007

(Defended March 19, 2007)

This thesis is dedicated to my parents,

to my mentors, Steve Quake and Mel Simon,

to the other people in lab, especially the postdocs, who, really, taught me all the nuts and bolts of putting together an experiment and making it work,

and to all the other friends along the way who made the journey so much fun.

Acknowledgements

I worked together with Heun Jin Lee on the knots project. He put all the instrumentation in place to perform the experiments, and throughout the experiment taught me to think and work systematically and effectively. I could have avoided many pitfalls and delays in that and subsequent experiments, had I followed his advice more diligently.

Alex Groisman and Keith Matthews did some preliminary work on the knots project. In particular, Alex suggested the use of high-molecular weight PEG to increase viscosity without changing refraction index and also provided the initial oxygen scavenging recipe; the idea to use servo motors to control the optical elements was Keith's.

Theoretical predictions of knot sizes for the 7_1 knot, not published elsewhere, were kindly provided by Pietro Pieranski. He, Andrjez Stasiak, Doug Smith, Mei Wang, and Julius Su provided other helpful suggestions in the knots project.

Members of the Quake group who taught me the art and craft of microfluidics included Emil Kartalov and Carl Hansen. The use of constrictions to control shear stress was suggested by Mike Diehl.

All the biology for the signaling project was done in Mel Simon's lab, and I'd like to thank lab members Iain Fraser, Misook Chang, Adrienne Driver (now at Truman College, Chicago), Jamie Liu, Bally Randhawa, Leah Santat, Estelle Wall, Joelle Zavzavadjian, and Xiaocui Zhu for all their help and friendship.

Finally, I want to acknowledge the Fannie and John Hertz Foundation, who generously financed my graduate studies. I greatly valued the yearly interviews with Lowell Wood and the Foundation-sponsored events where I was able to meet other Fellows.

Abstract

The overarching theme for the two main experiments presented here is that standard biochemical and cell biological techniques, which use macroscopic samples and hence average over large numbers of things, be they molecules or cells, tend to smear out interesting phenomena that occur to a small fraction of those things. Averaging also collapses the entire population distribution into one single value, and furthermore prevents tracking properties of individuals over the lifetime of the experiment. Thus, observing molecules and cells singly provides much more insight into their behavior. The first project described here involves mechanically tying knots into linear DNA molecules stretched out between optically trapped beads. Without mechanical intervention, the molecules we used contained knots only rarely, and those knots are expected to involve small portions of the DNA contour and hence give only small perturbations to the overall polymer dynamics. By tying and observing them singly, we were able to show that, while knots collapse and tighten under tension, even the most complex ones we tied retained mobility to quite a surprising degree. The observed knot sizes and mobilities correlated well with theoretical predictions for knots in ideal ropes of finite thickness, indicating that even under high tension the different parts of the molecular knots are kept away from each other because of electrostatic repulsion. The differences between knots of different topologies, both in size and speed, open up the possibility that, with further refinement, this approach may allow

us to observe the stepwise actions of single topoisomerases in chemically undoing complex knots. The second project was to develop a microfluidic system to perform many signaling experiments on cells simultaneously within a single field-of-view of a microscope. Single cell sensitivity has been pivotal both in verifying data quality and in understanding cell-to-cell variabilities in signaling strengths. In the course of these two projects I also had a few side ideas which, sadly, I wasn't able to develop to the degree that I would have liked. I've included them as minor digressions, in the hopes that someone will see them and find them useful.

Contents

List of Figures

Part I

DNA knots

Chapter 1

Introduction

Knots and braids have fascinated observers since ancient times; complex topological designs have been preserved on tiles and pottery dating back thousands of years [1]. Kelvin and Tait undertook the first systematic study of knots in the 19th century [2, 3], and in the 20th century a powerful mathematical framework was constructed to classify knots according to various topological invariants [4]. They appear in many different scientific contexts, ranging from the synthesis of topologically non-trivial molecules in chemistry [5] to the role of topology in life itself: topoisomerase enzymes exist to measure and change the topology of DNA. In physics, it was realized quite some time ago that there is a deep connection between knot invariants and theories of statistical mechanics [6]. Knots also appear naturally in long polymers [7]; they are in fact the generic state and can profoundly impact the dynamics of systems in which they appear [8, 9]. The magnitude of these effects depends strongly on the complexity of the knot [10]. Such polymeric topological constraints arise naturally in cells during DNA replication [11], and knotting in particular has been important in elucidating the mechanisms of DNA recombination [12].

Theoretical and numerical studies of knots in long polymers suggest that they are localized, i.e., the amount of polymer directly engaged within the knot is vanishingly small compared to the total length of the polymer [13, 14]. Distributions of knots have previously been synthesized in bulk samples [15, 16], but only in relatively short circular DNA molecules; in this limit the knots are neither localized nor tightly constrained, and indeed they were purified and characterized based upon their effects on the properties of the polymer as a whole. We sought instead to confine the knot and study it as an isolated object. By mechanically knotting linear pieces of DNA with beads at the ends that act as handles for optical tweezers, we were able to keep the DNA under a fixed tension, making the knot a localized structure whose properties are independent of the length of substrate DNA. The confinement of DNA achievable under these conditions allows comparison to models of polymer dynamics, as well as more specific theoretical results for ideal tight knots. The results presented here have been published [17].

Chapter 2

Sample preparation

2.1 Putting handles onto DNA ends

Because DNA is so thin (hydrodynamic diameter $\simeq$ 2 nm), it is essentially impossible to trap optically when extended (but see [18]). Handles, typically plastic or silica beads, must be attached to the DNA to allow its manipulation with optical traps. Here I will cover the biochemistry involved in preparing the bead-DNA-bead ”dumbbells” used in knot tying.

We used λ phage genomic DNA because it has a known sequence; its length distribution is monodisperse when the DNA is undamaged; it has overhangs at either end which facilitate modification; and because it can be obtained in fairly high quantities, fairly cheaply. The λ phage genome is 48,502 base pairs long, with two 12-base overhangs at either end that complement each other. Once injected into its host cell, the phage genome is circularized via annealing at the hybridized overhangs, and the single-strand breaks joined by ligases in the host cytoplasm. When the phage decides to lyse its host [19], the circularization facilitates massive replication of the genome [20] in preparation for new virus production and lysis.

For our purposes, the unannealed, cohesive ends are great targets for labeling with modified nucleotides [21], to which handles may then be bound. Briefly, the left side cohesive overhang in λ phage has the sequence GGGCGGCGACCT, with the corresponding right side cohesive overhang sequence AGGTCGCCGCCC (the GGG and AGG are at the DNA strand ends). Substituting a modified dUTP for dTTP in a DNA polymerase reaction allows us to specifically label the DNA at ”T” bases. Withholding dCTP from the reaction prevents incorporation of labeled dUTP on the right side while, with sufficient incubation, allowing for complete labeling in the left side, so that a subsequent reaction with a full set of nucleotides will be able to label the right side without labeling the left side. In this way, we can specifically label the left side with biotin and the right side with digoxigenin. In the cases where differential labeling is not necessary, we can simply omit the first polymerase reaction.

Beads could be attached to the DNA ends simply by mixing the DNA and beads together — beads coated with anti-digoxigenin bind to the digoxigenin-labeled end, and beads coated with streptavidin bind to the biotin-labeled end. The original rationale for differentially labeling the two ends of the DNA molecule was to prevent both ends of the molecule from binding to the same bead. With single-length λ molecules this was a serious problem, since the distance between the two ends of the molecule is only expected to be about 1 μm, so that binding sites on the bead that one end of a DNA molecule has already bound would always outcompete binding sites on other beads. For longer DNA molecules (see below), though, this became less of a problem, especially as we started to also increase the bead concentration. In this case we could simply do without the digoxigenin labeling and only rely on binding of streptavidin to biotin to attach beads to the DNA ends. In addition to simplifying the DNA synthesis protocol, the elimination of digoxigenin also gave rise to more reliable dumbbell syntheses, as we were never able to find a source of antibody-coated beads with the same binding efficiency and monodispersity as streptavidin-coated beads from Bangs Labs. Finally, the anti-digoxigenin linkage to digoxigenin seemed to have a propensity for falling off under tension. We associated it to instability of the antibodies, which are held together partially by disulfide bridges, in the strongly reducing observation environment (see §2.3.3).

2.2 Longer DNA

As described in §3.3, tying DNA into a knot simply entails making a loop with it and then threading that loop with one end, but our initial attempts to tie knots with λ DNA appeared quite unsuccessful. Because DNA is an entropic polymer, keeping it in an extended conformation meant applying tension. That tension, however, would also act to close off any loops formed in the DNA. We therefore had too short a time window within which to tie the knot after making the loop. We were already increasing the viscosity of the solution in which the knot was to be tied with poly(ethylene glycol), hoping thereby to slow down the loop decay (§2.3.3). Increasing the viscosity of the solution further would neither help nor hurt with the loop decay problem: the same viscosity that slows down loop formation also limits the speed at which the trap may be moved without losing the trapped bead, since the trap can only exert a finite amount of force (§4.1).

The best way to buy time to thread the loop, we reasoned, was to increase the length of DNA being tied. The added length would allow us to make a larger loop to thread; that larger loop would also take longer to decay away. We noted that the cohesive ends of the DNA allow easy concatemerization of λ DNA to yield longer length molecules, while at the same time allowing us to retain the biochemistry involved in linking the DNA to beads. To generate concatemers, we simply ran a standard DNA ligation reaction on a solution of

λ DNA where intermolecular end annealing outcompeted intermolecular end annealing.

To estimate the concentration needed, let's assume that the DNA molecule is a Gaussian chain of n segments, length b, with minimal excluded volume effects, as in the Rouse model. The end-to-end vector distribution $\rho(\mathbf{r})$ is then Gaussian [22] with mean square magnitude $\left\langle R^2 \right\rangle = nb^2$:

$$\rho(\mathbf{r}) = \left(\frac{3}{2\pi n b^2} \right)^{3/2} \exp\left[-\frac{3r^2}{2nb^2} \right] \tag{2.1}$$

which immediately gives the intermolecular end concentration of $c = \left(2\pi n b^2/3\right)^{-3/2}$. For λ phage, where b = 55 nm and $n \simeq 311$, we have $c \simeq 4.0 \times 10^{14} \mathrm{L}^{-1}$, or 20 mg/L. The λ stock solutions available from commercial vendors all have concentrations in the vicinity of 500 mg/L, which assures a low circularization background in the concatemerization reaction.

Initial experiments using a ligation temperature of 16°C, recommended by the manufacturer, yielded rather poor quality dumbbells. More often than not, beads were found bound not only to the ends of the DNA molecules but also in the middle of the molecules.

We wondered if this was due to internal labeling of the concatemerized DNA molecules. To end-label the DNA, we were using the Klenow fragment of *E. coli* polymerase (see §2.3.1), which adds nucleotides in a template-dependent manner to the 3′ end of single DNA strands hybridized to a longer template. This includes both overhangs and internal single-strand breaks. We realized that the temperature of 16°C recommended for ligation was to promote annealing of the typical 4 bp overhangs generated by restriction endonucleases; in our case, the overhang is 12 bp, meaning that at the low temperature used most of our overhangs were already annealed by the time the ligase arrived and sealed the nicks. The rate-limiting step, then, would be the ligation reaction itself, so that ligation at one of the Watson-Crick strands would not necessarily be correlated with ligation at the

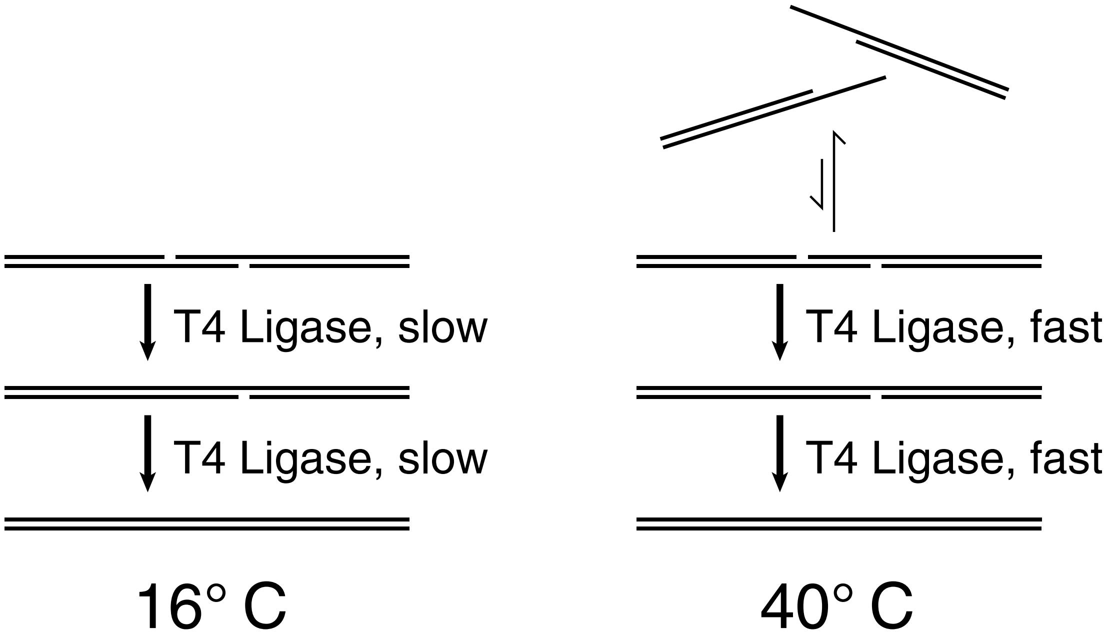

Figure 2.1: Rationale behind running the λ ligation reaction at higher temperatures. At 16°C, most of the cohesive ends are annealed already, so that the rate-limiting reaction is the ligation itself. This means that the ligation states of the two adjacent nicks at an annealed cohesive end are uncorrelated, so that the ligation reaction yields products with internal nicks. At 40°C, on the other hand, the activity of the ligase enzyme is much higher, but the enzyme lacks substrate since the cohesive ends are usually melted. The annealing of ends thus becomes limiting, and once this happens the nicks in both strands get ligated very quickly, so that the probability of having a product with an internal nick is much lower.

other. Since ligation in only one strand would be enough to join two molecules, this would have the effect of leaving nicks at incompletely joined cohesive ends. To change this, we performed the ligation reaction at a higher temperature, so that (a) the ligase activity was much higher, and (b) the proportion of cohesive ends that was annealed was much lower. The rate-limiting reaction now became the annealing of the cohesive ends; once that happened, the ligation of the nicks on the two strands should occur in quick succession (see fig. 2.1).

I'll note here that, in retrospect, the choice of T4 DNA ligase was probably not the best: its substrate specificity is much poorer than *E. coli* DNA ligase, and it will catalyze the joining of blunt DNA ends, though at much lower rates [23]. This gives dirtier ligation products and shows up in lower yields of ”clean” dumbbells. The presence, at low frequency, of ”stuck” fragments of DNA attached to otherwise good dumbbells (see fig. 5.1) probably arises from this specificity problem. Future experiments in this direction should probably use some other ligase.

2.3 Final sample preparation protocol

2.3.1 DNA synthesis

Start with 36 μl of 0.5 mg/ml λ phage DNA in a large Eppendorf tube. Incubate at 75°C, 10 min.

Ligation: Ice the tube. Add 4 μl 10x Ligation buffer, and 2 μl T4 DNA Ligase (New England Biolabs cat. #M0202S) that has been diluted 1:100. Mix well by pipetting up and down (slowly) 8-10 times with a wide-mouth pipette and a pipetteman set at 20 μl.

Incubate at 40 °C, 18 min, to ligate.

Heat to 70 °C, 10 min, to inactivate enzyme.

Ice, 4 min.

End labeling: Add 2 μl 100 mM DTT, 2.5 μl ea: dATP, dGTP, dCTP, and biotin-dUTP (all 1 mM), 20 μl water, and 2 μl Klenow (exo-). Mix well by pipetting up and down (slowly) 8-10 times with a wide-mouth pipette and a pipetteman set at 40 μl.

For end labeling without an initial ligation step, add 8 μl 10x EcoPol buffer instead of 2 μl 100 mM DTT.

Incubate at 37 °C, 20 min.

Heat to 70 °C, 10 min.

Put in ice, 4 min.

Dialysis: While the DNA is iced, take a petri dish and cover the bottom with TNE (10 mM Tris, 10 mM $NaCl_2$, 1 mM EDTA).

When the DNA is done icing, place a Millipore filter disc in the petri dish, being careful to have the shiny side up and not get any buffer on that side. Carefully pipette the DNA onto the filter disc, taking care to prevent the droplet from merging with the buffer.

Put lid on petri dish, and let it sit 1-2 hrs.

Pipette the DNA solution off the filter disc and transfer to a 1.7 ml Eppendorf tube. Weigh the tube before and after to get the yield volume, which will be around 55 μl. Discard the buffer and petri dish.

This gives bio-poly-λ-bio. Dilute 10 μl of it into 90 μl of TNE and mix to get a good working concentration. Smaller volumes of DNA will be progressively harder to pipette.

2.3.2 Making dumbbells

Make TNE with Tween (TNE/tw): 2 μl of 10% tween-20 for every 1 ml of TNE buffer. This is to be made fresh each time.

Take 195 μl TNE/tw; add 15 μl streptavidin-coated beads (1 μm dia. polystyrene, 1% w/v, Bangs Labs).

Spin at 3 krpm in an Eppendorf 5415 C tabletop centrifuge, 6 min.

Pipette off 200 μl supernatant; add 200 μl TNE/tw; resuspend by vortexing.

Repeat twice; after last spin, add only 70 μl TNE/tw. Also add 20 μl desthiobiotin. Resuspend.

Incubate (rotating), 1 hr.

Wash twice, except resuspend to 16 μl at end of last wash. Add 2 μl of the 1:10 DNA, and mix immediately. Put on rotating tube rack.

Take aliquots (2 μl into 18 μl TNE/tw) after 1, 2, 6, 10, and 20 hours. Dilution of the bead-DNA mixture is sufficient to stop the binding reactions.

2.3.3 Sample slide preparation

Stain the dumbbells by diluting them into a mixture of 6% poly(ethylene glycol) (m.w. 35000, Polysciences) in 1×TNE, with 250 μg/ml α-casein, 0.1% tween-20, and 20 nM YOYO-1. Let sit, rotating, for at least 1 hr. Dilution volumes are to be determined empirically with each batch of dumbbells.

Meanwhile, use Sigmacote (Sigma-Aldrich) to make hydrophobic the surface of a plain glass slide. Let it dry. Also, make the oxygen scavenger cocktail: equal volumes of 113 mg/ml glucose, 50% (v/v) β-mercaptoethanol, 5 mg/ml glucose oxidase, and 0.9 mg/ml catalase.

After the dumbbells are finished staining, put an 11 μl droplet onto the center of the glass slide. Add 3 μl of the oxygen scavenging mix. Gently lay a glass cover slip (No. $1\frac{1}{2}$, 18 mm sq.) on top of the droplet, and seal with clear nail polish. Let the nail polish dry for about 10 min.

Chapter 3

Optical trapping

Optical trapping of objects in fluid relies on momentum transfer from a beam of light to an object that it impinges upon. Briefly, a laser beam of reasonable power (on the order of 1 W) is focused to a diffraction-limit spot. Polarizable objects interact with the light beam and are attracted to, and trapped by, the focal spot. This, then, lets us ″grab″ micron-sized objects with a light beam and then manipulate them. Typically, the same objective used to focus the laser is also used to image the object so trapped.

3.1 Operating principle

The theory behind optical trapping has been extensively covered elsewhere [24, 25], so I will only present it briefly and elaborate only when doing so relates to the use of optical trapping in biology.

There are commonly two different, complementary explanations as to why objects are attracted to the focus of a light beam. The first (fig. 3.1a) takes an electromagnetic fields approach. Consider a sphere of polarizability α sitting in some electric field $\vec{E}$. The field induces a dipole $\vec{p} = \alpha\vec{E}$ which interacts with the field to give rise to a favorable interaction energy $U = \vec{p} \cdot \vec{E} = \alpha E^2$. Now, static electric fields, by virtue of having to obey Laplace's

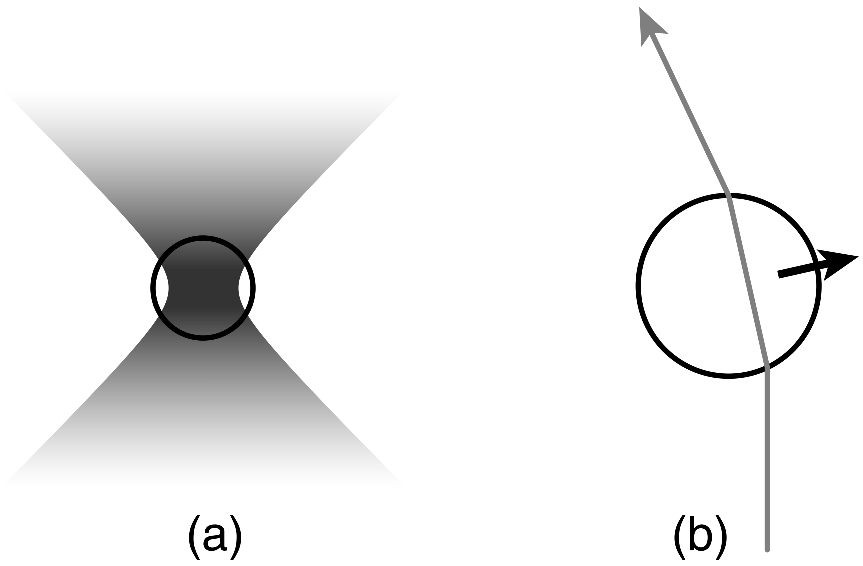

Figure 3.1: Explaining the ability to trap small particles with a beam of light. (a) The focus of a light beam is a region of highest time-averaged electric field strength, which attracts electrically polarizable material. (b) An individual ray in a light beam gets deflected by a refracting sphere in such a way that its momentum is changed. This change gives rise to a recoil force on the sphere which pushes it towards the center of the beam.

equation, cannot have any local extrema in field strength. However, oscillating electric fields can, and there is a strong time-averaged local maximum in field strength at the focus of a beam of light. Using a coherent laser beam allows us to generate a diffraction-limited focal spot which is thus able to trap particles with sizes on the order of 1 μm.

The second approach (fig. 3.1b) uses simple ray optics and considers a refracting sphere within, but offset from, a straight beam of light. The beam is deflected by the sphere in the same direction as the sphere's offset from the beam. Since each photon so deflected carries a momentum that is also deflected, the resulting recoil pushes the sphere back into the light beam. Note that this particular situation only confines the bead in two directions. At the center of an optical trap, however, different rays that converge at the focus confine the bead in different directions; confinement along the main beam direction is conferred by rays coming in from the sides.

This reasoning is for a particle trapped in vacuum. It still holds for a particle in water, with the modification that the index of refraction of the trapped particle should be higher than that of water; otherwise the particle will be repelled from the focus. In the fields approach, the analogous requirement is that the polarizability of the particle should be higher than that for water at the frequency of the trapping light. These requirements are identical, since the index of refraction n and dielectric constant ϵ are related by $n^2 = \epsilon\mu$, with the magnetic permeability μ pretty close to unity for most dielectric materials.

3.2 Instrument setup

To observe the DNA sample and form the optical traps, we used an oil-immersion Olympus PlanApo 60x objective (N.A. 1.4), infinity-corrected with a tube length of 180 mm. Since the objective is infinity-corrected, a collimated infrared beam will form an optical trap within the imaging plane.

3.2.1 Trap

Forming the optical trap is quite straightforward, but we wanted to have two traps, one for each end of the piece of DNA being observed, and we need to move at least one of the traps in all three dimensions. To generating a dual-beam trap with a single laser, we can simply decompose our laser beam source according to polarization with a polarizing beam splitter, manipulate the two resulting beams independently, and recombine them again using another polarizing beam splitter. Because our source laser is circularly polarized, we could form a linearly polarized laser beam of arbitrary polarization angle with a quarter-wave plate; this allows us to vary the proportion of laser power going to each trap. In the end, we were able to use another laser to form the second trap; combining the two beams

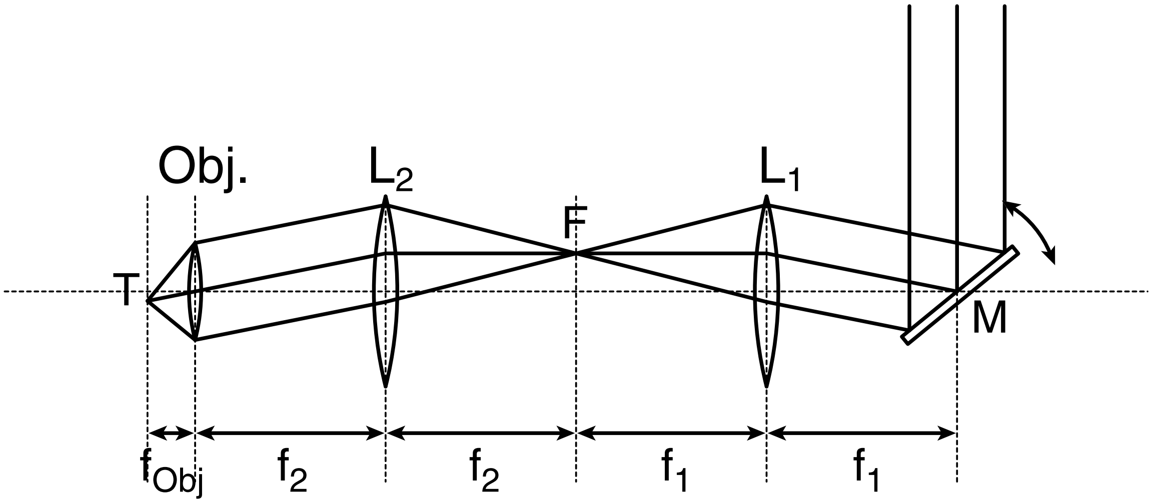

Figure 3.2: Mechanism for changing the position of the trap within the imaging plane. Briefly, the telescope formed by lenses L_1 and L_2 image the steerable mirror (M) onto the back focal plane of the objective. Changing the tip/tilt of the mirror (M) alters the incident tip/tilt of the beam into the objective, without steering the beam center away from it, thus moving the trap location within the imaging plane.

was again accomplished by the use of a polarizing beam splitter.

As for steering a given trap, we note that the incident angle of the beam determines the position of the focus within the plane. As is standard practice with optical traps, we used a lens pair to form a telescope imaging a mirror onto the back focal plane of the microscope objective (fig. 3.2). This way, the incident angle of the infrared beam into the objective can be adjusted without steering it away from the objective. Another way of understanding this is to think of lens L_2 and the objective as forming a telescope, imaging the focal point of the laser beam F into the imaging plane at trap location T. Since the mirror M is at the focus of lens L_1, changing its angle simply moves F in the transverse direction and hence moves T within the imaging plane. Thus, whereas f_1 and f_2 in fig. 3.2 are shown as being equal, they need not be so. Adjusting f_1, for instance, changes the lever arm over which rotation of M can act to move point F; this can be used to trade stability and precision for speed and range, or vice versa. Adjusting f_2 does likewise by changing the magnification of imaging F to T; it also changes the depth control (see below). Finally, the telescope formed by L_1 and L_2 will change the size of the laser beam impinging on the objective, and so will determine how much optical power makes it to the focus, and what distribution that power comes in.

Moving the trap in the depth direction turns out to be crucial in the ability to tie a knot; manipulating a trap in two dimensions does not allow for easy and consistent control over the topology of the DNA attached to the trapped bead. Again looking at the lens pair of the objective and L_2 as a telescope, we see that moving the trap T along the beam direction can be effected simply by moving F along the beam direction; this is easily accomplished by moving lens L_1 back and forth. While in principle this will couple into the steering within the imaging plane, in practice the effect is quite minimal; the effect can be further reduced by zooming the trap up and down only when it is in the center position, so that the beam never deviates from the optical axis.

Running through the lens equations, we obtain that motions of T along the optical axis get demagnified by a factor m^2, and motions of T perpendicular to that get demagnified by m, where $m = f_2/f_{\rm Obj}$ is just the telescope magnification. Thus, for $f_{\rm Obj} = 3$ mm and $f_2 = 150$ mm, we'd need about 2.5 mm travel of the zoomed lens (L_1) to obtain a 1 μm change in the depth of the trap. This was made possible by mounting L_1 on a linear stage (Newport) driven by a servo motor (KO-Propo). The motor servo control signal, a simple linearly-varying voltage reflecting the motor position, could be amplitude-encoded atop a kilohertz carrier wave and recorded as an audio channel in synchrony with video images of the knot tying process.

Combining the beam steering with multiple beams, we simply use one lens for L_1 for

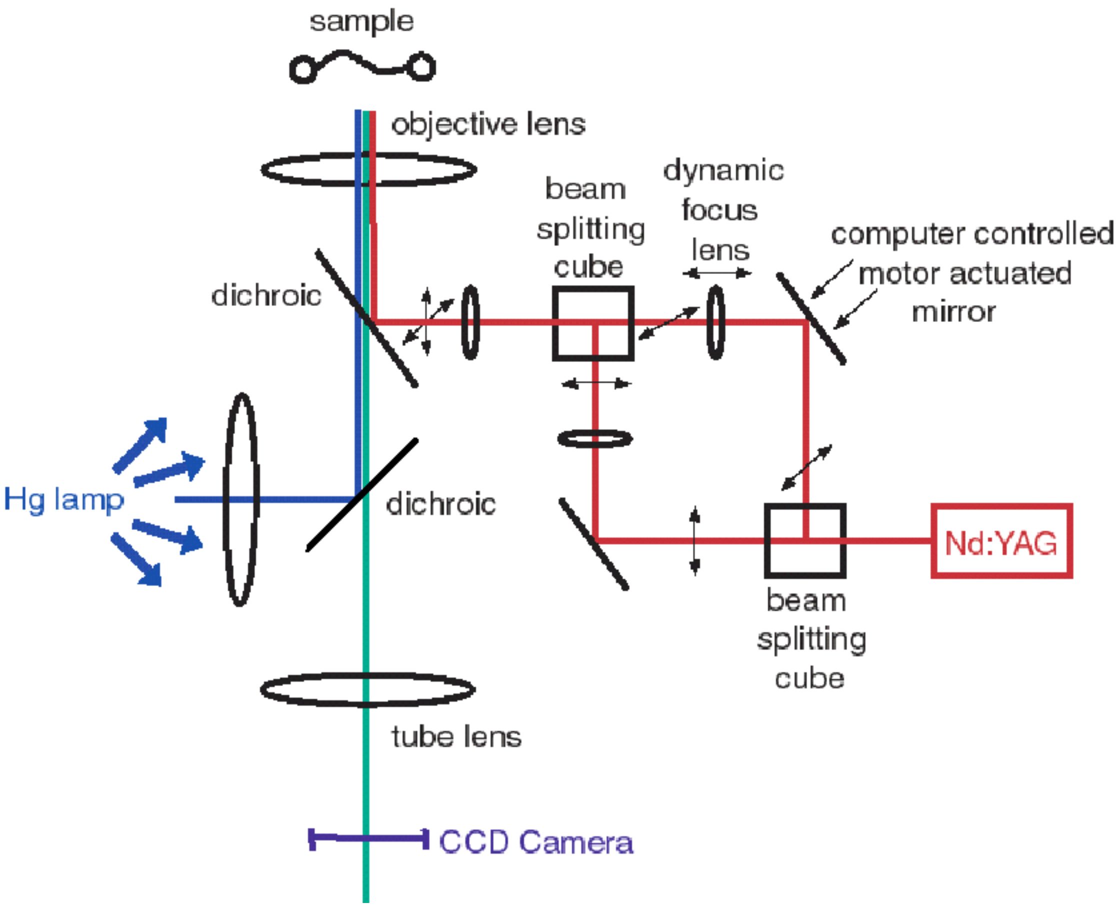

Figure 3.3: Simplified schematic of the combined optical trapping and fluorescence microscope used to tie knots. See text for details.

each beam, combine those beams with a polarizing beam splitter, and then have the two beams share a lens for L_2. This way we could have two independently steerable traps.

3.2.2 Imaging

Because the DNA molecule itself is so thin, imaging it in bright field is essentially impossible. As is standard practice, we imaged the DNA molecule by staining it with a dye and observing the dye's fluorescence. We used the dye YOYO-1, which is a dimer of fluorophores that, when free in solution, quench each other. When the fluorophores intercalate in between bases in the DNA molecule, however, the coupling between the fluorophores is broken so that they can no longer quench each other. This results in about a thousand-fold increase in fluorescence, so that the DNA molecule shows brightly even in the presence of free dye. Because both excitation and emission of YOYO-1 are at wavelengths far removed from the 1064 nm infrared laser we use for trapping, we could decouple these simply with dichroic mirrors. Figure 3.3 shows the full system put together.

3.3 How to physically tie a knot

Tying a knot is actually quite simple, conceptually. To form the simplest of knots, a 3_1, or trefoil knot, one simply needs to form a loop with a piece of DNA, and then thread that loop with one end of the DNA (fig. 3.4). We at first tried to establish standard tying protocols that could be programmed into the computer and then executed by servo motors driving the zoom lens and steering mirrors. However, because of the randomness of the ligation process used to generate longer DNA (§2.2), and because of random variations in the disposition of the DNA molecule at the start of knot tying, we decided that it would be easier to tie the DNA molecules by hand. Instead of moving the trap around the DNA molecule, we effected the same motion by moving the DNA sample around the trap with manually operated micrometers on the translation stage holding the DNA sample. Depth control of the trap was still done with a servo-controlled zoom lens, but with its position controlled by a set of electronic pedals situated on the ground below our optical table. Thus pseudo-three-dimensional control was afforded to the experimenter, and tying the DNA molecule became a fairly routine process once sample quality was achieved. In the end we were able to tie hundreds of knots into DNA molecules.

Figure 3.4: Tying a knot is actually quite easy with longer pieces of DNA. The panels here read down, then across, with the white vertical bar near the top of the image indicating the zoom depth of the optical trap. Thus, in making the initial loop, we pull the bead *over* the tail of the strand (middle left panel), so that we can pull the bead back under it again (top right panel) and then pull through to obtain a tied knot.

Chapter 4

System calibration

4.1 Optical trapping

We used the autocorrelational approach to calibrate our optical trap. The problem of a particle trapped in a harmonic potential has been treated in detail [22]. The main conclusion we use is that, for a particle with drag coefficient ζ in a potential

$$U = \frac{1}{2} k x^2, \tag{4.1}$$

the particle's position $x\left(t\right)$ has as its autocorrelation

$$\left\langle x\left(t\right) x\left(0\right)\right\rangle = \frac{k_B T}{k} \exp\left(-t/\tau\right), \tag{4.2}$$

where the decay time constant is $\tau = \zeta/k$.

The $x\left(t\right)$ here is actually measured as a photocurrent $I\left(t\right)$ from a quadrant photodiode, converted via operational amplifiers and load resistors into a voltage $v\left(t\right)$ which is then digitized by an analog-to-digital converter. We assume, for x within a certain range, the photocurrent is proportional to the displacement, but that proportionality constant is unknown. By fitting the computed autocorrelation to an exponential, we obtain a time

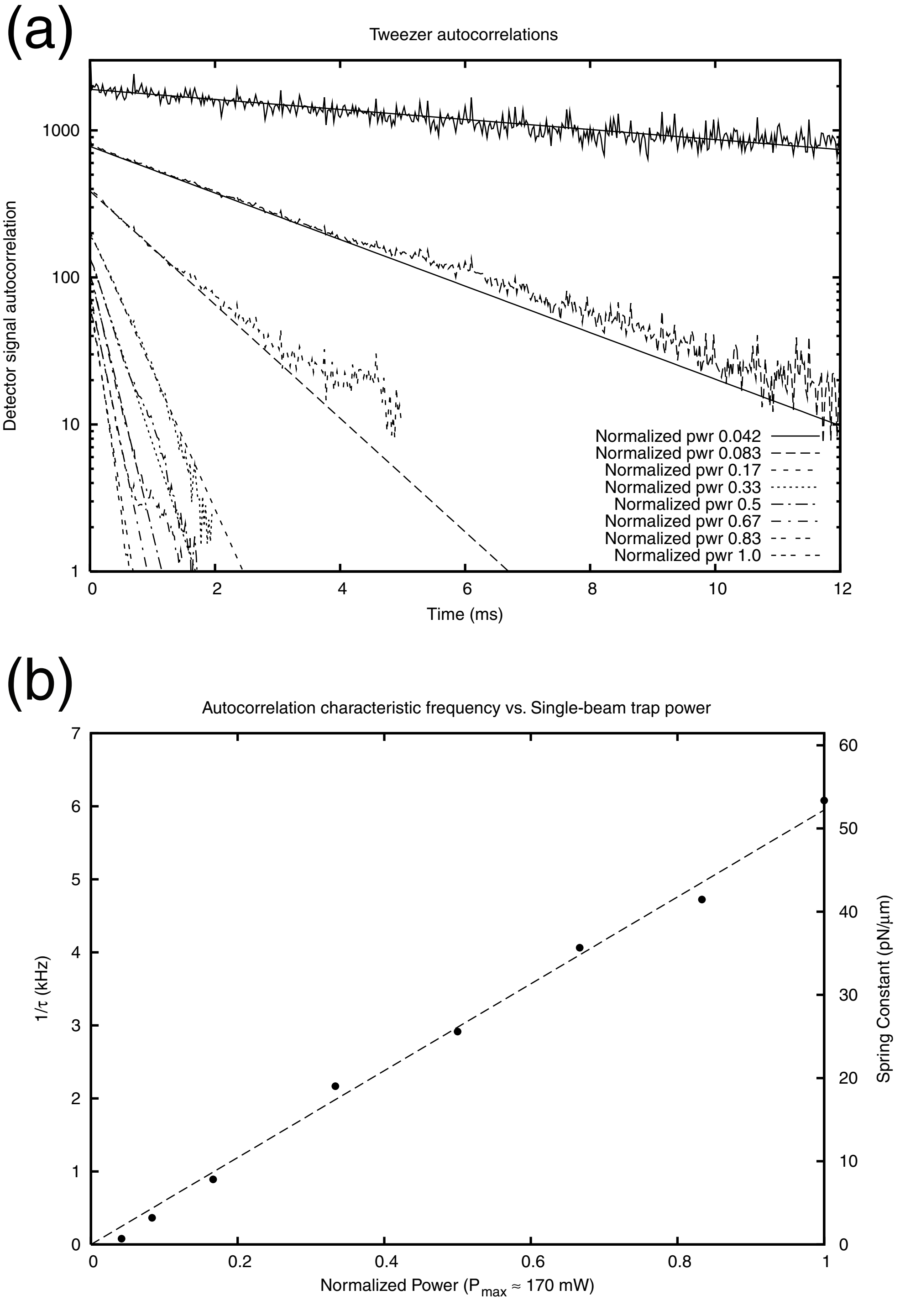

Figure 4.1: Optical trap calibration. To avoid mixing of signals, we opted to use only one trap; the laser beam for the other trap was stopped with a beam dump. We adjusted the quarter wave plate (see §3.2) to change the amount of laser power entering the microscope objective and forming the trap. The laser power was measured using a ThorLabs photodiode detector, with maximal power being 600 mW entering the objective, of which ≃170 mW emerged. (a) autocorrelations mostly decayed exponentially; these exponential fits easily give calibration parameters. (b) The trapping strength is proportional to the input laser power.

constant which should be independent of the position-to-current conversion factor. Using particles of known diameter d inside pure water, whose viscosity η is known, we can compute the bead's drag coefficient $\zeta = 3\pi\eta d$ and thereby infer the trap constant $k = \zeta/\tau$. The inferred trap constant then gives us the amplitude of the positional autocorrelation, which we can compare to the amplitude of the voltage autocorrelation to obtain the conversion factor between position and voltage.

Fig. 4.1 shows the results of this calibration. In particular, note that the spring constant scales quite nicely with the optical power entering the objective, as expected.

4.1.1 Classical escape force for Gaussian potential

For a strongly trapped particle, we can estimate the maximum trapping force by using classical stability analysis. In our trap, the focused beam waist is expected to be about 800 nm wide. The trapping strength of 25 pN/um, at a thermal energy of 4.11 pN nm, gives an average particle excursion of 12.8 nm from the beam center, which is much smaller than the beam waist diameter.

Let's just take a look in one direction. Classically, a bead bound in the trapping potential resides in a local minimum of that potential. Applying an external force f onto the bead simply means adjusting the trapping potential by $U_{\text{force}} = -fx$. This shifts the local minimum of the potential, but doesn't change the second derivative, which here must be positive for the equilibrium point to be a local minimum. Now, with the potential

$$U = -U_0 \exp\left(-\frac{x^2}{s^2}\right) \tag{4.3}$$

we have the second derivative

$$\frac{\mathrm{d}^2\mathrm{U}}{\mathrm{d}x^2} = \frac{2U_0}{s^2}\left(1 - \frac{2x^2}{s^2}\right)\exp\left(-\frac{x^2}{s^2}\right). \tag{4.4}$$

Clearly it's that second term in the product that will change signs. For $|x| < s/\sqrt{2}$ we have $U_{xx} > 0$, which means that, in the absence of thermal forces, the bead will be stably bound. Incidentally, the two boundary points are the points of highest potential slope, so the forces applied to the bead at those points are the highest forces that the trap can produce. That force is

$$\begin{aligned} F_{\max} &= \left.\frac{\mathrm{d}U}{\mathrm{d}x}\right|_{x=s/\sqrt{2}} \\ &= \left.\frac{2xU_0}{s^2}\exp\left(-\frac{x^2}{s^2}\right)\right|_{x=s/\sqrt{2}} \\ &= \frac{U_0\sqrt{2}}{s}e^{-1/2}. \end{aligned} \tag{4.5}$$

We have no easy, direct way of measuring the trap potential depth, but we do have access to second derivative of the potential at the trap bottom, which is just the spring constant (see above):

$$\begin{aligned} k &= \frac{\mathrm{d}^2\mathrm{U}}{\mathrm{d}x^2} \\ &= \frac{2U_0}{s^2}\left(1 - \frac{2x^2}{s^2}\right)\exp\left(-\frac{x^2}{s^2}\right); \end{aligned} \tag{4.6}$$

at the center of the trap it reduces to just $2U_0/s^2$, so we have

$$\begin{aligned} F_{\max} &= \frac{sk_0}{\sqrt{2e}} \\ &\approx 0.43\, sk_0. \end{aligned} \tag{4.7}$$

At the measured value of $k_0 = 25\,\mathrm{pN}/\mu\mathrm{m}$ and an estimated $s \simeq 760\,\mathrm{nm}$, we have $F_{\max} \approx 8pN$.

Flipping things around, we have as the potential barrier to escape $U_0 = ks^2/2$ which gives, for the same parameters, $U_0 \simeq 7.2\,\mathrm{pN}\cdot\mu\mathrm{m}$, or about 1800 times k_BT.

4.1.2 Thermal escape frequency under applied force

From a thermal standpoint, there really isn't any position in an optical trap that's stable. There will always be a time (maybe a very long time) over which a trapped bead is expected to escape the close vicinity of the trap center. Once it escapes, the bead will most likely wander off further and further away from the trap: in three dimensions, random walks have a less-than-unity probability of ever revisiting their origin.

For simplicity, I'll take a one-dimensional approach to the problem, since an applied force will break symmetry and give rise to a saddle-like "pass" in the energy landscape through which an escaping bead is most likely to transit.

The Kramers theory of reaction rates gives as the reaction rate

$$r \quad \sim \quad \frac{\sqrt{k\kappa}}{\zeta} e^{-Q/k_BT}, \tag{4.8}$$

where k and $-\kappa$ are the second derivatives in curvature at, respectively, the bottom of the potential well and the top of the potential barrier. ζ is the drag coefficient, Q the well height, and k_BT the thermal energy. In our simplified model we are in the happy situation where all these parameters are either provided or can be calculated. At room temperature, k_BT is $4.11\,\mathrm{pN}\cdot\mathrm{nm}$. For a bead with diameter $d = 1\,\mu\mathrm{m}$ in water with viscosity $\eta = 0.98\,\mathrm{cP}$, we have as the drag coefficient $\zeta = 3\pi\eta d \approx 9.24\,\mathrm{pN}/\left(\mathrm{nm}/\mu\mathrm{s}\right)$.

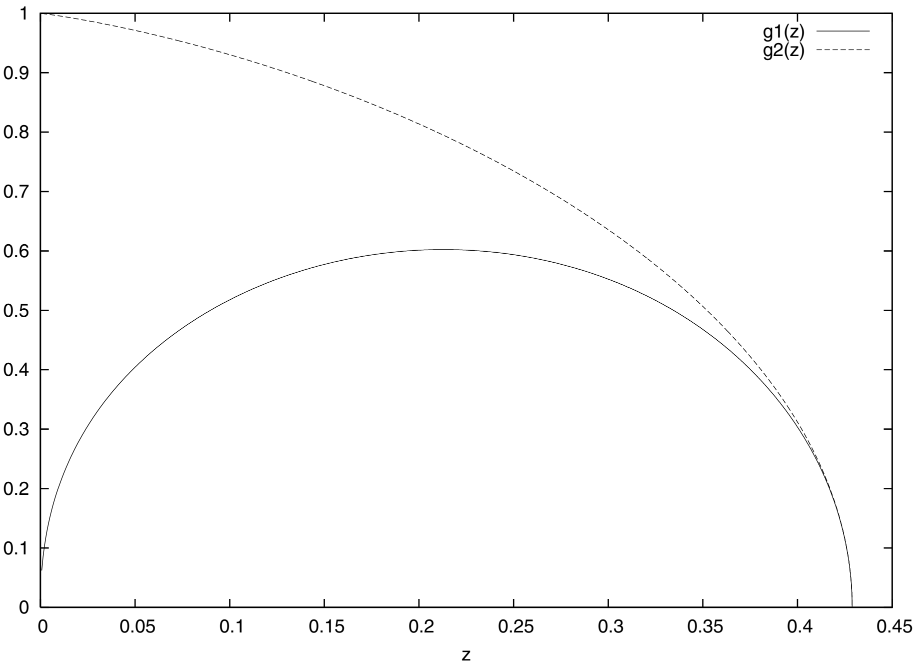

Figure 4.2: Auxiliary functions g_1 and g_2 for thermal escape frequency calculation; see text for details. Note that z must be below $z = (2e)^{-1/2}$, which corresponds to the classical escape force.

Now, any applied force simply adds a strictly linear potential to the trapping potential, so it doesn't actually change the second derivatives; the effect of the applied force is only to change the equilibrium positions at which those second derivatives are evaluated. We can rescale the applied force to be in multiples of U_0/s, which will mostly nondimensionalize the reaction rate equation, but note that the Arrhenius exponential factor doesn't scale that way.

So, let $x_1(z)$ and $x_2(z)$ be the two roots to the equation $f(x) = x \exp\left(-x^2\right) = z$ with

$x_1(z) < x_2(z)$. Then we have

$$
\begin{aligned}
F &= \frac{2U_0 z}{s} && (4.9)\\
k &= U''(s \cdot x_1(z))\\
&= \frac{2U_0}{s^2}\left(1 - 2x_1^2(z)\right)\exp\left(-x_1^2(z)\right) && (4.10)\\
\kappa &= -U''(s \cdot x_2(z))\\
&= \frac{2U_0}{s^2}\left(2x_2^2(z) - 1\right)\exp\left(-x_2^2(z)\right) && (4.11)\\
Q &= U(s \cdot x_2(z)) - U(s \cdot x_1(z))\\
&= U_0\left[\exp\left(-x_1^2(z)\right) - \exp\left(-x_2^2(z)\right)\right] && (4.12)\\
r &= \frac{2U_0}{s^2\zeta}\sqrt{\left(1 - 2x_1^2(z)\right)\left(2x_2^2(z) - 1\right)}\exp\left(\frac{-x_1^2(z) - x_2^2(z)}{2}\right)e^{-Q/k_B T}. && (4.13)
\end{aligned}
$$

So, defining two auxiliary, dimensionless functions (see fig. 4.2)

$$
\begin{aligned}
g_1(z) &= \sqrt{\left(1 - 2x_1^2(z)\right)\left(2x_2^2(z) - 1\right)}\exp\left(\frac{-x_1^2(z) - x_2^2(z)}{2}\right) && (4.14)\\
g_2(z) &= \exp\left(-x_1^2(z)\right) - \exp\left(-x_2^2(z)\right), && (4.15)
\end{aligned}
$$

we have, simply,[1]

$$
r \sim \frac{2U_0}{s^2\zeta} g_1(z) \exp\left[-\frac{U_0}{k_B T} g_2(z)\right]. \qquad (4.16)
$$

Clearly the parameters have physical interpretations: $r_0 = 2U_0/\left(s^2\zeta\right) = k/\zeta$ is just the base rate scale of the system, and $\tau = U_0/(k_B T)$ is just the nondimensionalized energy

---

[1] Given the "$\sim$" this is probably overkill, but being careful about what goes into the exponential is still useful.

scale, so that

$$r = r_0 g_1(z) \exp\left[-\tau g_2(z)\right]. \tag{4.17}$$

For $\tau \gg 1$, as in the case at hand, the Arrhenius exponential term dominates while the curvature term $g_1(z)$ remains of order unity over most of the force range. Near $f = 0$ for $\tau \simeq 1800$, as in the trap at hand, we have $r/r_0 \sim e^{-1800}$. With $r_0 \sim 3\,\mathrm{ms}$, that means that the trap lifetime is about 10^{780} s, or 10^{738} lifetimes of the universe.

Going from the mathematics back to understanding real time constants here is still pretty handwaving; more rigorous treatment of this particular model can be found in ref. 26. An added complication to the phenomenon comes from the fact that the DNA fiber tugging at our trapped bead is not a perfect spring. Specifically, the DNA itself exhibits drag and thus changes the Brownian dynamics; the changes that this introduces are considered in ref. 27.

4.2 Solution viscosity

Because all the knot dynamics get scaled by the solution viscosity, we needed to measure that viscosity for further analysis of the data. We performed this calibration by observing the diffusion of 1 μm beads.

The diffusion constant for a bead is

$$\begin{aligned} D &= \frac{k_B T}{\zeta} && (4.18)\\ &= \frac{k_B T}{6\pi\eta a}. && (4.19) \end{aligned}$$

We observe the diffusion constant by the mean squared deviation:

$$D = \frac{\left\langle x^2\left(t\right) - x^2\left(0\right)\right\rangle}{2t}. \tag{4.20}$$

Plotting the mean squared deviation as a function of time, we can compute a best fit line slope m, so that $D = \alpha m$. To convert from m's units of $\mathrm{pix}^2/\mathrm{fr}$ to $\mu\mathrm{m}^2/s$, and account for the factor of 2, we've multiplied by a conversion factor $\alpha = 0.0927884$; this incorporates the horizontal resolution of 12.7 pixels per micron, computed from the image of a 600 lines/mm grating, and the frame rate of 29.97 frames per second. This then gives

$$\begin{aligned} \alpha m &= \frac{k_B T}{6\pi\eta a} \\ \eta &= \frac{k_B T}{6\pi\alpha m a}. \end{aligned} \tag{4.21}$$

We have numbers:

- $k_B T$ is just the thermal energy, 4.11 pN·nm. Or 4.11×10^{-21} J.
- a is the bead *radius*. We're using 1 μm diameter beads, so $a = 5 \times 10^{-7}$ m.
- m is measured from bead videos. For water, we have $m = 5.03215$. In this the fudge factor is $\alpha = 9.279 \times 10^{-14} m^2/s$.

From which we derive the viscosity $\eta = 9.339 \times 10^{-4}\,\mathrm{Pa}\cdot\mathrm{s}$, a few percent deviation from water's theoretical value of $9.8 \times 10^{-4}\,\mathrm{Pa}\cdot\mathrm{s}$.

If we use $m = 0.597$ from the 6% PEG viscosity measurement, we get $\eta = 7.870 \times 10^{-3}\,\mathrm{Pa}\cdot\mathrm{s} = 7.87\,\mathrm{cP}$.

Chapter 5

Results and discussion

To study how higher-order knotting structure affects dynamics, we constructed knots following the ordering scheme of a standard knot table. Knots are designated by C_k, with C the minimal number of self-crossings displayed when the knot is projected into a plane, and k a cardinal index used to distinguish between topologically different knots with the same C. By threading the DNA loop multiple times, or making more complicated loops before threading them, we were able to consistently construct knots of types 4_1, 5_1, 5_2, and 7_1, in addition to the simplest knot 3_1 (fig. 5.1d). Approximately 100 different DNA molecules were successfully tied into knots, and about one third of the knots provided useful quantitative data.

All of the knots shrank under tension, becoming highly localized, diffraction-limited spots at tensions as low as 0.1 pN (fig. 5.1a). We traced DNA shapes using an active contour ("snake") algorithm [28] and computed intensity profiles from those shapes. When we tiled intensity profiles from successive frames, bright tracks became identifiable, indicating that the knots move over time (fig. 5.1b). In control molecules in which we did not tie a knot, these bright tracks were present about 10% of the time, close to the expected probability of random thermal knotting in DNA. We quantified these tracks and computed mean squared distance travelled as a function of time. Logarithmic plots (fig. 5.1c) indicate

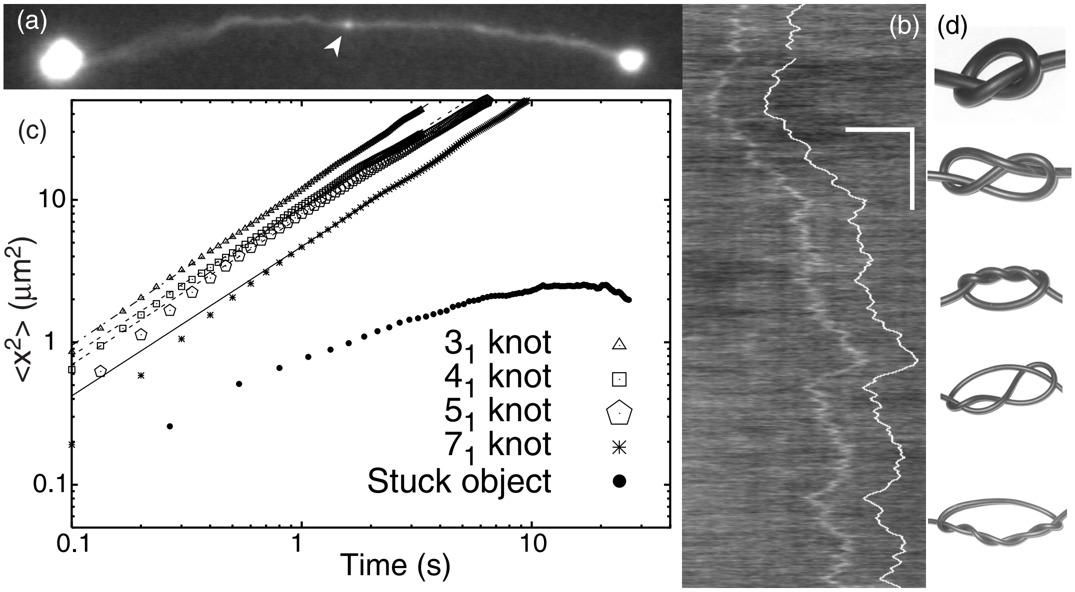

Figure 5.1: Observing knot diffusion. (a) The stained, knotted DNA appears as a diffraction-limited contour between two beads, with an increase in fluorescence at the knot (arrow). The path of the DNA is found by software and its intensity profile computed; tiling these profiles from sequential frames (b) reveals a diffusive trace which indicates the knot's trajectory. Scale bars, 5 μm (horizontal) and 5 s (vertical); scale of (a) is same as horizontal scale of (b), The trace is quantified (offset white trace) and its mean squared traveled distance as a function of time t computed (c) which obeys a power law with exponent $\alpha \approx 1.06$ (see text). “Stuck object” denotes what appeared to be a stray piece of DNA crosslinked to the main DNA strand and observed to diffuse along the length of the main DNA strand under the strand's entropic elasticity. (d) We have tied and analyzed open knots of types (from top to bottom) 3_1, 4_1, 5_1, 5_2, and 7_1.

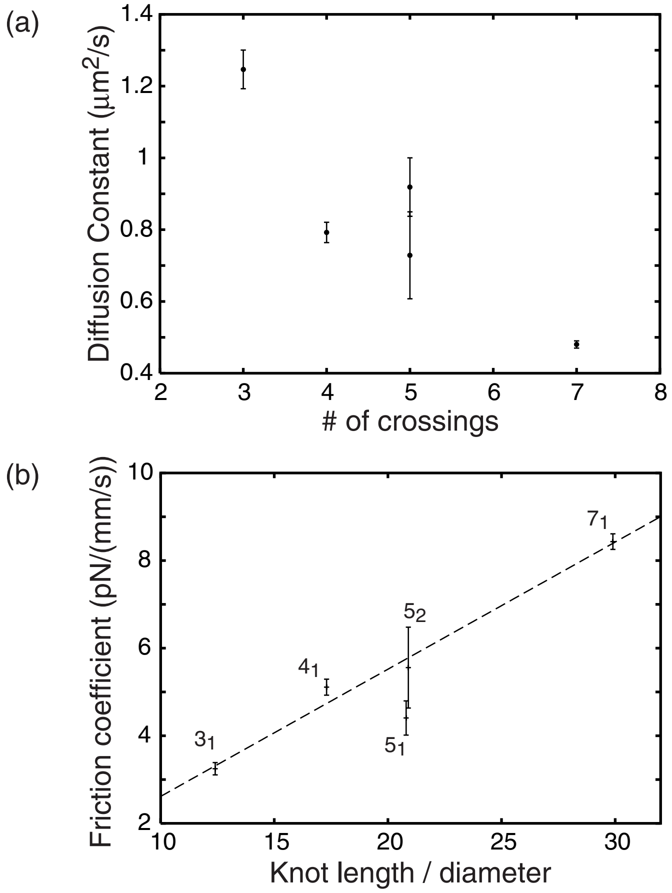

Figure 5.2: Knot diffusion constants D vary dramatically with complexity (a); their respective friction coefficients $\zeta = k_B T/D$ correlate well to theoretical knot lengths (b). The slope of the best fit line is 0.29 ± 0.003 pN/(mm/s)=$(2.9 \pm 0.3) \times 10^{-10}$ N/(m/s). The observed knot sizes (see text and fig. 5.3) are smaller than typical DNA fluctuation, so the knot is expected to track the DNA contour during diffusion, making the distance it traverses one of contour length. Thus all diffusion constants here were rescaled by two factors of relative extension (i.e., the ratios of end-to-end distance to contour length) before averaging. Only data points with relative extensions between 0.55 and 0.75 were used. The numbers of knots observed were 23, 9, 3, 4, and 3 for knot types 3_1, 4_1, 5_1, 5_2, and 7_1, respectively.

a power law relation $\langle x^2 \rangle \propto t^{\alpha}$. The value of α averaged over all knots was 1.06 ± 0.02, in agreement with classical random walk statistics. We then computed diffusion constants by plotting the diffusion data on linear axes and fitting to a line, leaving the offset term free to compensate for short-time artifacts from both observation and analysis; slopes obtained from these fits then become our diffusion constant measurements. We found no discernible tension dependence in knot properties at the tensions (0.1-2 pN) used to extend the DNA molecules. However, the diffusion constant varies dramatically with knot complexity (fig. 5.2).

Since the knots have conserved topologies, they must move with a snake-like motion of the polymer through the knot structure, analogous to the reptating motion of a polymer in the presence of a fixed obstacle network. We call this motion "self-reptation" since the same molecule is both constraining and constrained. One can thus define a characteristic time $\tau_{\text{rept}} \sim \frac{L^2}{D}$ equal to the time it takes the knot to diffuse through the length L of DNA comprising the knot; this time is analogous to the lifetime of the reptation tube. The total length L of polymer engaged within a given knot type has been calculated in numerical simulations of tight, open knots constructed of ideal ropes [29]. Comparing our drag coefficients $\zeta = \frac{k_B T}{D}$ to these lengths yields a roughly linear relationship (fig. 5.2b), so $D \sim L^{-1}$ and hence $\tau_{\text{rept}} \sim L^3$, consistent with the reptation model [22, 30] and with observed behavior of DNA in an entangled solution [31].

Besides analyzing the kinetics of knot motion, it is also possible to extract information about the relative sizes of the knots from the microscope images. Using the knot position information from track quantification, we averaged knot intensities and compared them to intensities on adjacent unknotted parts of the DNA. Because the knot sizes are below the resolution of the imaging system, we could only measure the extra amount of DNA present

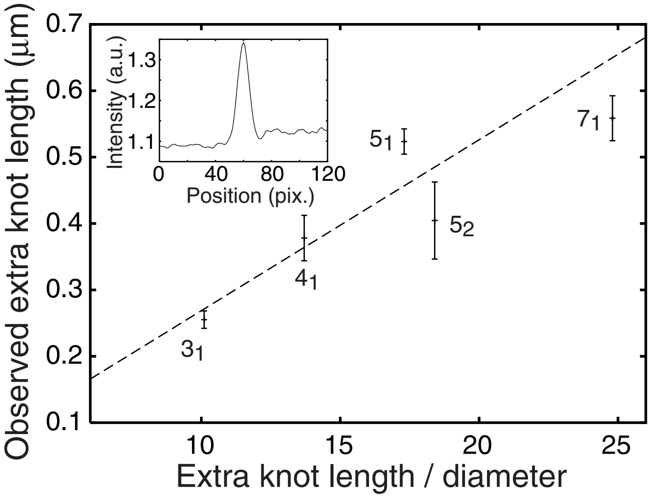

Figure 5.3: Averaged extra knot lengths correlate with those determined from numerical simulations of ideal open knots [29]; the slope of the best fit line gives a DNA effective diameter of 26 ± 6 nm. The ordinate axis represents the difference between length required for a knot and an unknotted segment.

in the knot as compared with an unknotted strand spanning the same distance; this will in general be different than the total knot length L, but instead correspond to the change in length caused by the knot in a tight, ideal rope. These dimensionless theoretical lengths Λ_O are relative to rope diameter, and have been studied computationally [29]. Comparing them to the absolute knot length measurements (fig. 5.3) gives an average inter-strand spacing of 26 ± 6 nm. This is most likely due to electrostatic self-repulsion of the charged DNA molecule, and the effect is similar in magnitude to computations and observations for DNA in bulk [15].

The above analyses assume that the knot conformations can be approximated as those of ideal tight knots, i.e. conformations which maximize strand-strand distance. Another possibility would be that the knot size is determined by by DNA bending rigidity. In that case, topological crossings in the trefoil (3_1) knot would occur along a small part of the loop (as in fig. 3c of [32]). We can thus calculate the radius of the rigidity-dominant knot using elastic bending theory:

$$R = \sqrt{\frac{k_B T \xi_p}{2F}} \simeq \frac{10\text{nm} \cdot \sqrt{\text{pN}}}{\sqrt{F}}, \tag{5.1}$$

where F is the tension on the rope, $k_B T$ the thermal energy, and ξ_p the persistence length. Since most measurements were performed at $F \sim 1\text{pN}$, elastic return forces should give an extra length of $2\pi R \sim 61\text{nm}$, or only about one quarter of the 255 nm trefoil knot size. This argument should be valid for all torus knots, including the 5_1 and 7_1, so it predicts that the sizes of rigidity-dominant torus knots are independent of knot type; this is inconsistent with the data in fig. 5.3.

Having quantified both the size and mobility of knots, we can propose a simple hydrodynamic model to link these measurements. The constraint network for any given part of the knot is formed by other parts of the same knot, so the "walls" of the effective reptation tube move during diffusion. From computed conformations of ideal knots [29], it appears that the constraining strands in the network are generally perpendicular to the constrained strand; we should therefore expect little or no net force in the direction of strand motion from the constraining strands within a reptating knot. We can then model the friction coefficient as arising from the viscous drag of one long cylinder (the constrained DNA strand) within another (the constraining tube). From [33], p. 54, this gives a drag coefficient per unit length ζ/L as a function of the ratio ρ of radii of the cylinders and the viscosity η:

$$\frac{\zeta}{L} = \frac{2\pi\eta}{\ln\rho}. \tag{5.2}$$

In this case, L is the length of DNA comprising the knot. The inner cylinder radius is half of the hydrodynamic diameter of 2.5 nm for DNA, and the outer cylinder radius is the observed mean separation between strands of 26 nm. This gives an axial force contribution of $\zeta/L \approx 0.017 \pm 0.002$ Pa·s, which is in fair agreement with the value of 0.011 ± 0.003 Pa·s derived from the slope in fig. 5.2b, especially given the simplicity of the present model. Presumably the flow field associated with motion of DNA through the knot will "bleed" beyond the phantom tube defined by its contraints, reducing the energy dissipation and giving rise to a slightly lower drag than that predicted by our model.

We have thus shown that knots along an extended DNA molecule behave in a manner consistent with predictions for ideal, tight, reptating knots. Despite having dimensions comparable to the persistence length of DNA, the knots are quite mobile and form one of the smallest known models of reptation. They are also a model system for the study of tightly confined DNA which is present in systems as diverse as eukaryotic nucleosomes and packaged virus heads. Finally, visible DNA knots of known topology are ideal substrates for studying the enzymology of topoisomerases at the single molecule level.

Bibliography

[1] H. Gardner. *Art Through the Ages*. Harcourt Brace, Fort Worth, 1996.

[2] W. Thompson. *Philos. Mag.*, 34:15, 1867.

[3] P. G. Tait. *Scientific Papers*. Cambridge University Press, London, 1898.

[4] V. F. R. Jones. Knots in mathematics and physics. *Lecture Notes in Mathematics*, 1525:70, 1992.

[5] J.-P. Sauvage and C. Dietrich-Buchecker, eds. *Molecular catenanes, rotaxanes, and knots*. Wiley, New York, 1999.

[6] C. N. Yang and M. L. Ge, eds. *Braid Group, Knot Theory, and Statistical Mechanics*. World Scientific, New Jersey, 1989.

[7] D. W. Sumners and S. G. Whittington. Knots in self-avoiding walks. *J. Phys. A*, 21(7):1689–94, 1988.

[8] S. R. Quake. Topological effects of knots in polymers. *Phys. Rev. Lett.*, 73(24):3317–3320, 1994.

[9] P.-G. de Gennes. Tight knots. *Macromolecules*, 17:703–4, 1984.

[10] F. B. Dean, A. Stasiak, T. Koller, and N. R. Cozzarelli. Duplex DNA knots produced by Escherichia coli topoisomerase I. Structure and requirements for formation. *J. Biol. Chem.*, 260(8):4975–83, 1985.

[11] O. Sundin and A. Varshavsky. Arrest of segregation leads to accumulation of highly intertwined catenated dimers — dissection of the final stages of SV40 DNA replication. *Cell*, 25(3):659–69, 1981.

[12] N. J. Crisona, R. Kanaar, T. N. Gonzalez, E. L. Zechiedrich, A. Klippel, and N. R. Cozzarelli. Processive recombination by wild-type gin and an enhancer-independent mutant — insight into the mechanisms of recombination selectivity and strand exchange. *J. Mol. Biol.*, 243(3):437–57, 1994.

[13] R. Metzler. Localization behaviour in a phenomenological model of three-dimensional knots. *New J. Phys.*, 4:91, 2002.

[14] V. Katritch, W. K. Olson, A. Vologodskii, J. Dubochet, and A. Stasiak. Tightness of random knotting. *Phys. Rev. E*, 61(5):5545–5549, 2000.

[15] V. V. Rybenkov, N. R. Cozzarelli, and A. V. Vologodskii. Probability of DNA knotting and the effective diameter of the DNA double helix. *Proc. Natl. Acad. Sci. USA*, 90(11):5307–11, 1993.

[16] S. Y. Shaw and J. C. Wang. Knotting of a DNA chain during ring-closure. *Science*, 260(5107):533–6, 1993.

[17] X. R. Bao, H. J. Lee, and S. R. Quake. Behavior of complex knots in single DNA molecules. *Phys. Rev. Lett.*, 91(26):265506, Dec. 2003.

[18] S. Katsura, K. Hirano, Y. Matsuzawa, K. Yoshikawa, and A. Mizuno. Direct laser trapping of single DNA molecules in the globular state. *Nucl. Acids Res.*, 26(21):4943–5, 1998.

[19] M. Ptashne. *A Genetic Switch: Gene Control and Phage λ*. Cell Press and Blackwell Scientific, Cambridge, MA, and Palo Alto, CA, 1986.

[20] A. Kornberg and T. A. Baker. *DNA Replication*. W. H. Freeman and Co., New York, 2nd ed., 1991.

[21] R. M. Zimmermann and E. C. Cox. DNA stretching on functionalized gold surfaces. *Nucleic Acids Res.*, 22(3):492–7, 1994.

[22] M. Doi and S. F. Edwards. *The Theory of Polymer Dynamics*. Clarendon Press, 1986.

[23] R. I. Lehman. DNA ligase: Structure, mechanism, and function. *Science*, 186(4166):790–7, 1974.

[24] A. Ashkin, J. M. Dziezdic, J. E. Bjorkholm, and S. Chu. Observation of a single-beam gradient force optical trap for dielectric particles. *Opt. Lett.*, 11(5):288–90, 1986.

[25] S. Gross. Application of optical traps in vivo. *Meth. Enzymol.*, 361:162–74, 2003.

[26] E. Evans and K. Ritchie. Dynamic strength of molecular adhesion bonds. *Biophys. J.*, 72(4):1541–1555, Apr. 1997.

[27] A. Sain and M. Wortis. Influence of tether dynamics on forced kramers escape from a kinetic trap. *Phys. Rev. E*, 70(3):031102, 2004.

[28] M. Kass, A. Witkin, and D. Terzopoulos. Snakes — active contour models. *Int. J. Comput. Vision*, 1(4):321–31, 1987.

[29] P. Pieranski, S. Przybyl, and A. Stasiak. Tight open knots. *Eur. Phys. J. E*, 6:123–8, 2001.

[30] P.-G. de Gennes. Reptation of a polymer chain in presence of fixed obstacles. *J. Chem. Phys.*, 55(2):572–9, 1971.

[31] D. E. Smith, T. T. Perkins, and S. Chu. Self-diffusion of an entangled DNA molecule by reptation. *Phys. Rev. Lett.*, 75(22):4146–9, 1995.

[32] Y. Arai, R. Yasuda, K. Akashi, Y. Harada, H. Miyata, K. Kinosita, and H. Itoh. Tying a molecular knot with optical tweezers. *Nature*, 399(6735):446–8, 1999.

[33] L. D. Landau and E. M. Lifshitz. *Fluid Mechanics*. Butterworth and Heinemeann, Oxford, 1987.

Part II

A microfluidic platform for performing cell signaling experiments with single cell sensitivity

Chapter 6

Introduction and motivation

6.1 A new platform for biological signaling?

Biological signal transduction, put broadly, is the process whereby information about external events and conditions is processed and converted to appropriate responses; this response is typically, but by no means limited to, a change in the gene expression profile of the cell. Signal transduction forms the very underpinning of multicellularity, since it is critical to communication and cooperation between different cells.

In mammalian cells, signal transduction makes use of a vast apparatus of proteins, lipids, and small molecule second messengers to generate appropriate responses. Large parts of the apparatus are re-used in different cells for completely different purposes. This is encouraging because it suggests that, once we understand the function of a module in some signaling pathway, that understanding should ease elucidation of the function of the module in the other contexts. Against the optimism stands the enormous complexity of mammalian systems in general, both within and amongst identifiable modules.

The rise of molecular biology in the decades since Watson and Crick has brought with it a reductionist viewpoint of how to understand biological systems, which is to first understand the bits and pieces individually and then piece the knowledge together to understand whole systems. That second part of the equation has until recently been somewhat neglected, proving rather more difficult than expected [1, 2]. It is becoming apparent that integrating together the knowledge of individual components and interactions within a given pathway will require quantitative understanding of those components and interactions, especially when feedback is involved which can give very different behaviors for the same network topology [3, 4].

From an engineer's standpoint, at some level a quantitative understanding of a system requires quantitative data about that system, be they rate constants for the individual reactions comprising that system or performance characteristics (e.g., input/output relationships) of the system as a whole. Because there are large numbers of inputs and outputs for typical cellular signaling networks, an even partial, but systematic, characterization of a given signaling transduction network will require many, many different experiments [5].

Most upstream processes in signaling rely upon changes in either protein conformation or localization to encode and transmit information. Detecting protein changes *ex vivo* will, of course, kill the cells under observation to obtain any one data point and preclude tracking variations for the same sample over time. It also usually precludes single cell sensitivity because pooling proteins from thousands to millions of cells is required to obtain enough signal (but see [6]). Observations *in vivo* tend to suffer from a biological analog to Heisenberg's uncertainty principle, since proteins usually go about their jobs with little fanfare or, more importantly, directly observable signal: tracking proteins *in vivo* with specificity tends to require expressing modified proteins to report changes associated with signaling. Expression of modified proteins will almost always change quantitatively the functioning of the signaling apparatus; there is also the chance that the functioning is changed qualitatively as well. In addition, these techniques tend to be labor-intensive and not well suited to high-throughput methods.

Mammalian cells exhibit wide variability in terms of their signaling behaviors. Within an experiment, the variation gives a large range of observed behaviors for identical conditions. This variability can be exploited to provide new insights into the underlying nature of a given biological system [7], and is often critical to understanding phenomena observed at the populational, averaged level [8]. Between experiments, variability in the population structure itself is a problem to be overcome, since it can contaminate the interpretation of differences between experiments and controls. This bulk variability can arise from differences in preparations of cells which can be difficult to avoid, or can arise from cells changing characteristics as they slowly age.

In addition, observed responses of cells sometimes arise as secondary responses from an initial stimulus. For instance, an inflammatory initial stimulus might trigger immune cells to secrete cytokines, and it would be the response of those same cells to the secreted cytokines that would be measured in a signaling assay. This possibility further complicates analysis of the results of signaling experiments.

What I wanted, then, was to improve upon existing ways of observing signaling in mammalian cells. The new platform should be versatile, so that its basic structure could be adapted to many different experiments. It should provide for higher throughput. It should provide continuous perfusion so that cell secretions are swept away before they can influence cell behavior. It should have single cell resolution to allow observation of population distributions, not just population averages, but at the same time allow for direct comparison between multiple experiments under identical conditions. I decided to try to meet these goals using microfluidic technology.

6.2 Microfluidic soft lithography

Microfluidic technologies use microfabrication techniques to generate micron-scale "plumbing". Devices made using these technologies typically use dramatically less reagent and can take advantage of different physical phenomena that occur as the size scale shrinks [9]. Fabrication of microfluidic devices using soft lithography [10] is very fast and easy, requiring only very basic equipment and no difficult or hazardous processing. This, often combined with the ability to put pneumatic valves [11] into devices, has allowed the application of microfluidics to a whole host of problems in biology [12, and references therein].

For my purposes, microfluidics allowed easy integration of multiple experiment chambers into a given field-of-view of a microscope, and integration of flow control into an experimental platform. As elaborated in Chapter 7 and demonstrated in Chapter 10, I used these two approaches to design and create devices that would allow several different perfusion-based signaling experiments to be imaged simultaneously with single cell resolution.

The material with which I made devices was poly(dimethylsiloxane) (PDMS), specifically Sylgard 184 (Dow Corning). PDMS is the material used for much of the original research in microfluidic soft lithography, and for good reason: PDMS is very easy to work with, and when cured is tough yet flexible (Young's modulus in the MPa range). In addition, PDMS is optically clear and allows for easy optical interrogation of material within devices. It is permeable to gas, so that channels can be filled with fluid by dead-end priming under an applied pressure, and oxygen and carbon dioxide can diffuse into the channels to support metabolism and pH buffering, respectively.

PDMS comes as a silicone oil base and a curing part, and, after mixing and curing, the two will form a crosslinked rubber. By manipulating the ratio of curing part to oil base, the surface chemistry of the silicone can be tuned so that two pieces of PDMS can be bonded together after they have been cured [11]; undercuring the two initial pieces also contributes to the strength of the bond. Sylgard 184 cures very quickly and therefore allows for rapid fabrication, whether for prototyping or production purposes (see Appendix B): typical fabrication times for a batch of four devices, once the molds have been made, were about two hours, and turnaround times from design to device could be as rapid as three days. The fabrication speed and low cost of the base material made PDMS devices cheap enough to be disposable, obviating issues of device cleaning and reuse. I did encounter some problems peculiar to PDMS, but they could usually be overcome and did not outweigh the aforementioned advantages.

6.3 Biological background to calcium signaling

I used observations of G protein-coupled intracellular calcium release as the first experiment to try with the microfluidic devices. Quantitative sensing of intracellular calcium is relatively straightforward to do (see below), and moreover, because free calcium concentrations could reach large fractions of 1 μM over the course of an experiment, I expected large signals. Detection sensitivity was therefore less of an issue, and I was able to tolerate a large loss of optical signal as the price of having a large detection area using standard microscope optics (see §9.1).

Resting cells typically have large calcium concentration gradients across their membranes, with < 100 nM inside the cytoplasm and millimolar concentrations in the endoplasmic reticulum (ER) and extracellular media. Release of calcium ions into the cytoplasm represents a ubiquitous intermediate step in mammalian signal transduction. Calcium release as a signaling “second messenger” is important in behaviors as diverse as oocyte fertilization, muscle contraction, neuronal signal processing and neurotransmitter release, and immune cell activation [13]. It is in connection with the last application that my experiments were performed.

The other half of this story, that of G protein activation, is an equally important and fascinating part of biological signal transduction. G proteins are membrane-bound proteins that act as signaling intermediates in a myriad of different processes. Inactive G proteins bind GDP and exist as heterotrimers of α, β, and γ units. When activated, a G protein exchanges its GDP for a molecule of GTP, and subsequently dissociates into the GTP-bound α subunit and a $\beta\gamma$ heterodimer; both of these dissociation products can be used to transmit signals downstream. The G_α subunits are usually endowed with a basal rate of GTPase activity, so after some time it cleaves a phosphate off of GTP, converting it back into GDP, and then rebinds a $\beta\gamma$ dimer to return to its inactive form. Thus, G proteins form a self-resetting “switch” that can be turned on or off. They can provide amplification in signaling, since any given activated receptor can turn over many G protein complexes, as well as additional opportunities for signal modulation through proteins such as regulators of G protein signaling (RGS) that can alter their GTP hydrolysis rate. Receptors involved in olfaction are all G protein-coupled receptors (GPCRs), as are a large class of neurotransmitter receptors, immune-related receptors, and visual rhodopsin, among others.

In the system I have been looking at, the flux of information and reactants, moving from ligand binding to calcium release, is as follows (also see fig. 6.1). Once a G protein-coupled receptor binds its cognate ligand, it changes conformation state and starts to cat-

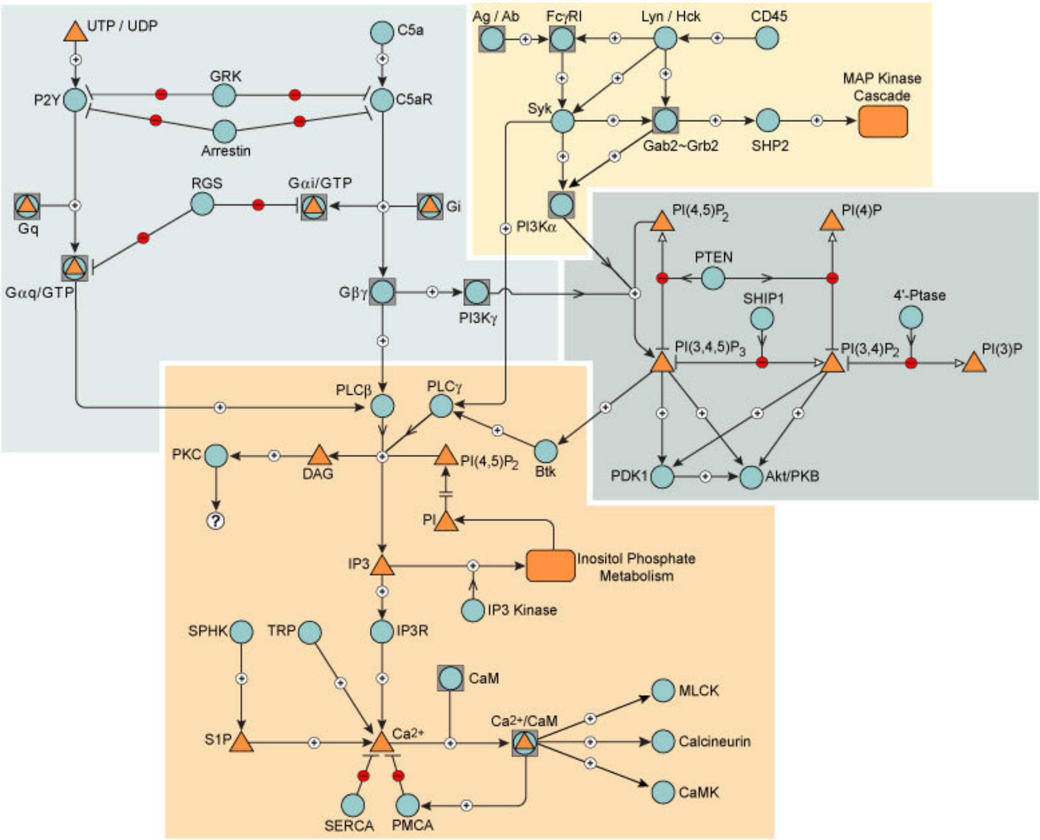

Figure 6.1: Schematic diagram of the signaling network I'm looking at. This is actually a superset; the G protein-coupled pathway appears on the left side. See text for further details.

alyze G proteins dissociation. Either dissociation product, the GTP-bound G_α or the $G_{\beta\gamma}$ heterodimer, can make the link to the next stage by activating the β subtype of phospholipase C (PLCβ), which catalyzes the cleavage of phosphatidylinositol-4,5-bisphosphate (PIP_2), a minor phospholipid component of the plasma membrane, into diacylglycerol (DAG) and inositol-1,4,5-trisphosphate (IP_3). IP_3 then diffuses to, and binds, its receptor on the ER surface (the IP_3 receptor IP3R), which in turn opens and releases the calcium ions stored in the ER into the cytosol [14].

Calcium release can be observed by loading cells with a cytoplasmic calcium-sensitive fluorescent dye. Just about any observation of molecular events inside the cell requires a contrast mechanism that can affect the very cellular physiology it is trying to measure, and with calcium the situation is no different. By introducing a calcium-sensitive dye into the cytoplasm, especially enough to make use of a large fraction of the released calcium ions, I also introduce a significant and fast-diffusing calcium buffering activity. Because calcium dynamics inside a cell can exhibit significant positive feedback due to the presence of calcium-sensitive calcium release channels [13, 15], such buffering can potentially suppress calcium concentration oscillation and spiking. Some experimental evidence suggests this to be true at the concentration of indicator that I've been using (R. Rebres and T. Roach, unpublished results).

The gist of my experiments with G protein-coupled calcium signaling was that I used calcium release as a readout to infer the properties of the upstream signaling network. Thus, while I *did* modify the calcium response network, the modification was downstream of the processes of interest whose properties I was inferring. Observing the system downstream should thus result in less perturbation to the upstream parts of interest. Verification of data integrity (§10.1) suggests that this may be the case.

My work on GPCR-induced calcium release focused mainly on three ligands: the nucleotide UDP, which activates the P2Y family of receptors [16]; the anaphylatoxin protein fragment C5a, which activates its own unique receptor C5aR; and platelet activating factor (PAF), a small lipid molecule which also has its own unique receptor PAFR. These different ligands use the available G proteins in the cytosol differently: UDP uses mostly $G_{\alpha q}$ (with some $G_{\alpha 11}$), C5a mostly $G_{\alpha i}$, and PAF uses both. GTP-bound $G_{\alpha i}$ does not activate PLCβ, so when it is dissociated from the heterotrimer it is the $\beta\gamma$ subunit that activates PLCβ.

Much of the biochemistry and cell biology in this project was done in collaboration with the Alliance for Cellular Signaling [17] (AfCS), of which the Simon lab is a part. Appendix

C reproduces the original protocols produced by the AfCS on which my experimental protocols were based.

Chapter 7

Device and instrument design

7.1 Introduction and design objectives

An integrated microfluidic device that performs experiments on mammalian cells as outlined in §6.1 has to accomplish four things:

- Placement of cells into, and retention within, appropriate chambers
- Maintenance of cells at consistent, physiological conditions
- Application of reagents to the cells of interest
- Observation of cells and their responses to reagents

Development of the microfluidic device and the associated protocols for handling solutions and cell suspensions proceeded in parallel, both informed by considerations of cell biology and device physics. For instance, I had to try quite a few different approaches, physical as well as chemical, to prevent cells from adhering to valve areas before arriving at the one described below, which was the first one to work well enough consistently. One of the more successful aborted efforts is described elsewhere (§13.2). This chapter covers the microfluidic aspects of experiment design; the next two chapters cover biochemistry protocols and experimental data acquisition details.

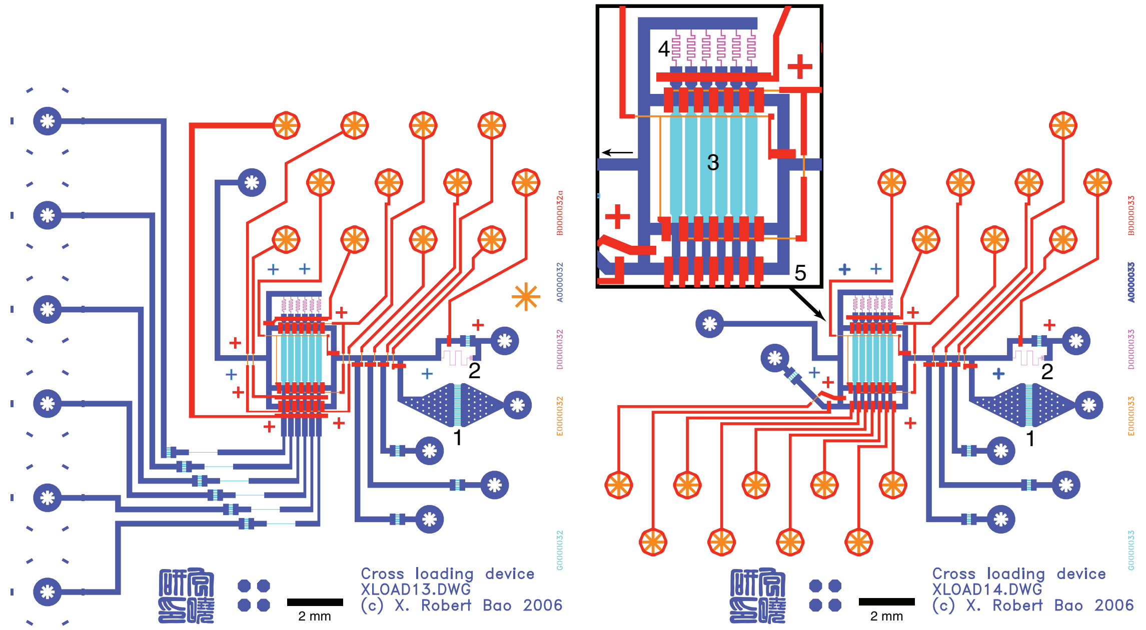

Figure 7.1: Fluidic device designs for performing cell signaling experiments. In the left panel is a device for screening different ligand conditions, and in the right panel is a device for performing differential solution kinetics studies. The graphics show the control layer design (red and yellow) superimposed atop the flow layer design (blue, light blue, and purple). 2 mm scale bars in black. In the control layer, red features are patterned into 30 μm high SU-8 photoresist, and yellow features into 10 μm high SU-8. In the flow layer, light blue features are patterned into 25 μm high SU-8, purple features into 10 μm high SU-8, and blue features into AZ-100 photoresist that, after thermal rounding, yields features with peak heights of $\sim$45 μm. Inset on the right shows the central cell-bearing region of the kinetics device, magnified for clarity. Numbered features are as follows: (1) cell strainer for cell clumping control; (2) high-resistance flow constriction to slow down media flow during cell culturing; (3) cell-bearing cross channels; (4) flow balancing and moderating flow constrictions; (5) offset flow shunt for elimination of stale solutions. See text for detailed explanations of these features.

Fig. 7.1 shows the two final device designs I used for data collection. The first design allows flushing of each cell-bearing chamber with a different fluid, while the second design allows flushing of cell-bearing chambers with the same fluid but at different times. Each also has an extra manifold for perfusing fluids to all chambers at once.

7.2 Cell placement and adhesion

Placement of cells into the chambers proved quite a challenge. Cells needed to be suspended as a single cell suspension and injected into the device. As suspended macrophages were typically about 15 μm in diameter, the channels carrying macrophages had to be at least that wide, and optimally a lot wider to avoid clogging. Such channels would be difficult to close from above, so I used a push-up geometry for valves [18], making operation of the device much easier.

That macrophages express a wide variety of receptors and respond to many types of ligands, which is what makes them useful cells to study, also makes them difficult to work with because they are very sensitive to environmental contamination. For this reason, I decided that I needed to minimize the possibility of cells being crushed by actuating valves. Unfortunately, scavenger receptors expressed on the macrophage surface [19], so critical for a macrophage's physiological function because they allow attachment to a wide variety of surfaces, frustrated all attempts at using surface chemistry to determine where cells could adhere to the device. Essentially, surface passivation with neither protein (BSA in this case, which is also present in the macrophages' suspension medium) nor with grafted poly(ethylene glycol) molecules [20, 21] was able to fully eliminate macrophage binding. The only approach left to me was to use streams of clean media to wash cells out of the

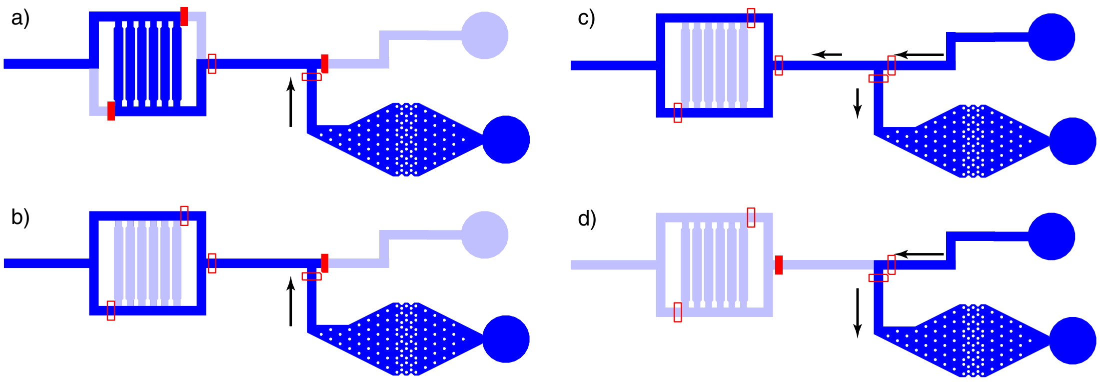

Figure 7.2: Scheme for loading cells into the device without inducing cellular damage. For clarity, all flow layer channels are shown in blue, with stagnant channels in light blue. The central cross channels correspond to feature 3 in fig. 7.1. (a) Initially cells are injected into the cross channels because the bypass channels are valved off. Because the flow is split several ways here, I drive it with a small pneumatic pressure (∼0.3 psi) to prevent cells from sticking near the stagnation points at flow branchings. (b) Opening the bypass channels equalizes pressures across the cross channels, so they no longer carry flow. Once this happens I can reduce the driving pressure to that arising from a small height difference between inlet and outlet (∼0.06 psi). (c) The media inlet is then opened; the fluid flow is strong enough to reverse flow in the cell inlet, so the entire system, with the exception of the cross channels, is cleared of cells. There is still some residual flow in the cross channels, resulting from fabrication errors that generate slight imbalances in the flow resistances between upper and lower branches of the bypass channels, but most cells still remain within the cross channels. (d) Flow into the cross-channel area can now be shut off, and the cell inlet can be further flushed with media. Note that, until this point, no valves have been closed.

valve areas.

At first, this approach seemed to pose a chicken-and-egg problem: to prevent all cells from being washed away, fluid flow must be stopped at those areas of the device designed to contain cells, *before* the washing process can begin. This is usually done by closing valves, but no valves can be closed before they are washed! The solution to the conundrum was to set up a flow regime where flow to certain channels is stopped by the *opening* of valves; this scheme is detailed in fig. 7.2 and demonstrated in fig. 7.3. Essentially, cells were dynamically trapped within cross channels in a bridge-like arrangement. I'll call these cross channels "cell channels" since they're the only place within the device that should have cells. The injection and wash process always took place at room temperature

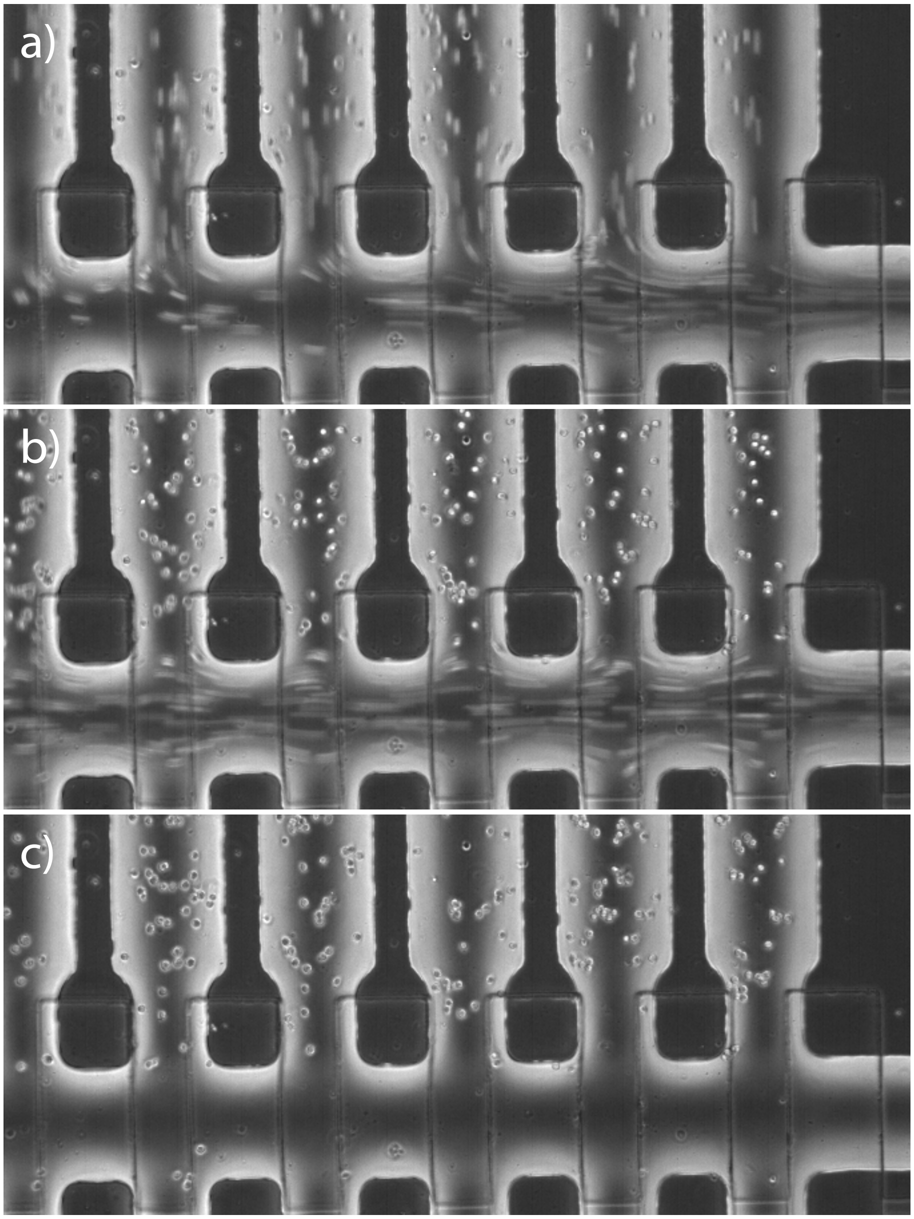

Figure 7.3: Phase contrast images of the cell seeding process. Relative flow velocities can be inferred from the length of the streaks that cells make as they flow by. (a) cells being injected into the cross channels. Note the progressively slowing flow in the horizontal feed channel going from right to left as more and more flow is being diverted to the vertical cross channels. (b) with the bypass valves open, the cross channels are mostly stagnant even though there is still strong flow in the horizontal feed channel. (c) the horizontal feed channel is cleared of cells by flushing with medium.

to minimize premature macrophage adhesion, which occurs much faster at 37°C. Even so, macrophages would start to adhere to channel floors within a fraction of a minute upon flow cessation, so the entire process was designed to keep fluid moving over valve areas almost until the very end of the wash; a computer program was used to coordinate valve actuations to achieve this.

In addition to scavenger receptors, RAW macrophages also express integrins, which are specifically designed for attachment to select substrate surfaces. Pretreatment of the PDMS surface with vitronectin or fibronectin, both of which bind integrins, enhanced adhesion, so that cells were rarely washed away by moderate flow; this pretreatment also provided a more physiological substrate which resulted in healthier cells. Because microfluidic channels had extremely large ratios of surface area to volume, the amount of protein that could be deposited onto the channel walls was quite severely limited by the concentration of protein used. In the end this caused me to use fibronectin, which is commercially available at a tenfold higher concentration than vitronectin, for the promotion of adhesion. Critically, strong binding between cellular integrins and the fibronectin adsorbed to the device walls took a little time to develop, so that cells stuck to walls only under conditions of little or no flow.

7.3 Control of dissolved gas and temperature

As noted above (§6.2), one of the reasons why PDMS is so convenient for cell biological applications is its high gas permeability. Controlling the dissolved gas content of cell media within the device can be achieved either by incorporating a gas-bearing serpentine channel in the device, or simply by blowing the desired gas mixture over the device (R.

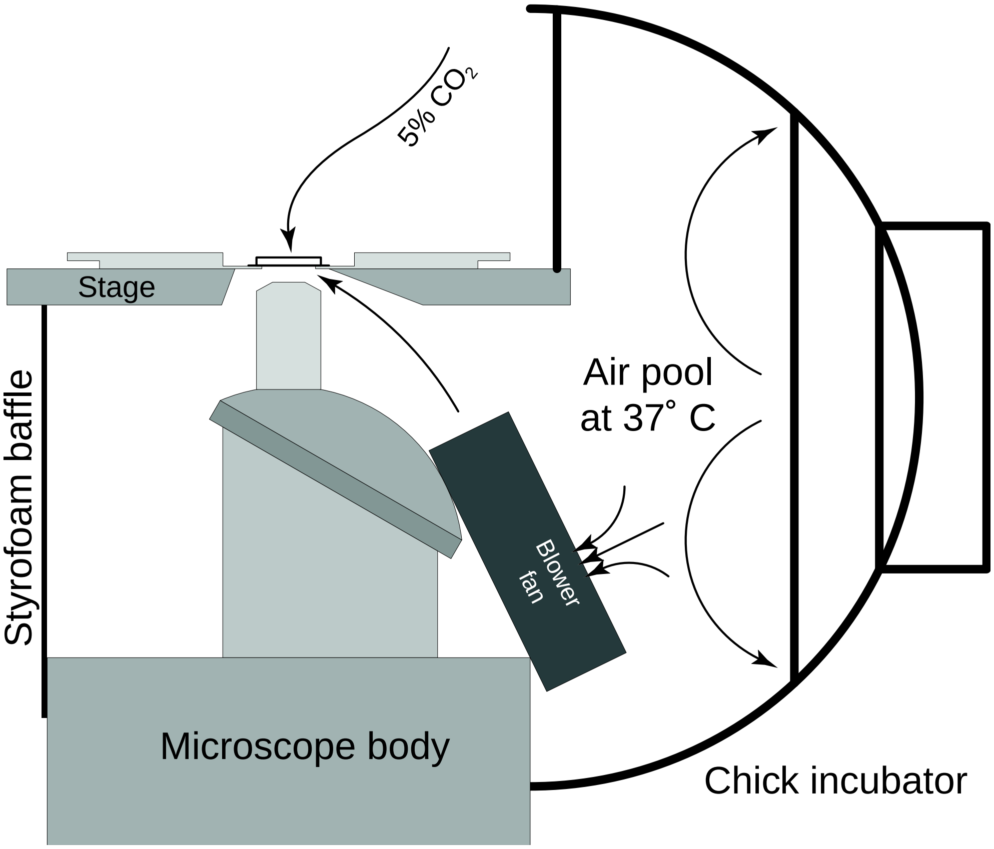

Figure 7.4: Because PDMS is gas-permeable yet thermally insulating, dissolved gas and temperature control are achieved from different directions. I control gas content via diffusion through the PDMS from above, and I control temperature with a heated air stream from below. Thermal baffles make a good enclosure in the space between the microscope stage and the bottom part of the microscope body; air in this enclosure is heated with a thermostatted chick incubator. Note that in the typical calcium experiment these two features are never used simultaneously; cells are perfused with a carbonate-free buffer during imaging (§8.2).

Gomez-Sjoberg, personal communication). Initial devices incorporated the gas channels, but they tended to make the device fabrication process both complicated and unreliable. Eventually I realized that this was not worth the relatively modest savings in gas mixture consumption, and I switched to using a small Teflon tube to blow a mixture of 5% CO_2, balanced in air, across the top surface of the device.

Temperature control of cells in the device was accomplished by heating from below, since that was the surface closest to cells ($\lesssim 200\ \mu$m, with the No. 1 cover slip and intervening PDMS). Typical devices were about 3 mm thick, so cells were at least ten times closer to the bottom surface. In addition, most of the material below cells was glass, which has a thermal conductivity roughly ten times higher than PDMS [22, 23]. This means that cells were in much better thermal contact with the bottom. Since I used a low-magnification air objective (10x, N.A. 0.3) with a long working distance, there was a good gap through which I could blow warmed air to set the temperature that cells experienced. A piece of temperature-sensitive liquid crystal film, placed on top of the microscope stage and insulated from ambient air with a piece of styrofoam, confirmed that the presence of the objective did not affect the temperature at the device. In typical experiments, the temperature control was turned on just after injection of cells into the device, so that the temperature had equilibrated throughout the microscope by the time the cells were ready for the experiment. For applications where larger magnifications and lower light levels compel the use of an immersion objective, temperature control may be effected through the objective by use of a heated objective collar.

Fig. 7.4 shows the scheme for temperature and dissolved gas control inside devices. Note that, since the PDMS above the microfluidic channels acts as a “blanket” for the cells, the top surface of the device can be exposed to ambient air. This meant that I didn’t need to enclose the device, so I had unfettered access to the device without sacrificing environmental conditions. Also note that the experiments were imaged with cells in a HEPES-buffered media that did not contain carbonate and hence did not require dissolved CO_2 control. In-chip culturing of cells for a normal experiment was on a slide warmer set to 37°C, and the device was transferred to the microscopy only in preparation for imaging. Thus, the setup as shown was used only for time-lapse photography of long-term cell culturing.

7.4 Control of shear

Many mammalian cells, especially vascular endothelial cells, are sensitive to shear stress [24–26]. Particularly relevant to our work with G protein-coupled receptors is the observation [24] that the β-adrenergic receptor, a GPCR, shows shear-dependent activation. This effect appears to be linear at low shear, saturating at higher shear with half-maximal activation at about 5 dynes/cm^2.

Actually, RAW264.7 macrophages seemed to be much more sensitive to flow on a time scale of hours: even at very modest shear stresses, orders of magnitude below the 5 dynes/cm^2 quoted above, they tended to stop dividing and die off within a day; only by slowing the flow down dramatically was I able to keep the macrophages alive for days on end. Approximating the macrophage shape to be flat against its adhesion substrate, I estimate that the shear stress in this case would apply an integrated shearing force on the cell of less than 1 pN! For comparison, a single kinesin motor molecule is able to move against about 6 pN before it stalls [27]. For this reason, I find it difficult to believe that it's the shear force itself which is causing increased cell morbidity and mortality. More likely is the possibility that RAW264.7 cells secrete factors, possibly proteins or peptides, into their surrounding media which are required for their own survival, akin to the "quorum sensing" observed in bacteria [28]. At higher flow rates the concentration of these factors cannot be built up because they get flushed too quickly, leading to cell death.

Because cells are sensitive not only to shear stresses, but also shear stress oscillations [29], I wanted to reduce flow transients as much as possible. Thus I decided against using the pumped metering scheme more typical of soft valve microfluidic devices [9, 30]. Controlling flow rate, then, simply came from the careful tailoring of both the force driving the flow and the resistance impeding it. Depending on the force required, flow could be driven by either air or hydrostatic pressure. Air pressure could be controlled by pressure regulators, but these were limited to rather high pressures since regulation was typically only good to within about 0.1 psi. Variations in input pressure and output flow rate would give rise to fluctuations in output pressure. Worse, depending on the particular regulator used, the output pressure sometimes depended on the *history* of output flow rate variations, so that the pressure applied was not reliable. In cases where lower driving pressures were required, I used hydrostatic pressure, whereby the height difference between the flow meniscuses at the flow inlet and outlet gave rise to a gravity-driven pressure difference; this pressure is about 0.1 psi per 7 cm height difference. Of course, by making use of hydrostatic pressure, I made the system sensitive to it, so that care had to be taken to maintain fluid meniscus heights at the desired level in the face of fluid flow which displaces those meniscuses.

Even with the relatively fine control over driving pressure afforded by hydrostatics, the flow rates in channels tended to be too high. Channel dimensions in most cases, as noted above, were dictated by the need to transport cells to the central observation area in the device, and tolerate flow of excess cells through the channel to the waste port. Now, for a channel much wider than it is tall, the surface stress is given by eq. A.4: $\sigma = Gh/2$, with G being the pressure gradient and h the channel height. Spreading the 0.1 psi pressure difference over a channel length of 40 mm, the longest flow path in my device designs, still gave a resulting shear stress for a 50 μm high channel of a few dynes/cm^2.

Fortunately, impeding flow in microfabricated devices was straightforward. Recall that the flow rate through a pipe scales as the *fourth* power of the pipe's cross-section size [31]. I could thus use modestly thinner sections of channels to dramatically reduce the flow rates, and by extension the shear stresses, in the other parts of the device. In terms of fabrication, this meant defining those channel sections with a thinner layer of photoresist. I didn't need to gate channel flow in the thinner sections, so I used SU-8 photoresist for this purpose because of its fabrication ease, versatility of thickness, and durability. Flow constrictions so constructed were about 5 times thinner and 10 to 20 times narrower than the normal channels, yielding at least a thousandfold increase in the flow resistance per unit length. To avoid cell clogging, I simply kept these flow constrictions away from the flow path of the cell suspension. The thin flow constriction (feature 2 in fig. 7.1) slowed down media flow to give rise to the minuscule shear stresses quoted above.

In addition to moderating the flow rate, flow constrictions also had the virtue of concentrating fluidic resistance to very small portions of the device. Thus, variations in flow resistances across the rest of the device had basically no effect on the overall flow rate. This became important because it was difficult to accurately control AZ-100 photoresist thickness over the centimeter-size length scales of the finished device designs (Appendix B), whereas thin SU-8 spins gave very uniform photoresist thicknesses that also tended to stay uniform through all stages of wafer processing. Further, with flow constrictions in place, the flow rate became independent of the presence of cells which presumably increased flow resistance in the channels to which they adhered. In direct analogy to a large electrical resistor, the flow constriction became the dominant resistance in the system and, coupled with a stable driving pressure, gave rise to a fluidic current source.

This idea of making a fluidic current source was also useful in trying to make as uniform as possible the conditions across the different cell channels that were to contain different experiments. Again, by putting most of the resistance, and hence most of the pressure drop, across flow resistors, I could equalize flow rates through the different cell channels and also make them independent of partial clogging by the presence of cells in those channels. This accounts for the set of flow resistors downstream of the cell channels (feature 4 in fig. 7.1).

Finally, to ensure that most cells within the same channel experience the same shear stress due to fluid flow, I used a non-rounding photoresist to form the cell channels. Channels were defined in the photomask to be 200 μm wide and, as fabricated, were between 25 and 30 μm high; edge effects are only expected (eq. A.18) within 20 μm or so of the side walls. The thickness of the channels appears dangerously close to the size of the cells I'm using, but to date I have not seen any problems with channel clogging; indeed only rarely have cells adhered to the tops of the channels, suggesting that they are not being squeezed through the channels.

7.5 Solution freshness

The astute reader may have wondered why the fluidic resistors balancing flow across different cell channels were placed downstream of the cell channels, instead of upstream between the cell channels and the offset shunt (see below). This alternate placement would still keep the resistors out of the direct stream of suspended cells, and would also effectively isolate the cells from any upstream pressure changes. The cell channels would, to use another electrical analogy, be "shorted to ground" and kept at zero pressure. In the present devices, pressure changes of the scale that I could practically apply would probably not have a direct effect on cell physiology, but they could still deform the cell channels (PDMS being very compliant) and thereby induce small flow transients.

In fact the flow resistors were initially placed upstream of the cell channels, in the location I just alluded to. The reason they were moved was that PDMS is very hydrophobic and will readily absorb small hydrophobic solutes as well as adsorb proteins [32, 33], presumably by interacting with their hydrophobic cores. This becomes a real problem when PDMS microdevices are used for pharmacological studies [33] such as the ones I have performed; I have therefore tried to minimize hydrophobic solute depletion as much as possible in the device designs.

Let's consider roughly how this effect scales with channel dimensions. It seems reasonable that, for the same cross-sectional area, the minimum adsorption will occur with a channel of aspect ratio unity, i.e., one as wide as it is tall. There are thus only two geometrical parameters to worry about: the width w and length l of the channel. We also have flow rate ϕ, which is to be kept constant, and a diffusion constant D for the solute under consideration. Fick's law of diffusion tells us that the time τ it takes for the solute to diffuse from the center of the channel to a wall scales as $\tau \sim w^2/D$. The time T it takes for flow to travel through the pipe scales as $T \sim lw^2/\phi$. We can just take the ratio of these two to get a figure-of-merit f for how accessible the walls are to solutes in the channel. Thus

$$f = \frac{T}{\tau} \sim \frac{LD}{\phi} \tag{7.1}$$

is independent of w. Adsorption to the walls just gets progressively worse as the channel increases in length. Note also that smaller ligands are doubly affected: they are more liable to dissolve into the nanoporous PDMS matrix, and they arrive at the PDMS faster due to diffusion.

This computation implied that I needed to decrease the channel *length* upstream of the cell channels. As is I had to make the constricted channels snake back and forth to get the required resistance, so I felt it would be best to connect the offset shunt (feature 5 of fig. 7.1) to the cell channels with straight channels and put the serpentine resistance channels downstream. Such an arrangement also meant that solutes would not experience high shear until after they flow over the cells — some protein solutes may be shear-sensitive.

The offset shunt was necessary because solutions had to be primed into their respective inlets before they could be used, lest air bubbles get into the system and destroy the experiment. The priming process usually took between 10 and 20 min, during which the solution crept along the channel very slowly. The solution that primed a given channel, then, had ample opportunity to have all its small hydrophobic solutes diffuse into the PDMS matrix. In addition, many of the ligands I used were sensitive to heat. The protein fragment C5a, for instance, degrades at 37°C, so AfCS protocols involving C5a stimulation keep the ligand on ice and warm it to physiological temperature just prior to its addition to cells. Because of the small dimensions involved, keeping solutions cool inside devices while heating cell-bearing areas was rather impractical.

What resulted, then, were plugs of depleted and degraded solution in the device's inlet channels with fresher solution upstream in the microbore tubing. These stale solution plugs were directly upstream of the cell-bearing portion of the device, and if allowed to reach the cells would do so in the critical first few seconds of ligand application when the cell was starting to respond to the ligand. Clearly what was required was some way of siphoning off the initial plug of stale solution, freshening the solutions in the microfabricated channels just before applying them to cells; a bypass shunt line connecting these inlet channels directly to the waste line did just that. As noted above, PDMS is a decent insulator, so that even as the lower part of the device was being heated to physiological temperatures, the top side of the device, as well as feed tubes that are inserted into the de-

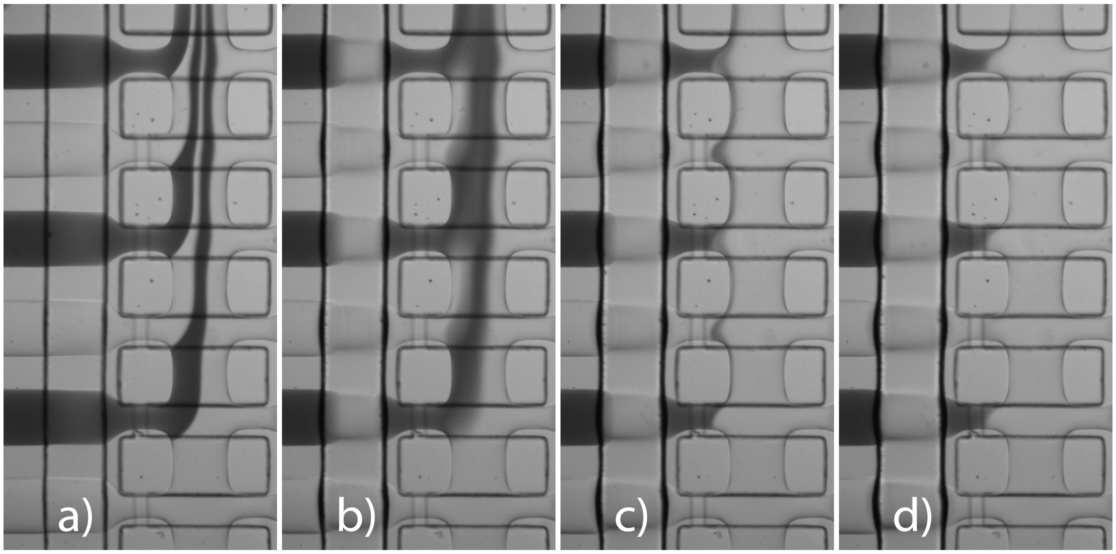

Figure 7.5: Shunting of solutions, demonstrated with colored dye solutions. Solutions are pressurized to be injected in from six channels on the left (these would contain stimulating ligands in actual experiment), and in the channel from the bottom. The cell area would be to the right, connected by short channels to the shunt area. The outgoing channel on top connects directly to the waste channel. (a) Solution in all channels on the left flow into the shunt. Media from the bottom channel, being topologically the ”rightmost” inside the shunt line, forms a barrier that prevents ligands flowing in from the left from diffusing towards cells. (b) Once ligand access channels are closed, the ligand flow stops, and the boundary between flow streams blurs due to diffusion. (c) The shunt area can be flushed with clean fluid from below, so that by (d) there is very little cross-contamination between channels.

vice, could stay cooler. In experiments presented below, feed tubes were kept at ambient temperatures, but in the future adding extra cooling should be straightforward.

Having to clear six different inlet channels that were in very close proximity complicated things a bit. I really didn’t have the space to put a separate shunt line for each inlet; in any case each shunt outlet would have required its own port due to flow routing issues. Instead I used one shunt for all the inlets, and had to deal with the resulting cross-contamination. To keep the shunted fluid away from susceptible cells, and to avoid having to open and close valves in close proximity to those cells, I placed the shunt line a small distance upstream of the cell areas. The shunt line was also allowed access to the plain media stream, which would block ligands from diffusing or flowing into the cell areas.

The media stream would also wash out the shunt area prior to ligand application. These two functions both contributed to reducing cross-contamination. The shunting process is shown in fig. 7.5.

With the shunt in place, the first plug of ligand to reach cells should be quite fresh, having been inside the PDMS device for no longer than a few seconds. The shunting flow rate could not be sustained once individual inlet channels were connected to their respective cell channels, since cell channels have downstream flow resistors; in any case the high flow rates would apply a large shear stress on cells. The flow thus settled down after being connected to cell channels, and the situation became as described above with solute adsorption; we can thus use device parameters to estimate the figure of merit f for channel adsorption. The flow rate was about 2.5 nl/s. Diffusion constants for ligands varied, but approximating ligands as spheres of hydrodynamic radius 1 nm gives a diffusion constant of about 200 $\mu\text{m}^2/\text{s}$. The longest upstream inlet channels were about 12 mm from the inlet port to the cell area, which yields f of order unity. Thus significant depletion could eventually be expected with smaller hydrophobic ligands such as platelet-activating factor (PAF; see §6.3).

Several things to note here:

- The depletion will not be immediate. Flow rates during the shunting process can reach 1 μl/s, giving a thousandfold lower f. The resulting plug of unaffected ligand is the one that triggers the initial signaling in cells. Since the *entire* inlet channel is filled with fresh ligand, the time it takes to refill that channel at the lower flow rate (given that f is about unity) is a good estimate for the decay time of ligand concentration. Channel volumes are about 70 nl, so it will take 30 s or so for the ligand depletion effects to arise. Initial peak responses to ligands will typically be over by then.

- In the context of experiments testing for signaling kinetics rather than binding affinities, extended exposure to ligand is necessary. However, I could just use saturating concentrations of ligand so that depletion into the PDMS does not significantly alter receptor activation.

- This is by no means a general solution to the problem of solute adsorption in pharmacological applications of PDMS microdevices. All of my experiments occur over a timescale of minutes (see Chapter 10), and cells are killed anyway at the end of experiments by the calibration process, so that the long-term cytotoxic effects of shear flow, described above, do not constrain the flow rate I can use. Even so, there appear to be time-dependent effects (§10.1.1) that might be attributable to the high flow rates used during the experiment. The flow rates I use in experiments may not, in general, be sustainable for longer periods of time without causing damage to the cells being studied.

- The consideration here is only for solution in the center of the channel, whereas the cells that respond to ligand are attached to channel walls. Concentrations that the cells see will probably be affected by (ad/ab)sorption at the wall areas immediately upstream of those cells; future experiments should be performed to compare signaling performance with cells attached to glass *vs.* cells attached to PDMS. Again, this is expected to have more of an effect on small, hydrophobic ligands such as PAF and lysophosphatidic acid (LPA).

Chapter 8

Cell handling

8.1 Preparation of cells for injection

RAW264.7 macrophages were cultured on plain polystyrene plastic dishes that had not been treated for tissue culture use. The macrophages stuck to the dishes via their scavenger receptors, but not very strongly, and a day or so after being seeded in a new dish would mainly be found growing in clumps; this also seemed to happen more as cells senesced after many rounds of division.

Usually cells could be washed directly off the plastic dish surface by streaming over them the media that they were cultured in. The cell-containing media was transferred to a 50 ml Falcon centrifuge tube, and the plastic dish further washed with 3 ml phosphate-buffered saline (PBS), supplemented with 5 mM EDTA to chelate the calcium that helps macrophages adhere. This solution, which might contain the more adherent cells that were not removed by the first wash, was also transferred to the centrifuge tube, and the mixture centrifuged at 300×g for 5 min to pellet the cells. The media was aspirated, and the tube tapped vigorously to mechanically disrupt the cell pellet. The pellet was resuspended with 1 ml of PBS supplemented with 10% fetal bovine serum, yielding a suspension of cells with a reasonably low amount of clumping; most clumps at this stage were of 5 or fewer cells.

From this suspension, 10 μl were taken off to be counted in a hemacytometer, and the rest pelleted by centrifuging at 14000 rpm for 10 s in an Eppendorf model 5415C tabletop microcentrifuge. The supernatant was again aspirated, and the pellet disrupted by tapping and then resuspended. This time it would be resuspended in PBS with 5 mM EDTA, which prevents cell-cell adhesion and thus makes a more monodisperse suspension of cells. The suspension volume was adjusted according the cell count to yield a cell density of 70000 per μl.

Before this could be injected, though, the calcium had to be replaced since it is essential for integrin binding to fibronectin and hence for the adhesion of cells to the channel floor. This was done just before injection by doubling the suspension volume with addition of Leibovitz's L-15 media (specially formulated to support cell survival and growth in the absence of carbonate), supplemented with 4 mM L-glutamine, 20 mM HEPES, and 10% fetal bovine serum, to which 5 mM $CaCl_2$ and 5 mM NaOH were added. The added calcium should just completely saturate the EDTA in the original suspension, and there would be enough extra calcium in the L-15 media and fetal bovine serum to support macrophage adhesion. The NaOH was necessary to preserve pH balance since binding of Ca^{2+} to EDTA releases one equivalent of acid. Because prolonged exposure to EDTA has deleterious effects on cell physiology, cells were resuspended with PBS/EDTA just prior to addition of the L-15 media. The resulting suspension, at 35000 cells per μl, was enough to yield about 250 cells per cell channel of 7 nl and was injected immediately upon mixing to reduce cell clumping that would result from the presence of extracellular calcium. Indeed, visible clumps of cells usually appeared inside the cell suspension feed tube by the end of the injection process.

8.2 Seeding and stimulation

Seeding of the suspension proceeded as described in §7.2, at room temperature. After injection, the device, with its holder, was transferred to a slide warmer set to 37°C. Cells were kept with no flow for about 15 min, during which time they adhered to the fibronectin-coated channel floor, and after that a small but steady flow of RAW growth media (RAWGM; see §C.1) was applied to wash in nutrients and wash out metabolic waste.

A stream of 5% CO_2, balanced in air, was also applied to the device at this time, since the RAWGM contains carbonate ions and thus is dependent on carbon dioxide control for pH balancing. Under these conditions, cells could typically be cultured for more than 72 hours (fig. 8.1). They probably start to get sick as the cell density increases; passaging cells to control for density is impractical in a microfluidic device. Usually experiments were carried out after between 2.5 and 4 hrs of incubation, so that cells were attached firmly and, indeed, often spread out onto the PDMS substrate, but their health, as determined by the distribution of basal calcium levels, had not been compromised (data not shown).

After this time, cells were washed for 1 min with the experimentation buffer HBP (short for HEPES-HBSS-BSA-Probenecid; see appendix C.1), supplemented with 2.5 μM fluo-4 AM (Invitrogen), which is a membrane-permeant ester of the calcium-sensitive dye fluo-4. Once the ester crossed the plasma membrane, cytoplasmic enzymes would cleave off the AM group and trap the dye within the cytoplasm. According to the manufacturer's product information, uptake of free dye into subcellular compartments is reduced at lower temperatures, so the device was taken off the slide warmer and allowed to cool back down to room temperature just before the start of staining. The 5% CO_2 stream was also stopped at this time, as HBP does not require it for pH balancing. Staining occured for 30 min, after

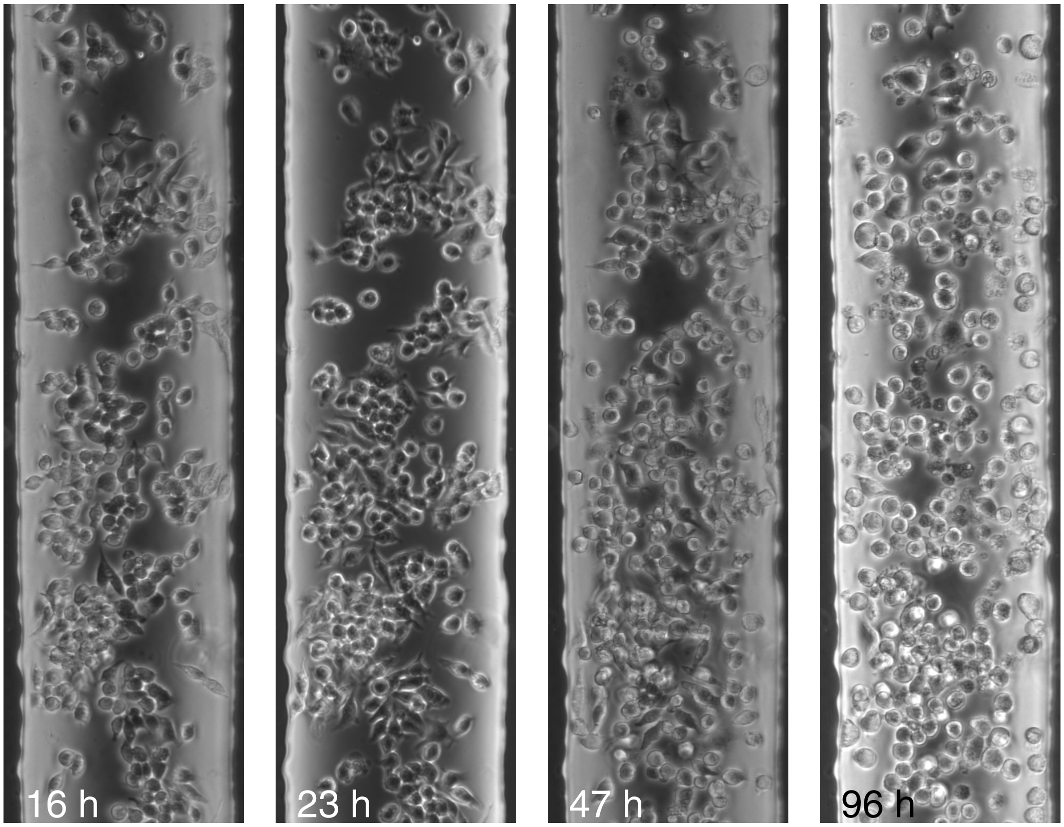

Figure 8.1: Phase contrast images of cells inside a microfluidic for long periods of time; all these images are of the same location inside the same device. By 96 hours, most cells have rounded up, and that there is already significant cell death. Note that cell division rates are quite a bit lower than in tissue culture dishes, where doubling times of 13-16 hours are normally observed.

which cells were washed with fresh HBP.

Because the stimulation and calibration solutions were susceptible both to thermal decay and depletion of solutes due to ad- and absorption, they were not introduced to the device until this time. These solutions were prepared during the staining process and primed into hitherto empty channels in the device in preparation for the stimulation experiment.

After the fluo-4 was washed out, the device was placed onto the microscope, which has been preheated for $\sim$3 hrs and had a warmed air stream to heat the device back up to 37°C (fig. 7.4). The cells were further incubated under these conditions for 25 min before starting the experiment, to complete dye de-esterification (again per manufacturer's recommendations), to allow cells to recover from the room temperature staining process, and to allow its holder to thermally equilibrate, reducing the amount of mechanical drift during the experiment.

Experiments were started by flushing cells with plain HBP buffer for 4 min, after which flow was switched within the device to wash cells with the ligands of interest. During this time there was a steady perfusion of solution driven at 0.5 psi with air pressure, so that for the most part cells experienced a shear stress of a few dynes/cm^2. When stale ligand solutions were shunted to waste, however, I had to shut off flow to the cell area lest those solutions reach cells prematurely, so that flow over cells was stagnant for a few seconds prior to stimulation. Further, I wanted to stimulate all cells more or less at once, so initial application of ligand to cells was performed at 4 psi driving pressure to reduce the difference in ligand arrival times to upstream and downstream portions of cell channels. While the flow itself did not trigger calcium release, as evidenced by the calcium time series data from the negative buffer control channels, it may still have affected the signaling apparatus and modulated calcium release.

Chapter 9

Data acquisition and analysis

9.1 Optical imaging

For reasons delineated above, I chose to use a "push-up" geometry for valves, so that the cell-bearing flow layer is entirely encased in PDMS. Fortunately, PDMS is optically clear in the visible spectrum, with minimal autofluorescence. Its index of refraction of 1.4 [22] is close to the standard cover glass index of 1.515. Imaging through the PDMS, then, entailed no extra effort and no sacrifice of optical quality. Moreover, the microscope objective that I used was one with a relatively long working distance and hence much less susceptible to aberration from increasing the effective cover glass thickness. To further reduce the potential for aberration, I constructed devices atop No. 1 cover slips, which are generally about 60 μm thinner than the No. $1\frac{1}{2}$ cover slips for which microscope objectives are designed. Any residual thickness problems could be corrected with high N.A. objectives' correction collet, but I have not seen the need even when imaging at relatively high powers.

Data throughput and light collection efficiency were two design parameters that worked against each other. Clearly, data throughput depended on imaging as large an area as possible, which, with a fixed detector size (indeed, a fixed microscope field number), meant reducing the magnification. As in fig. 3.2, the objective and tube lens (L_2) form a telescope that images an object onto another focal plane F. In a standard microscope the tube lens focal length and position are both fixed, so the magnification $m = f_2/f_{\mathrm{Obj}}$ is changed through varying f_{Obj}. The beam radius coming out of the lens is $r = f_{\mathrm{Obj}} \tan\theta$, where θ is the half-angle subtended by the lens; the numerical aperture (N.A.) of the lens is $\sin\theta$. For θ small we have $r \simeq f_{\mathrm{Obj}} \times \mathrm{N.A.} \sim \mathrm{N.A.}/m$. The maximum beam radius r we can have is set by the microscope's tube size, so unless I resort to custom optics any decreases in magnification must be accompanied by decreases in the N.A. For small N.A. the light collection efficiency scales as the square of N.A., so that any increase in detection area has to result in a decrease in optical sensitivity. It is for this reason that I tried to pack as many independent cell channels as possible into a small area.

In practice, the use of a 10× objective (N.A. 0.3) gave the best compromise between imageable area and light sensitivity. All calcium experiments were imaged with the 10×/0.3 objective in a Zeiss Axiovert 35 inverted microscope with a field number of 18 mm; the image was formed onto a Hamamatsu Orca 285 CCD camera via a 2× reducing coupler, so that most of the observable field could be imaged onto the CCD. This arrangement allowed imaging of about 1000 well-separated cells per experiment.

9.2 Instrument control and data acquisition

Water-filled pneumatic microvalves [11] within the device were driven with electrical solenoids (Precision Dynamics and Clippard) switching pressurized air, typically regulated to 25-30 psi. Solenoids were driven with custom-build electronics, which also controlled power to the bright-field illumination halogen lamp via a solid-state relay.

Data acquisition was orchestrated by a dedicated computer which communicated to the solenoid valve driver circuits via a combination of parallel and USB ports, to the camera via an IEEE1394 (FireWire) link, and to the shutter driver via a serial link. Frame acquisition would begin with the computer issuing a command to the shutter driver to open the shutter. The fluorescence illumination shutter (Uniblitz) had a built-in optical interrupt mechanism to indicate shutter opening; as soon as the shutter opened, this sent an electrical TTL pulse to the camera and triggered the start of camera integration. A custom-built, settable timer closed the shutter after the camera was finished integrating. Once integration was complete, the frame was transferred to the computer, which, depending on how quickly frames were being acquired, either stored it in memory or wrote it to disk. Data was written directly to a scratch partition to avoid filesystem overhead. Because all the trigger timings were generated by computer, they could be varied with ease, and each shutter open command issued by computer was timestamped to allow correlation with the captured frames during analysis.

After the first minute of HBP flow at the beginning of each experiment, I would start to take pictures with the CCD camera while withholding fluorescence illumination; this gave each experiment a camera background data set. After the dark frames, I would further take 12 frames with fluorescence illumination, once every 5 s, without changing buffer conditions, to give basal calcium measurements for the cells. At the start of agonist application I usually temporarily increased the frame capture rate, to avoid losing sight of some of the fast events that occur at the beginning of a cell's agonist response, but slowly ramped the capture rate down again to minimize photodamage. The CCD camera, a cooled Hamamatsu ORCA-285, could transfer frames to the computer at speeds as high as 5 frames per second, though 2 fps was typically more than fast enough (frame exposure times were 16.667 ms and thus not framerate-limiting).

Since cells displayed a wide range of staining intensities, and since fluo-4 without Ca^{2+} bound still fluoresces faintly, at the end of each experiment the staining characteristics had to be measured. This was accomplished by flushing all cells with two solutions: one designed to remove all calcium from the cytoplasm (the ”min” solution), and another to massively deliver calcium to the cytoplasm to saturate the calcium indicator dye (the ”max” solution; §C.2).

I also took a bright-field, phase-contrast image of the cells in the device both at the beginning and the end of each experiment. This allowed confirmation that features identified were indeed cells, and also may provide extra information to be incorporated into future cell identification algorithms. For instance, my current cell detection algorithm can misidentify cell clusters as single cells; perhaps some sort of edge detection algorithm applied to the bright field image may be used to identify cell boundaries and separate cells within a cluster.

9.3 Data analysis

For each experiment, a map of where the cells should be was first generated by subtracting an averaged “min” calibration image from an averaged “max” calibration image. This is expected to select out only regions that exhibited calcium-dependent fluorescence, i.e., only regions with significant fluorescence from the calcium-sensitive dye being used. The intensity map was further corrected by rescaling to a fluorescence image taken of a uniformly fluorescent plastic calibration slide (Chroma), to adjust for nonuniformities in the fluorescence excitation illumination as well as vignetting and clipping effects from emission image formation.

The corrected intensity map was analyzed using an adaptive watershed algorithm, where contiguous regions of intensity above a certain cutoff were identified as candidate features. The cutoff started at some low basal level, and the algorithm tracked the evolution of the candidate features as the cutoff was raised gradually. As the cutoff was raised, identified regions would slowly shrink until they either split off into separate islands or disappeared entirely. Any given island that disappeared was tracked back to the first threshold at which it split off from something else (or the starting threshold, if that never happened), or the first threshold at which its size fell below some maximum size cutoff, whichever happened last, and its shape at that threshold became the final shape of the identified feature. I assumed that the cells remain immobile over the course of an experiment, so intensity time points for each feature were calculated by summing pixel values over feature regions for each image. Further quality assurance was performed at the time trace level to remove cells that were either too faint or too sick to yield reliable data. Finally, channel shapes were identified by eye and entered via a graphical interface so that the analysis program could group calcium traces by the cell channel from which they came.

For any given data set, the analysis takes about ten minutes to run on a PC with an AMD Athlon XP processor. The data analysis program was custom written, in C for the computation-intensive image analysis and in Common Lisp (CMUCL) for downstream time trace analysis and data display and collation; the analysis code is available on request from the author.

Free calcium concentrations could be inferred from the image intensity data by assuming that the minimum intensity I_{min} represents all unbound indicator molecules, and that the maximum intensity I_{max} represents all bound indicator molecules:

$$\left[\text{Ca}^{2+}\right](t) = k_D \frac{I(t) - I_{\text{min}}}{I_{\text{max}} - I(t)}, \tag{9.1}$$

where k_D is the calcium binding constant for the indicator dye. There have been some conflicting reports about k_D for fluo-4, with the manufacturer giving a value of 345 nM [34] but another lab reporting a wildly different 520 nM [35]. In addition, the same lab reports a much lower k_D of 190 nM at 37°C than at 22°C! For this reason, because data scatter tends to get problematic at high calcium concentrations due to dye saturation, and because the absolute calcium concentrations are not really the salient measurement here, I will give experimental data as normalized fluorescence values

$$\hat{I} = \frac{I - I_{\text{min}}}{I_{\text{max}} - I_{\text{min}}} \tag{9.2}$$

with the understanding that they can be easily converted back:

$$\left[\text{Ca}^{2+}\right] = \frac{k_D \hat{I}}{1 - \hat{I}}. \tag{9.3}$$

Chapter 10

Results

10.1 Quality control

10.1.1 Internal statistical consistency

Many engineering challenges were tackled with one payoff in mind: to be able to perform different experiments under (ideally) identical conditions and thereby be able to compare their results with confidence. The natural first question to ask, then, is whether that is actually the case. This can be tested by comparing the outcomes of different channels that have been subjected to the same stimulus. For a typical dataset, such as one that stimulated three channels with 10 μM UDP, I can compare the actual standard deviations between the individual channels (0.011) with the standard errors derived from cell population statistics within each channel (ranging from 0.008 to 0.014). After all, the standard error of the mean of a data set is meant to tell how far off, on average, the observed mean of that data set is from the true mean of the distribution from which its members are taken. If the assumption is that the cells in each channel are indistinguishable, i.e., their properties are drawn from the same distribution, then the standard deviation of channel means should be close to the standard errors within each channel.

Fig. 10.1 shows this comparison for all experiments where such comparison is possible.

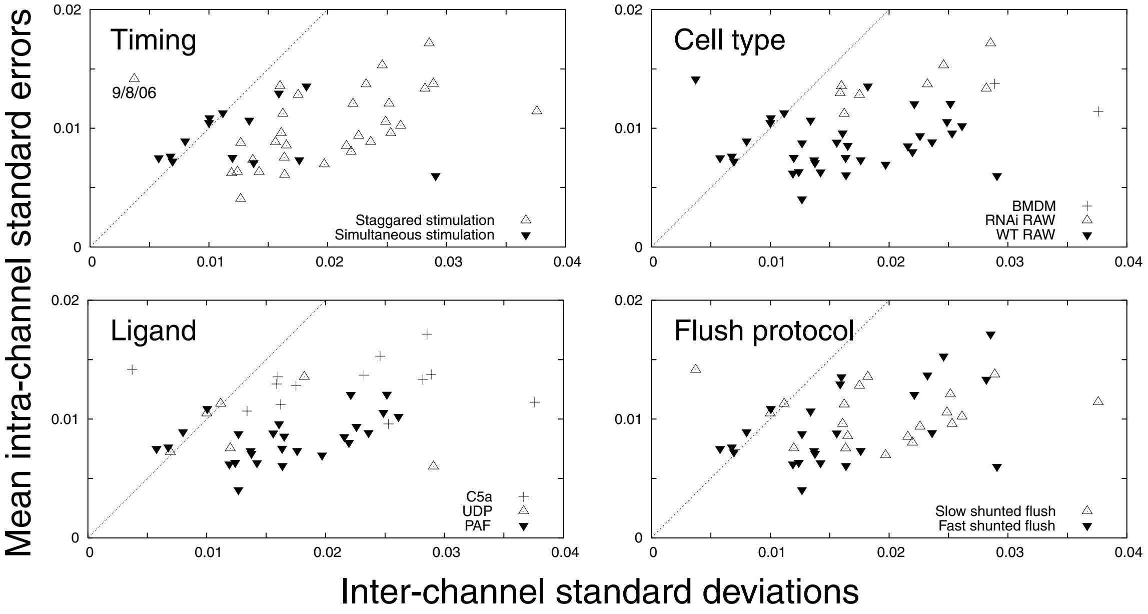

Figure 10.1: Comparing the standard deviation between channels to the standard errors within channels allows us to ask whether cells from different channels behave differently; see text for explanation. The different panels break the same data down according to different aspects of the experiments. Note that this is an entirely post-hoc analysis, so no attempt was made to be systematic in the data.

It also breaks the data down in several different ways to look for potential sources of variability. Reasonable agreement between these statistics does appear to be the norm in most experiments, though almost all experiments exhibited higher inter-channel standard deviations. These might be due to subtle effects resulting from differences that were unavoidable between channels, including differences in illumination intensity, channel height, and downstream flow resistance. Looking closer at the categorization, a few more patterns start to emerge:

- Either C5a, or infection with viruses expressing shRNA (labeled ”RNAi” in the upper right panel), gave rise to more variability; since their overlap is so large it is hard to distinguish between the two hypotheses. Either explanation is plausible: C5a always gave a less homogenous response, with large non-responding populations; shRNA expression from viral infection also tended to be nonuniform and could increase the scatter in the data.

- Roughly halfway through taking the data shown here, as a part of continuing improvements in device function, I increased shunting flow rates and thereby increased the degree to which stale input ligands were shunted to waste (§7.5). This didn't seem to have significantly altered either cellular or channel-wise variabilities (lower left panel).
- Simultaneous stimulation of all channels seemed to give more uniform results across channels. This indicates that cellular responses may change over the course of an experiment and is corroborated by other data (§10.4).
- There is a definite paucity of data here, but it appears that bone marrow-derived macrophages (BMDMs) gave higher intra-channel standard errors; this is probably because they gave stronger responses. They also gave higher inter-channel standard deviations.
- Most data points lie between lines of unity slope and slope 0.4. Thus, while they were still significant, systematic errors between channels were of similar magnitude as stochastic errors.

10.1.2 Data uniformity

Another central assumption in these experiments is that cells within each channel differ due to their internal states, and not due to their positions within those channels. A simple analysis correlating cellular responses to positions (fig. 10.2) supports this assumption. Both along and across the channel, there is apparent uniformity in the response distribu-

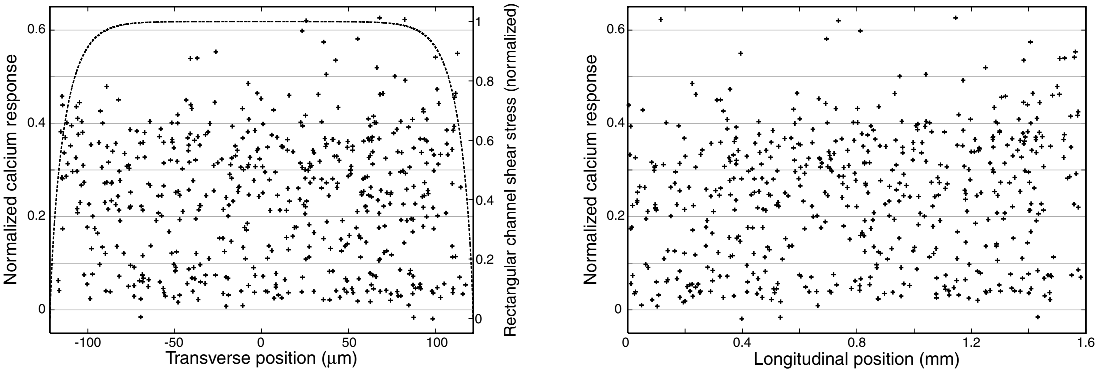

Figure 10.2: Plotting single cell responses (peak C5a-induced calcium concentration) against cell position either across the channel (left) or along the channel (right) shows no clear dependence in either case. Left panel has the estimated shear stress distribution plot superimposed on the data, to indicate that even within the zones of wall-induced shear stress depression there doesn't seem to be any change in cellular responses.

tion. This is confirmed by trying to fit data from the two graphs to straight lines: r^2 from the longitudinal fit is about 2%, and that for the transverse fit is less than 10^{-4}. Fitting the cellular response to the *square* of the transverse position, looking for effects of shear stress depression which are expected to affect cells near the channel periphery verses cells near the channel center, also gives a very low correlation: $r^2 < 10^{-3}$. Thus, variations in position account for at most 2% of the variability in cellular responses.

10.1.3 External consistency

The last way of testing the function of the devices is to compare device-derived experimental data with data from another source. The microscopy lab of the AfCS at Stanford generated single-cell resolution data sets for single ligand stimulations, directly analogous to single-stimulation data shown here that were acquired within microfluidic devices. Comparisons of response distributions to two different concentrations of UDP are shown in fig. 10.3.

Responses to saturating concentrations of UDP appear to be mostly similar, with a

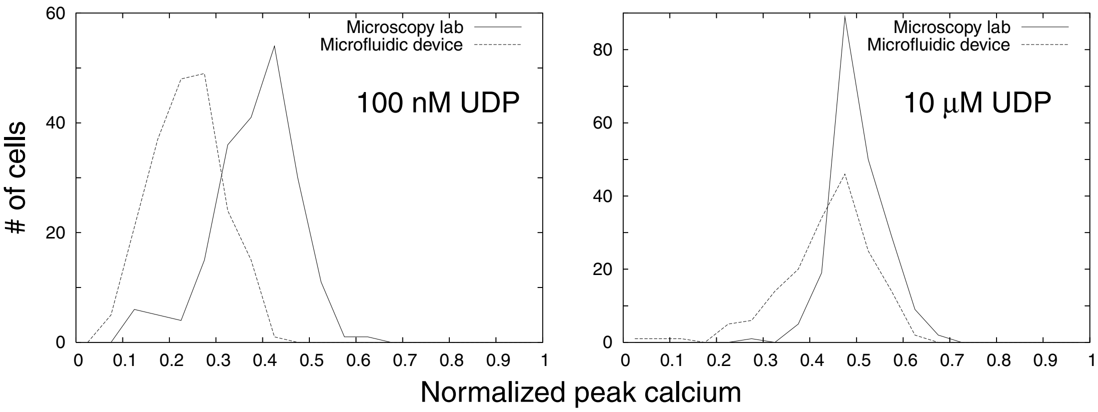

Figure 10.3: Comparison of response distributions after treatment of cells with 100 nM and 10 μM UDP. Histograms were not rescaled since they included similar numbers of cells. Microscopy lab data were generated using ratiometric imaging of cells stained with fura-2; the calcium concentrations so derived were converted to equivalent fluorescence values for fluo-4 to allow direct comparison with microfluidic data. Large-well data were kindly provided by Dr. Grischa Chandy.

larger spread in the microfluidic device. At a hundredfold lower concentration of UDP, however, cells in the microfluidic device gave significantly lower responses compared to those in large wells. One caveat here is that experimental results vary depending on the particular batch of cells used, and probably also the passage number. In addition, the Stanford data were acquired using a different calcium-sensitive dye, fura-2, and with ratiometric imaging, whereas the microfluidic data were acquired with fluo-4 using simple intensity measurements. These differences notwithstanding, that the 10 μM UDP results were so similar tends to indicate that the differences seen at 100 nM UDP are real.

One possibility for this discrepancy could be that cells were actually exposed to different concentrations of UDP in the two cases. Experiments in large wells usually involve adding a volume of concentrated ligand to the buffer solution already on top of the cells; the procedure (§C.1) calls for doing so gently, presumably to prevent the fourfold-concentrated ligand from reaching cells before being diluted by the surrounding solution. Such a possibility could explain the discrepancy seen, but would probably also have increase the scatter in the large well data; such a large scatter has not been reported. On the other hand, degradation of UDP before it arrives at cells within the microfluidic device is still a concern, despite the lengths (§7.5) to which I have gone to suppress it. For this reason, most of the experiments I have performed with the microfluidic device were performed at saturating ligand concentrations.

10.2 Calcium store depletion

The past year has seen much attention paid to the molecular mechanisms behind a cell's uptake of extracellular calcium in response to depletion of internal stores, due to recent experiments identifying key molecular players in the process [36–40]. These advances show a fascinating picture of inter-organelle communication, rather beyond the scope of this work. For my purposes, because much of the new data generated by the microfluidic experiments were obtained through repeated stimulation of cells (§10.3 and §10.4), I needed to characterize the calcium store depletion and replenishment kinetics without necessarily addressing the molecular mechanism behind these processes.

The extent of store depletion could be assessed at the end of an experiment by looking at the kinetics of minimum calibration. The minimum calibration buffer contained thapsigargin, ionomycin, A23187, and EGTA. Thapsigargin is an inhibitor of SERCA, the sarco/endoplasmic reticulum calcium pump responsible for maintaining the calcium gradient between the cytoplasm and the ER. Its presence allowed emptying of the ER stores into the cytoplasm via calcium leakage [41]. Ionomycin and A23187 are ionophores that permeabilize the plasma membrane to calcium ions, so that the calcium chelator EGTA outside the cell could drain the released ER calcium out of the cytoplasm. Since most of

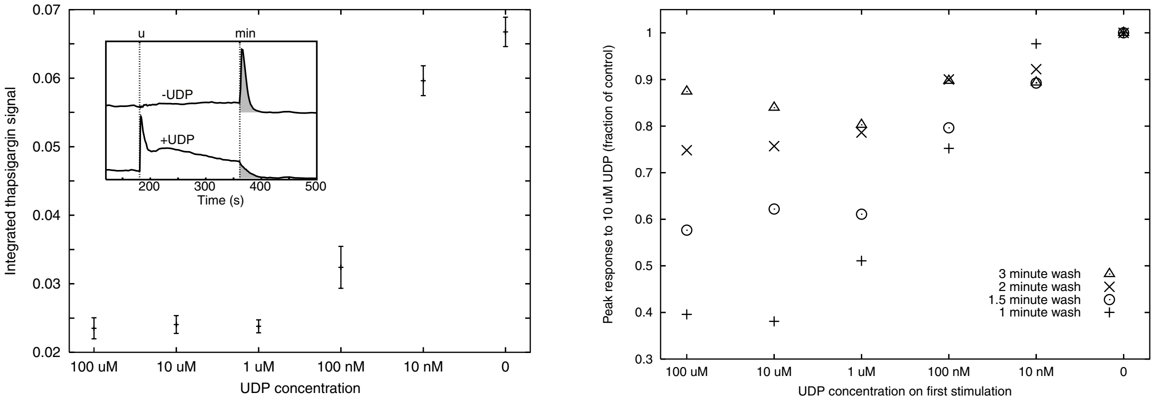

Figure 10.4: Calcium store depletion results from UDP stimulation, and this depletion depresses subsequent calcium responses to UDP. Left panel: quantification of stored calcium. RAW cells were treated with varying concentrations of UDP for 3 min and subsequently treated with the minimum calibration buffer (see text). The calibration buffer-induced calcium transient for each cell was integrated, and the mean and standard errors for those sums are plotted for each UDP pretreatment condition. Inset, averaged time traces for initial stimulations either with or without UDP. Regions of integration used for the main plot are shown shaded. Right panel: store depletion effects on subsequent UDP responses. RAW cells were treated for 2 min with varying concentrations of UDP, washed for the times indicated, and then restimulated with 10 μM UDP. Data are mean±s.e.m.; each point represents data pooled from at least two separate experiments.

the calcium-sensitive dye in the cell resided in the cytoplasm, the residual ER calcium always gave a sharp, transient increase in signal before being removed to the extracellular medium; integrating that signal then provided a relative measure of how much calcium there was in the ER before the calibration process. The results of these measurements are shown in fig. 10.4, left panel. Clearly, cells stimulated with higher concentrations of UDP showed much more store depletion.

The almost complete elimination of stores within 3 min of robust calcium mobilization within the cell is sure to have an effect on subsequent calcium responses to ligand; the right panel of fig. 10.4 shows this. Restimulation after 1 min of wash showed a clear depression of the calcium response that was dependent on the concentration of the initial stimulus. This depression was mostly washed out after 3 min, and was essentially absent after 4 min (see §10.4). These data are in fairly good agreement with published results [42]

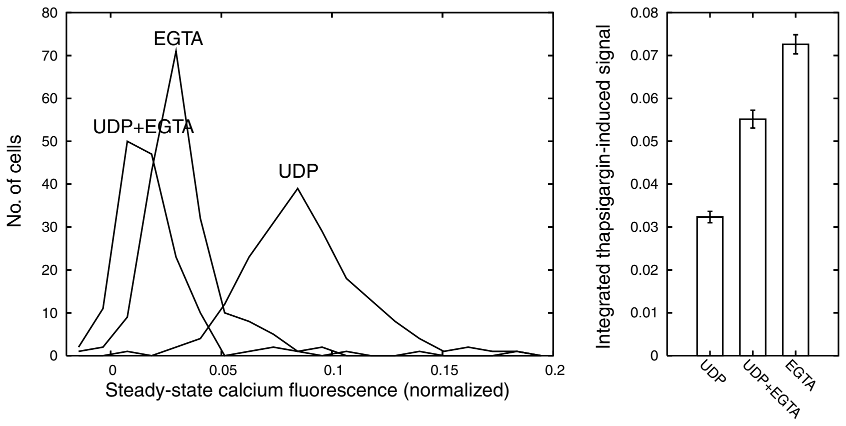

Figure 10.5: Left panel, histogram of steady state cytoplasmic calcium levels in cells after 3 min treatment with 1.5 mM EGTA and 10 μM UDP, either alone or together. Note that full depletion of cytoplasmic calcium requires both UDP and EGTA. Right panel, calcium store levels assessed after the 3 min stimulations. Note that, despite having more calcium in both cytoplasm and extracellular medium, cells treated with UDP alone had the least calcium in their stores.

on calcium store depletion and recovery. The complete washout within so short a time demonstrates that response depression arose from store depletion and not receptor desensitization; receptors to UDP expressed on RAW264.7 cells are not known to desensitize (AfCS, unpublished results).

The ability to perform experiments with different stimulation solutions allowed me to directly compare store depletion effects in the presence and absence of extracellular calcium. As seen in fig. 10.4, left inset, steady-state cytoplasmic calcium levels in cells stimulated with UDP (10 μM) were elevated, and the thapsigargin response indicates that stores were essentially emptied. The high steady-state calcium level was seen again in fig. 10.5, but in the presence of an external chelator during stimulation, UDP depressed calcium levels lower than treatment with chelator alone. Presumably, UDP stimulation led to the activation of some plasma membrane calcium conductance, either through a signaling-related calcium channel or indirectly through the store depletion-triggered calcium release-activated calcium (CRAC) conduction. While CRAC conduction has been reported to be inward-rectifying, that property is not absolute, so CRAC conduction would still be able to allow efflux of calcium when the gradient favors that flow direction.

Interestingly, UDP-induced store depletion was rather weak in the absence of extracellular calcium. This might be because the IP_3 receptor, responsible in this case for ligand-induced calcium release (§6.3), stops conducting at cytoplasmic calcium concentrations significantly below about 300 nM [43]: the cytoplasmic calcium depletion effected by the combination of external chelators and plasma membrane conduction would shut down further release of ER-stored calcium.

Would this low degree of store depletion still be able to activate CRAC conduction? Further experiments, especially those probing depletion and recovery kinetics (analogous to those probing desensitization; see §10.3), will be useful in answering this question. In any case, it is beyond the scope of the discussion here.

10.3 Receptor desensitization

While one can think of many potential places of feedback control in this signaling pathway, the most important one upstream of calcium release appears to be the phosphorylation and subsequent sequestration of the receptors themselves. In this I see a structural similarity with metabolic networks, where product inhibition (used to regulate product concentrations) usually affects the energy-consuming (and hence irreversible) “committed step” entry into the pathway that generates that particular product. This makes sense from a different perspective, too, where the cell can have specificity as to which receptors to downregulate by using the same binding-induced conformational change that initiates the signaling in the first place.

The process, known as desensitization, starts with phosphorylation of activated GPCRs by GPCR kinases (GRKs; see [44]), of which RAW264.7 macrophages express three (Grk 2, 5, and 6). The phosphorylation itself may modulate signaling, and in addition will allow binding of the protein arrestin which further reduces signaling [45]. Arrestin binding also initiates a process whereby bound receptors are endocytosed and then either degraded, or recycled (dephosphorylated and free of arrestin) back to the cell surface [46].

Probing for desensitization, functionally, required stimulation, washout, and a subsequent stimulation; this process, comprising many washes with different solutions, lent itself quite naturally to a microfluidic experimental platform. In addition, the ability to pack six different mini-experiments into each field of view allowed me to perform entire concentration or kinetics series within each data acquisition run where all other conditions were fairly well controlled for (§10.1.1). Indeed, whereas variations in response amplitudes between experiments could sometimes mask desensitization effects, within experiments those were usually quite apparent.

10.3.1 C5a

Fig. 10.6 shows desensitization results for C5a stimulation. Because C5a responses typically returned to baseline within about 30 s after agonist application, even in the continuing presence of agonist, C5a stimulation did not usually result in appreciable store depletion, so desensitization results were cleaner and I could probe for effects without using long washes.

The initial concentration dependences of calcium mobilization and receptor desensitization seem to mirror each other. The C5a response did not appear to saturate at 2.5 μM C5a; in contrast, activation of C5a receptor has been described as having an EC_{50} of about

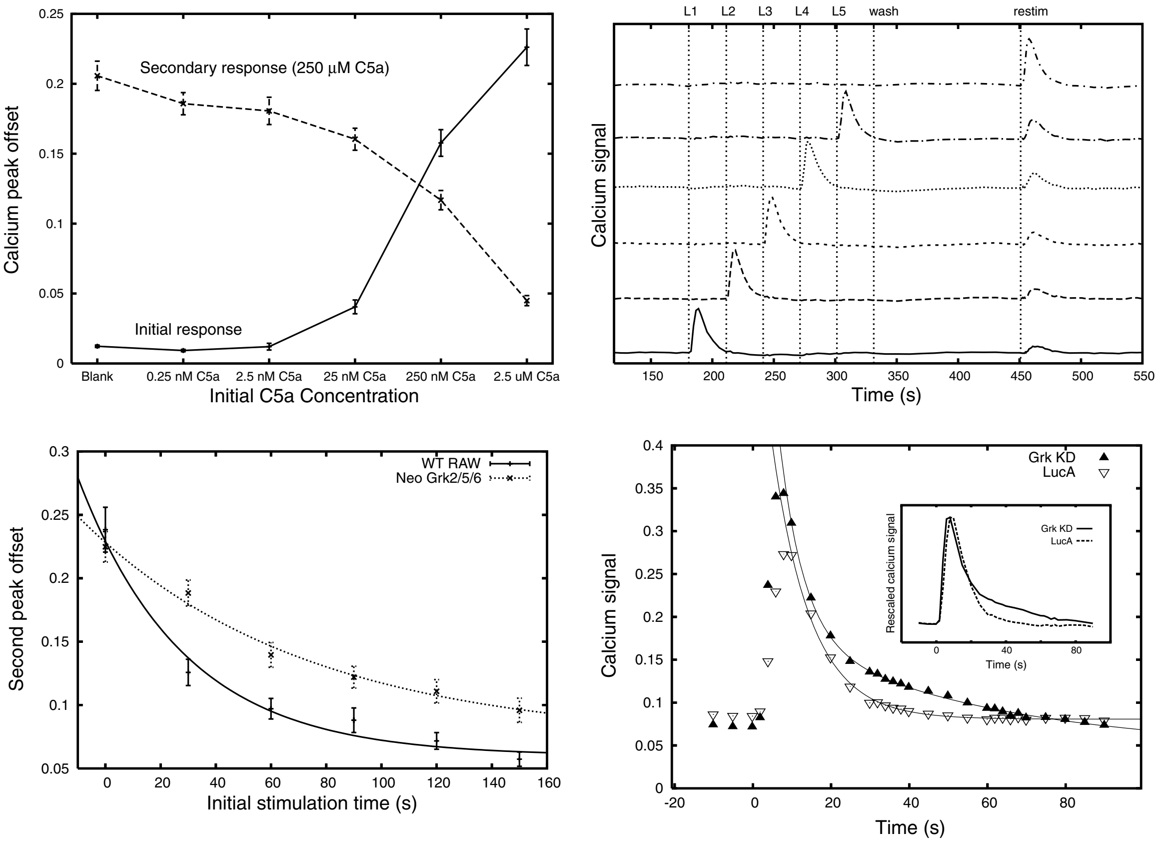

Figure 10.6: Desensitization results for the ligand C5a. Upper left, concentration dependence of C5a desensitization. 2 min initial ligand application, followed by 2 min wash and application of 250 nM C5a for all channels. Upper right, time dependence of C5a desensitization. Each channel (except for the last one) was washed with 250 nM C5a at a different time on the first round, indicated by the vertical dashed lines; the C5a was washed out of all channels at the same time, and the second treatment with C5a was performed at the same time for all channels. Note that channels which were exposed to C5a longer the first time gave lower responses on the second stimulation. Lower left, plot of the second peak offset amplitude as a function of initial C5a exposure time. Note that desensitization is significantly slowed for a cell line expressing shRNA knockdown of Grks 2, 5, and 6. Lower right, comparison of the initial C5a calcium response waveforms for Grk knockdown and control shRNA cell lines. The Grk knockdown waveform has a shoulder that makes it deviate from a single exponential decay; the shoulder is more apparent in the inset, which rescales the two waveforms so that their peaks overlap.

10 nM [47]. Again there appears to be a problem with not enough agonist reaching the cells. It seems rather unlikely for the decreased EC_{50} of C5a observed in the devices to be a result of physiological changes in the cells arising from their experiences inside a microfluidic device; one would expect cell physiology changes to be reflected in response amplitude, not apparent receptor affinity. One could argue that the C5a responses observed in macrofluidic cellular experiments were "clipped" by some saturation effect downstream, giving rise to a lower apparent EC_{50}, but that argument falls apart with the observation that, in the presence of C5aR antagonists that reduced signaling amplitude, the observed affinity for C5a remained unchanged ([47], fig. 2a). Degradation of C5a is known to occur at 37°C, but the extensive pre-flush of ligand solution prior to application to cells should have been enough to clear out degraded C5a. It is entirely possible that the Tygon microbore tubing holding the reservoir of ligand solution outside the device depleted C5a by having it adsorb to the tube walls, or that shear somehow damaged the ligand. The AfCS protocol (§C.1) recommends mixing of C5a solutions by inverting them instead of vortexing, perhaps because of known shear sensitivity.

Regardless, the responses inside microfluidic devices to C5a at 250 nM appear to be well-reproduced, at least within experiments. By flowing on C5a for different amounts of time for each channel, and then restimulating, I was able to build up kinetic data for the desensitization process. Fig. 10.6, upper right panel, shows the experimental time trace for this process. In the first round of stimulations, C5a solution was applied to each channel at a different time, so that the simultaneous washes and restimulations that followed gave rise to different channels exposed to C5a for different amounts of time. Simultaneous restimulations were used because I wanted to avoid problems with time-dependent changes in signaling responsiveness (§10.1.1).

The traces in the upper right panel show clearly that longer initial exposures to 250 nM C5a resulted in lower responses when cells were subsequently restimulated with 250 nM C5a; the timecourse of desensitization onset so obtained is shown in the lower left panel, along with a timecourse obtained with the same protocol but for cells infected with lentivirus expressing shRNA against all three Grk's known to be present in RAW264.7 cells. The triple Grk knockdown clearly displayed slower desensitization onset kinetics, which is expected since lower Grk expression levels should slow down the activation-induced phosphorylation of the C5a receptor that is the initiating event in desensitization.

Interestingly, Grk knockdown also seems to have affected the shape of the C5a-induced calcium response timecourse. Shown in the lower right panel of fig. 10.6 are two comparisons of the single-stimulation recovery kinetics for cells expressing either Grk knockdown or control shRNA (in this case, against luciferase A, which is not present in the RAW264.7 genome). In both cases, calcium responses typically returned to baseline within about 40 s of C5a application, even with the continued presence of the ligand. The kinetics of return to baseline appear to display single exponential decay in the control cell line, with the best-fit line shown in the graph having a decay time of about 10 s. Grk knockdown cells seem to display a ″shoulder″ of residual calcium presence (seen more clearly in the inset graph), and a similar single exponential fit clearly deviated from the recovery data in a systematic way. The best-fit line shown with the Grk recovery data has two components: a fast component with a 6 s decay time, and a slow component with a 50 s decay time. Incidentally, the slow component decay time is of the same order of magnitude as the desensitization onset times seen in the lower left panel of fig. 10.6 (38 s for WT; 81 s for Grk KD).

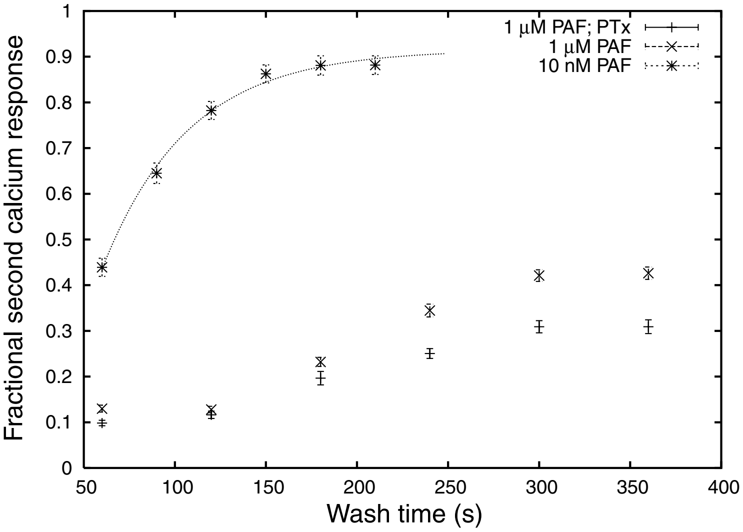

Figure 10.7: Short time scale kinetics of PAF signaling recovery. Cells were stimulated with the indicated concentration of PAF for 60 s, then washed for variable amounts of time before being stimulated with 1 μM PAF. The points plotted represent populational averages and standard errors of the ratio of second to first peak calcium offsets, averaged over all cells that initially responded with a peak calcium offset of at least $\hat{I} - \hat{I}_0 = 0.1$. Pertussis-toxin treated cells were treated for 14 h at 50 ng/ml.

10.3.2 PAF

The story with PAF is more complicated because it usually triggered a sustained release of stored calcium which depleted internal stores. Fig. 10.7 shows the complex recovery kinetics for PAF. Recovery from an initial stimulation at 10 nM displays rather straightforward first-order kinetics; a comparison of the recovery time course for PAF and the data for UDP, shown in fig. 10.4, demonstrates that they occurred with very similar time courses. That these recovery timecourses were independent of the ligand being used suggests a loss of signaling capability that happens downstream of ligand binding and receptor activation. Extrapolating recovery kinetics with the single exponential fit gives a “zero store” time that is 30 s *after* starting the plain buffer wash, i.e., if we believe the first order kinetics, then the store recovery process didn’t start until 30 s into the wash process. This, combined with the fact that the calcium recovery to baseline after ligand washout was a more or less single-exponential process with decay time of 30 s (and this is true for UDP as well), again suggests but does not unequivocally prove that it is calcium store depletion that we are dealing with here, and not any fast process that happens at the receptor level. More experiments need to be performed to verify calcium store depletion with PAF stimulation and correlate that store depletion with loss of signaling.

With a hundredfold higher concentration of initial PAF stimulation, which gave rise to only a small ($\sim$25%) increase in calcium signaling amplitude, the recovery kinetics became totally different. There was a rather small residual response to 1 μM PAF on restimulation, and the responsiveness to PAF did not seem to start recovering within 2 min of wash. Recovery seemed to stop by about 5 min, and by then had only returned to about 40% of the initial level. The apparent absence of desensitization at 10 nM, which appears to be mostly saturating in terms of initial calcium response, suggests the presence of another site of action for PAF on the cell surface, perhaps another binding site on the same receptor or perhaps some site of cross-reactivity on another receptor. Multiple binding affinities for PAF have been reported [48], the weaker one being 500 nM, consistent with the data shown here.

What happened over the 5 min or so during which the desensitized PAF response partially recovers? It is possible that the “desensitization” observed here was simply due to reduced signaling capacity on the part of phosphorylated PAF receptors. In that case, the recovery from desensitization may simply reflect dephosphorylation of those same receptors, with a large fraction of phosphorylated receptors entering the endocytosis path and thereby reducing the pool available for dephosphorylation. Since this implies that receptor endocytosis must compete with recovery of PAF sensitivity, it also assumes that endocytosis occurs on the same time frame of 3-5 min. Translocation studies of GFP-fused C5a receptors support the second assumption (S. Gibson, unpublished results). If this interpretation is correct, then the recovery kinetics of C5a will also require looking into: the kinetic curves of desensitization onset seen in fig. 10.6 may reflect receptor phosphorylation and not internalization, since those secondary responses were probed within 2 min of washout.

Since PAF signals through $G_{\alpha q}$ as well as $G_{\alpha i}$, I wondered what contribution each pathway made to the desensitization process. To test this, I performed the same experiment with cells that have been treated with pertussis toxin (PTx). In mammalian cells PTx eliminates $G_{\alpha i}$ signaling by inducing ADP ribosylation of those subunits which stabilizes their GDP-bound (and hence inactive) state [49, 50], but PTx does not appear to directly influence signaling through $G_{\alpha q}$. PTx intoxication reduced the initial signal amplitude by about 50% (data not shown), but the short wash desensitization fraction remained very similar. PTx-treated cells displayed more desensitization at longer wash times, but given the paucity of data at this point, any conjecture as to why that was would be premature.

Clearly much more data must be collected on PAF store depletion and desensitization, in both wild-type and shRNA-expressing cell lines, before the story is complete.

10.4 Exploring noise in G protein signaling

A look at the single cell data in any experiment quickly reveals large variations in responses from individual cells. This observation immediately poses the question of where the variations come from. The ability to observe individual cells over multiple stimulations in the microfluidic platform provided a convenient way of addressing that question. Again, this ability to observe individual cells and not just populational averages makes all the difference.

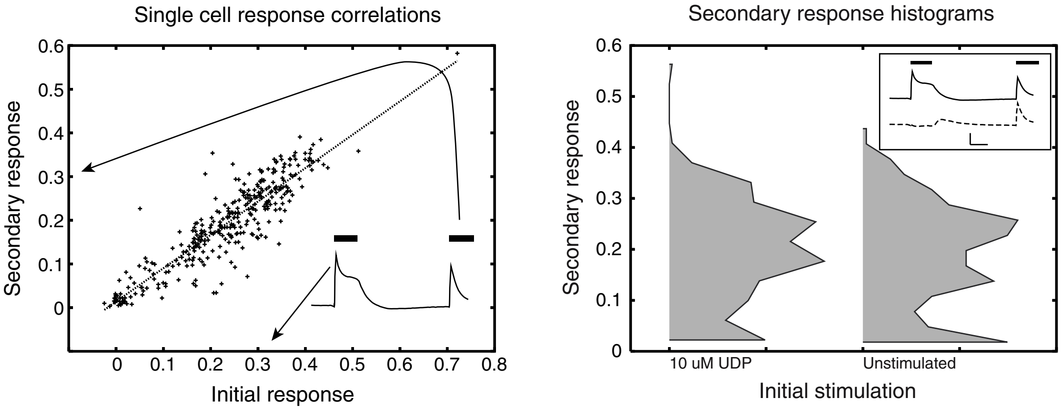

Figure 10.8: Single cell correlations from repeated UDP stimulation. Cells were stimulated by two rounds of 60 s each of 10 μM UDP, separated by 4 min of base buffer wash. Left panel shows the scatter plot of first response against second response, along with a linear fit; each point here represents a different cell, where its x coordinate shows the cell's response to the first stimulation and its y coordinate the cell's response to the second stimulation. To make sure no desensitization or depletion effects were present, three of six channels in this experiment were not stimulated with UDP on the first round, so that their responses on the second round could be compared with those channels that were. The right panel shows that the two populations gave essentially identical response histograms and rules out possible problems associated with desensitization or store depletion. Right panel inset shows averaged response time traces. Upper thick bars denote times of UDP application. Lower scale bars: 50 s (horizontal); 0.1 adjusted fluorescence (vertical).

In restimulation experiments with all three ligands (UDP, PAF, and C5a), cells over a broad range of responsivenesses reproduced their original response amplitudes (fig. 10.8 and table 10.1). In particular, a population of consistent non-responders usually showed up as a cluster of cells centered near the origin in response correlation plots, as in the left panel of fig. 10.8, and few of the responding cells strayed very far from the best-fit lines.

Reproducibility could be quantified in two different ways. We could take the two response amplitudes for any given cell as two different random variables x and y, and compute their normalized correlation:

$$\begin{aligned} c_{xy} &= \left\langle \left(\frac{x-\bar{x}}{\sigma_x}\right)\left(\frac{y-\bar{y}}{\sigma_y}\right)\right\rangle \\ &= \frac{\langle xy\rangle - \langle x\rangle \langle y\rangle}{\sigma_x \sigma_y}, \end{aligned} \tag{10.1}$$

where σ_x and σ_y are the standard deviations of x and y, respectively. This quantity is also the correlation coefficient r from linear regression. On the other hand, since x and y are repeated observations of the same process, we could consider extrinsic and intrinsic contributions to their variability [7, 51]:

$$\begin{aligned} \eta^2_{\text{int}} &\equiv \frac{\left\langle (x-y)^2 \right\rangle}{2\left\langle x \right\rangle \left\langle y \right\rangle} && (10.2) \\ \eta^2_{\text{ext}} &\equiv \frac{\left\langle xy \right\rangle - \left\langle x \right\rangle \left\langle y \right\rangle}{\left\langle x \right\rangle \left\langle y \right\rangle}, && (10.3) \end{aligned}$$

where intrinsic variability encompasses effects of stochasticity arising during the signal transmission process as a result of having low copy numbers of signaling intermediates, and extrinsic variability encompasses variability in the cell state that gets reproduced over different stimulations. The similarity between the extrinsic noise expression and the correlation coefficient arises from the fact that extrinsic noise gives rise to correlated responses. In the case of my repeated stimulation experiments, the intrinsic noise expression had to be changed, since the first and secondary responses did not necessarily have the same magnitude, even on average. This variability was hinted at above (§10.1.1), but showed up in full force here: note that in fig. 10.8 the slope of the best-fit line is not unity (see also table 10.1). Since the data in fig. 10.8 did fit so well to a straight line, I could assume that the global drop in responsiveness simply applied a scaling factor to the observed calcium response and thus correct for it by rescaling x and y with their average values:

$$\eta^2_{\text{int}} \equiv \frac{1}{2}\left\langle \left(\frac{x}{\left\langle x \right\rangle} - \frac{y}{\left\langle y \right\rangle} \right)^2 \right\rangle. \tag{10.4}$$

This reduces to eq. 10.2 when $\langle x \rangle = \langle y \rangle$; applying the same transformation has no effect on eq. 10.3.

Table 10.1: Single cell response correlation slopes, correlation coefficients, and noise contributions from intrinsic and extrinsic sources. UDP was used at 10 μM, C5a at 250 nM, and PAF at 10 nM (except for the last line). In all cases, scatter plots were generated, as in the left panel of fig. 10.8, with the initial response amplitude on the horizontal axis and the second response amplitude on the vertical. Linear regression of the data gave the slope and correlation coefficient r^2 shown. Intrinsic noise coefficient η^2_{int} is the responsiveness-corrected value given in eq. 10.4. Intrinsic/extrinsic noise amplitudes were not computed for differential stimulations, since there they have no meaning. n denotes the number of cells in each sample.

1st stim	2nd stim	Slope	r^2	η^2_{int}	η^2_{ext}	n
UDP	UDP	0.823±0.022	0.813	0.023	0.205	323
C5a	C5a	0.714±0.020	0.871	0.043	0.583	206
PAF	PAF	0.617±0.028	0.795	0.021	0.137	127
UDP	C5a	0.206±0.063	0.025	-	-	409
C5a	UDP	0.306±0.025	0.176	-	-	658
UDP	PAF (100 nM)	0.586±0.048	0.353	-	-	279

As shown in table 10.1, the squared correlation coefficient (r^2 from linear regression), a measure of what fraction of the variation in the second response is connected to variations in the first, could approach 90% for restimulation with the same ligand. Further, both C5a and PAF responses maintained good reproducibility in the face of about 30-40% desensitization (§10.3). The intrinsic and extrinsic noise coefficients indicate that most ($\gtrsim$80%) of the signal noise comes from extrinsic sources. They also give a good indication as to how much variability there was in the individual responses: cellular responses to C5a appear to be by far the most variable among the three ligands tested.

Correlating responses on a cell-by-cell basis with different ligands proves a lot more interesting. UDP and PAF show a fair amount of correlation with each other. UDP and C5a, on the other hand, display little correlation. This probably relates to the fact that C5a triggers calcium release via $\text{G}_{\beta}\gamma$, whereas UDP does so via $\text{G}_{\alpha q}$; PAF triggers calcium release via both. The UDP-C5a correlational data also shed some light on the nature of the non-responding populations that appear to be present with most ligand stimulations. As shown in fig. 10.9, the non-responders to C5a actually display responsivenesses to UDP

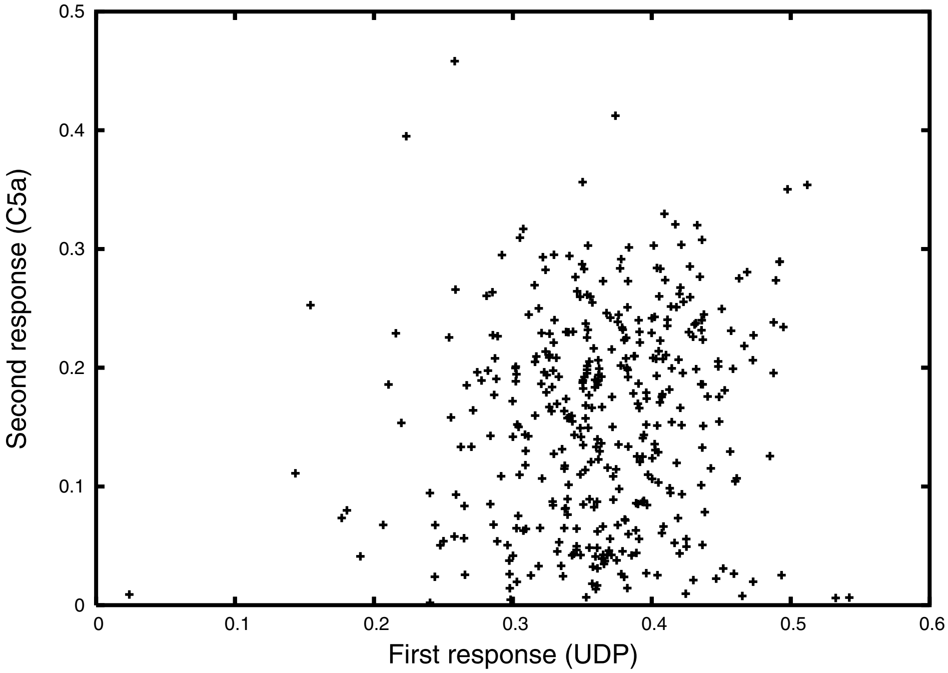

Figure 10.9: Single cell correlations for UDP and C5a responses. Cells were stimulated first with 10 μM UDP, and then with 250 nM C5a. Sufficient washout time was used to ensure full recovery of calcium stores before the C5a stimulation.

that appear no different from the population at large. This immediately rules out any sort of general mechanism which produces non-responding cells, for instance any sort of cell cycle-dependent signal transmission variations.

The above data provide a tantalizing glimpse of the complexities of signal transduction at the level of single cells: different cells within the same population somehow have different inherent sensitivities to different ligands. Sensitivities appear to be biased by the particular G protein pathway involved, and to any given ligand there are significant (though not always overlapping) populations of cells which do not respond.

Chapter 11

Discussion

11.1 Achievements and prospects

The biological stories here are still incomplete, but the data clearly indicate that the experimental platform works has generated interesting new data.

In the quantitative analysis of many biochemical networks, a major impediment has the lack of reliable *in vivo* rate constants for the reactions so neatly displayed on network diagrams. Computer simulations can be used in limited cases to infer these rate constants, but so many of them are unknown that the fitting problem tends to be completely underdetermined by the available data. The experiments observing desensitization within microfluidic devices provide kinetic measurements of several different processes involved, including short-term calcium depletion and longer-term phosphorylation. The data from C5a stimulation also suggest that receptor phosphorylation may also subtly alter the calcium response waveform, implicating phosphorylation in the shut-off of calcium signaling. That C5aR desensitizes rapidly may be the reason why cellular calcium returns to baseline after extended C5a stimulation but not UDP stimulation, and by extension why UDP induces calcium store depletion, whereas C5a does not. The story with PAF is a lot more complicated, with multiple different processes contributing to depressed sensitivity after an initial stimulus, but that is where the benefits of having the microfluidic device can shine through more clearly. Just as in NMR, where different imaging modalities can be obtained simply by changing around EM pulse protocols, I can look at different kinetic processes by changing around perfusion protocols in the microfluidic devices. The turnaround time for looking at different processes becomes very quick, especially since the assay itself is not dependent on any genetically encoded protein modification. At the same time, incorporating modified cell lines with certain proteins knocked out will be essential to determining what processes are being observed for any given experiment.

The single cell correlation data provide another view of the signaling process. On the single cell level, there is a remarkable amount of variability in responsiveness to ligand that is at once very reproducible between identical stimuli and fairly uncorrelated between different ligands. Thus the major contributor to response variability is expected to be quite far upstream in signaling, certainly upstream of where the response pathways for different receptors merge; variability may be at the level of receptor expression itself.

Again, the data are still far from complete, but some intriguing and compelling possibilities have presented themselves that will require further exploration. There appears to be some limited correlation between PAF and UDP, whereas the correlation between UDP and C5a is much lower. Since UDP and PAF share the ability to signal through G_q, whereas C5a only signals through G_i, this points to coupling variability that, at least partially, comes downstream of G protein activation. Recent work simultaneously measuring G protein dissociation and calcium influx (S. Gibson, unpublished results) has indicated that G protein dissociation in response to C5a stimulation appears much more robust than calcium release, supporting the idea that it is coupling between the two that varies between cells. Probing for single-cell correlations, in conjunction with measurements of upstream activation using protein reporters, promises to be a powerful method for understanding noise and variation in signal transduction processes.

The novel microfluidic platform, then, provides not only higher data quality and throughput but also novel experimental modalities that have hitherto been unavailable for cell signaling experiments. These improvements promise to provide more detailed and reliable information that is critically needed for achieving a quantitative understanding of cellular processes.

11.2 Future work

11.2.1 Throughput

One of the things that has been limiting the observation area has been the rapid falloff of numerical aperture, and consequently light collection efficiency, that happens with lower magnification. Recent microscopes with larger tube sizes can give better collection efficiency, lower magnification, or both. This, along with newer low-noise, large-format CCD cameras, should increase the number of cells observable by at least fourfold — either raising the number of experiments in one acquisition run or raising the number of cells per experiment in order to get better statistics.

Another possibility for increasing throughput is to scan the observation area with a motorized stage. This sacrifices time resolution for observation area, but since frames are seldom taken in rapid succession, the clever use of time staggering may realize significant throughput enhancements without necessarily reducing time resolution or sacrificing experimental consistency.

11.2.2 Sensors and modalities

I designed and built the devices with versatility in mind, and calcium assays are just the start of what I should be able to do with them. Work is currently ongoing to observe translocation of GFP fusion proteins. Preliminary data show clear translocation of the p65 subunit of NF-κB into the nucleus of macrophages upon stimulation with lipopolysaccharide. Direct imaging of protein translocation must be performed at higher resolutions and therefore reduced fields. p65 translocation experiments are currently imaged at 40×, giving access to parts of two channels at a time. Again, use of a motorized stage will improve data throughput, though at higher magnifications the depth of focus is much reduced, so the motorized stage must be used in conjunction with some sort of autofocus mechanism.

Because the PDMS layer underneath cells behaves very much like glass optically, most standard imaging techniques available for imaging through standard cover slips, such as epifluorescence confocal and through-the-objective TIRF microscopy, should be possible in the microfluidic devices as well. In addition, different imaging modes such as FRET, FRAP, and FLIM, among others, can be used to access different properties within cells. FRET in particular should be explored because so many molecular biosensors are based on fluorescence energy transfer.

11.2.3 Cells

The microfluidic platform has been demonstrated mostly with RAW 264.7 macrophages, with some experiments done on bone marrow-derived macrophages (BMDMs). Thus both transformed cell lines and primary cells can be seeded and cultured inside devices. Among transformed cell lines, RAW macrophages are actually rather difficult to grow in microfluidic devices; on-chip culturing has been demonstrated, in different platforms, for many other cell types. My flow-based seeding scheme should be applicable to just about any cell that can bind to and grow on top of extracellular matrix components such as fibronectin.

Bibliography

[1] M. H. V. van Regenmortel. Reductionism and complexity in molecular biology. *EMBO Rep.*, 5(11):1016–20, 2004.

[2] K. Strange. The end of "naive reductionism": rise of systems biology or renaissance of physiology? *Am. J. Physiol. Cell Physiol.*, 288:C968–C974, 2005.

[3] M. B. Elowitz and S. Leibler. A synthetic oscillatory network of transcriptional regulators. *Nature*, 403(6767):335–338, Jan. 2000.

[4] M. Acar, A. Becskei, and A. van Oudenaarden. Enhancement of cellular memory by reducing stochastic transitions. *Nature*, 435(7039):228–232, May 2005.

[5] M. Natarajan, K.-M. Lin, R. C. Hsueh, P. C. Sternweis, and R. Ranganathan. A global analysis of cross-talk in a mammalian cellular signalling network. *Nat. Cell Biol.*, 8(6):571–580, June 2006.

[6] B. Huang, H. Wu, D. Bhaya, A. Grossman, S. Granier, B. K. Kobila, and R. N. Zare. Counting low-copy number proteins in a single cell. *Science*, 315(5808):81–84, Jan. 2007.

[7] M. B. Elowitz, A. J. Levine, E. D. Siggia, and P. S. Swain. Stochastic gene expression in a single cell. *Science*, 297(5584):1183–1186, Aug. 2002.

[8] J. E. Ferrell, Jr., and E. M. Machleder. The biochemical basis of an all-or-none cell fate switch in *Xenopus* oocytes. *Science*, 280(5365):895–898, May 1998.

[9] C. L. Hansen, E. Skordalakes, J. M. Berger, and S. R. Quake. A robust and scalable microfluidic metering method that allows protein crystal growth by free interface diffusion. *Proc. Natl. Acad. Sci. USA*, 99:16531–6, 2002.

[10] Y. Xia and G. M. Whitesides. Soft lithography. *Angew. Chem. Int. Edit.*, 37(5):550–575, 1998.

[11] M. A. Unger, H. P. Chou, T. Thorsen, A. Scherer, and S. R. Quake. Monolithic microfabricated valves and pumps by multilayer soft lithography. *Science*, 288:113–116, 2000.

[12] G. M. Whitesides. The origin and future of microfluidics. *Nature*, 442(7101):368–73, 2006.

[13] M. J. Berridge, P. Lipp, and M. Bootman. The versatility and universality of calcium signalling. *Nat. Rev. Mol. Cell. Biol.*, 1(1):11–21, 2001.

[14] B. Alberts, D. Bray, J. Lewis, M. Raff, K. Roberts, and J. D. Watson. *Molecular biology of the cell*. Garland Press, New York, NY, 3rd ed., 1994.

[15] M. J. Berridge, M. D. Bootman, and H. L. Roderick. Calcium signalling: dynamics, homeostasis and remodelling. *Nat. Rev. Mol. Cell. Biol.*, 4(7):517–529, 2003.

[16] I. von Kügelgen and A. Wetter. Molecular pharmacology of P2Y-receptors. *Naunyn-Schmiedeberg's Arch. Pharmacol.*, 362:310–323, 2000.

[17] Participating investigators and scientists of the Alliance for Cellular Signaling. Overview of the alliance for cellular signaling. *Nature*, 420:703–706, Dec. 2002.

[18] V. Studer, G. Hang, A. Pandolfi, M. Ortiz, W. F. Anderson, and S. R. Quake. Scaling properties of a low-actuation pressure microfluidic valve. *J. Appl. Phys.*, 95(1):393–8, 2004.

[19] I. Fraser, D. Hughes, and S. Gordon. Divalent cation-independent macrophage adhesion inhibited by monoclonal antibody to murine scavenger receptor. *Nature*, 364(6435):343–6, 1993.

[20] E. K. Kartakov and S. R. Quake. Polyelectrolyte surface interface for single-molecule fluorescence studies of DNA polymerase. *Biotechniques*, 34(3):505–510, Mar. 2003.

[21] E. K. Kartakov and S. R. Quake. Microfluidic device reads up to four consecutive base pairs in DNA sequencing-by-synthesis. *Nucleic Acids Res.*, 32(9):2873–2879, 2004.

[22] J. E. Mark, ed. *Polymer data handbook*. Oxford University Press, New York, 1999.

[23] J. F. Shackelford and W. Alexander, eds. *CRC materials science and engineering handbook*. CRC Press, Boca Raton, FL, 3rd ed., 2001.

[24] M. Chachisvilis, Y.-L. Zhang, and J. A. Frangos. G protein-coupled receptors sense fluid shear stress in endothelial cells. *Proc. Natl. Acad. Sci. USA*, 103(42):15463–15468, Oct. 2006.

[25] S. K. Hughes, B. K. Wacker, M. M. Kaneda, and D. L. Elbert. Fluid shear stress modulates cell migration induced by sphingosine 1-phosphate and vascular endothelial growth factor. *Ann. Biomed. Eng.*, 33(8):1003–1014, Aug. 2005.

[26] K. Kosaki, J. Ando, R. Korenaga, T. Kurokawa, and A. Kamiya. Fluidic shear stress increases the production of granulocyte-macrophage colony-stimulating factor by endothelial cells via mRNA stabilization. *Circ. Res.*, 82:794–802, 1998.

[27] K. Svoboda and S. M. Block. Force and velocity measured for single kinesin molecules. *Cell*, 77(5):773–84, June 1994.

[28] M. B. Miller and B. L. Bassler. Quorum sensing in bacteria. *Annu. Rev. Microbiol.*, 55:165–199, 2001.

[29] G. Helmlinger, R. V. Geiger, S. Schreck, and R. M. Nerem. Effects of pulsatile flow on cultured vascular endothelial cell morphology. *J. Biomech. Eng.*, 113(2):123–131, May 1991.

[30] C. L. Hansen, M. O. A. Sommer, and S. R. Quake. Systematic investigation of protein phase behavior with a microfluidic formulator. *Proc. Natl. Acad. Sci. USA*, 101(40):14431–6, 2004.

[31] L. D. Landau and E. M. Lifshitz. *Fluid Mechanics*. Butterworth and Heinemann, Oxford, 1987.

[32] B. Huang, H. Wu, S. Kim, and R. N. Zare. Coating of poly(dimethylsiloxane) with *n*-dodecyl-$beta$-D-maltoside to minimize nonspecific protein adsorption. *Lab Chip*, 5(10):1005–1007, Oct. 2005.

[33] M. W. Toepke and D. J. Beebe. PDMS absorption of small molecules and consequences in microfluidic applications. *Lab Chip*, 6(12):1484–1486, Dec. 2006.

[34] K. R. Gee, K. A. Brown, W.-N. U. Chen, J. Bishop-Stewart, D. Gray, and I. Johnson. Chemical and physiological characterization of fluo-4 ca^{2+}-indicator dyes. *Cell Calcium*, 27(2):97–106, Feb. 2000.

[35] M. L. Woodruff, A. P. Sampath, H. R. Matthews, N. K. Krasnoperova, J. Lem, and G. L. Faim. Measurement of cytoplasmic calcium concentration in the rods of wild-type and transducin knock-out mice. *J. Physiol.*, 542(3):843–854, 2002.

[36] S. L. Zhang, Y. Yu, J. Roos, J. A. Kozak, T. J. Deerinck, M. H. Ellisman, K. A. Stauderman, and M. D. Cahalan. Stim1 is a Ca^{2+} sensor that activates CRAC channels and migrates from the Ca^{2+} store to the plasma membrane. *Nature*, 437(7060):902–5, Oct. 2005.

[37] A. V. Yeromin, S. L. Zhang, W. Jiang, Y. Yu, O. Safrina, and M. D. Cahalan. Molecular identification of the CRAC channel by altered ion selectivity in a mutant of Orai. *Nature*, 443(7108):226–9, 2006.

[38] M. Prakriya, S. Feske, Y. Gwack, S. Srikanth, A. Rao, and P. G. Hogan. Orai1 is an essential pore subunit of the CRAC channel. *Nature*, 443(7108):230–3, 2006.

[39] J. T. Smyth, W. I. DeHaven, B. F. Jones, J. C. Mercer, M. Trebak, G. Vazquez, and J. W. Putney, Jr. Emerging perspectives in store-operated Ca^{2+} entry: Roles of Orai, Stim and TRP. *Biochim. Biophys. Acta*, 1763(11):1147–1160, 2006.

[40] J. Soboloff, M. A. Spassova, M. A. Dziadek, and D. L. Gill. Calcium signals mediated by STIM and Orai proteins — a new paradigm in inter-organelle communication. *Biochim. Biophys. Acta*, 1763(11):1161–1168, 2006.

[41] M. Treiman, C. Caspersen, and S. B. Christensen. A tool coming of age: thapsigargin as an inhibitor of sarco-endoplasmic reticulum Ca^{2+}-ATPases. *Trends Pharmacol. Sci.*, 19(4):131–5, Apr. 1998.

[42] M. Montero, J. Alvarez, and J. García-Sancho. Control of plasma-membrane Ca^{2+} entry by intracellular Ca^{2+} stores. Kinetic evidence for a short-lived mediator. *Biochem. J.*, 288:519–525, 1992.

[43] C. W. Taylor and A. J. Laude. IP_3 receptors and their regulation by calmodulin and cytosolic Ca^{2+}. *Cell Calcium*, 32(5–6):321–334, 2002.

[44] J. A. Pitcher, N. J. Freedman, and R. J. Lefkowitz. G protein-coupled receptor kinases. *Annu. Rev. Biochem.*, 67:653–92, 1998.

[45] T. A. Kohout and R. J. Lefkowitz. Regulation of G protein-coupled receptor kinases and arrestins during receptor desensitization. *Mol. Pharmacol.*, 63(1):9–18, 2003.

[46] J. A. Koenig and J. M. Edwardson. Endocytosis and recycling of G protein-coupled receptors. *Trends Pharmacol. Sci.*, 18:276–287, 1997.

[47] D. R. March, L. M. Proctor, M. J. Stoermer, R. Sbaglia, G. Abbenante, R. C. Reid, T. M. Woodruff, K. Wadi, N. Paczkowski, J. D. A. Tyndall, S. M. Taylor, and D. P. Fairlie. Potent cyclic antagonists of the complement C5a receptor on human polymorphonuclear leukocytes. Relationships between structures and activity. *Mol. Pharmacol.*, 65:868–879, 2004.

[48] J. T. O'Flaherty, J. R. Surles, J. Redman, D. Jacobsen, C. Piantadosi, and R. L. Wykle. Binding and metabolism of platelet-activating factor by human neutrophils. *J. Clin. Invest.*, 78(2):381–388, Aug. 1986.

[49] L. Stryer. *Biochemistry*. W. H. Freeman and Company, New York, 1995.

[50] G. M. Bokoch, T. Katada, J. K. Northup, E. L. Hewlett, and A. G. Gilman. Identification of the predominant substrate for ADP-ribosylation by islet activating protein. *J. Biol. Chem.*, 258(4):2072–2075, Feb. 1983.

[51] P. S. Swain, M. B. Elowitz, and E. D. Siggia. Intrinsic and extrinsic contributions to stochasticity in gene expression. *Proc. Natl. Acad. Sci. USA*, 99(20):12795–12800, Oct. 2002.

Part III

Miscellaneous fluidics

Chapter 12

Amplifying valves

The ability to gate flow using pressure in a microfluidic device, as with soft valves, means that we can start thinking about doing logical operations inside microfluidic devices.

There are many reasons why this would be useful. As the number of valves per device increases, the number of control lines required for their independent actuation starts to become unmanageable. Thus, most large-scale microfluidic integration projects use large numbers of repeated units, with a limited set of control lines that controls all of them simultaneously. The use of multiplexers [1] reduces, but does not eliminate this requirement, and indeed only works when small portions of the device (e.g., single chambers or rows of chambers) are active at a time. If some of the control logic could be off-loaded to the fluidics, then, there is potential to greatly reduce the "bus width" of the computer-to-device interface. For instance, assuming that signals can propagate fast enough, the valve state of an entire device can be input serially. In this case a small number of control line inputs can, at some speed penalty, control an unlimited number of independently actuated valves.

Microfluidic devices may also be useful in settings other than the laboratory. Devices that incorporate digital fluidic logic may give richer and more robust functionality as implants and would require only a single power source. Such devices could also be used in circumstances where, because of interference, electronic control systems would be unreliable; the most extreme example of this would be devices designed to withstand the electromagnetic pulse associated with thermonuclear detonation.

One challenge that has impeded the implementation of logic in low Reynolds number microfluidic devices has been the lack of generally cascadable gates. That is, the output of any gate must be able to drive the input of another gate running at the same pressure. This has been challenging because microfluidic valves typically do not exhibit gain: they use a the presence of a high pressure to gate flow being driven at a lower pressure. Each step of a logic cascade, then, must entail a steady lowering of the pressures used to transmit signals.

To make a cascadable gate, then, one must have an amplifying valve, which we can think of as a fluidic transistor. It must be able to impede flow driven at a high pressure by using an input signal at a lower pressure. While this has been accomplished before [2], the implementation has involved many fabrication steps and was in general rather difficult.

12.1 The design

As in Mark Adams' work [2], my design involves using a "piston" to concentrate force from one surface onto another. The difference is that here the force-concentrating piston is built out of PDMS rather than some harder substance (fig. 12.1), so that no photolithography need be done with the devices after generating the molds; this makes the fabrication process much simpler and more reliable.

Another way of thinking about the actuation is as follows: if we pressurize the control layer, it will press down on and deform the tops of the cushion channel. A lot of that load will be borne by the central pillar, which means that the cushion layer transfers some of

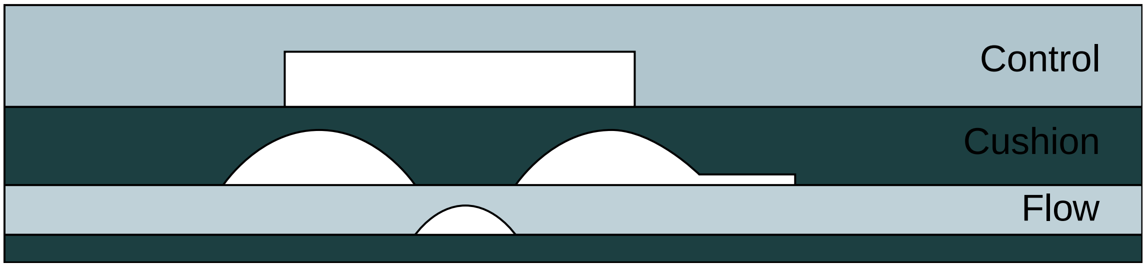

Figure 12.1: Basic idea behind simple amplifying valve. This is a cross-section through the device, which is circular; the planar layout is seen in fig. 12.2. The intervening cushion layer between the control and flow layers serves to concentrate the force from a large area in the control layer onto a smaller area in the flow layer. In this way, the force balance should allow us to gate a stream in the flow layer with a lower pressure signal in the control layer.

the force from the periphery onto the central pillar. This in essence concentrates more force onto the gated channel in the bottom flow layer.

Several things to note about this design:

- The central cushion layer, as shown, is rounded. This is to ease lift-off of the cushion layer from the mold, and to improve the coupling between pressure above the cushion layer and the central pillar which pushes against the flow layer.
- Alignment errors can be quite problematic here: a mis-aimed central pillar will dissipate most of the actuation force onto the bulk PDMS instead of the flow channel.
- Because the valve is gated by force, and not by flow, its analog in electronics is the field-effect transistor (FET). Normal operation of this valve is analogous to the "depletion" mode of electronic FETs [3].
- Instead of venting the cushion layer, we can also apply pressure to it. Pressure here *opens* the valve instead of closing it, as pressure in the cushion layer takes the pressure load in the control layer. This is in direct analogy to the FET's "enhancement" mode.
- The input impedance in both transistor operating modes is quite large: the gating

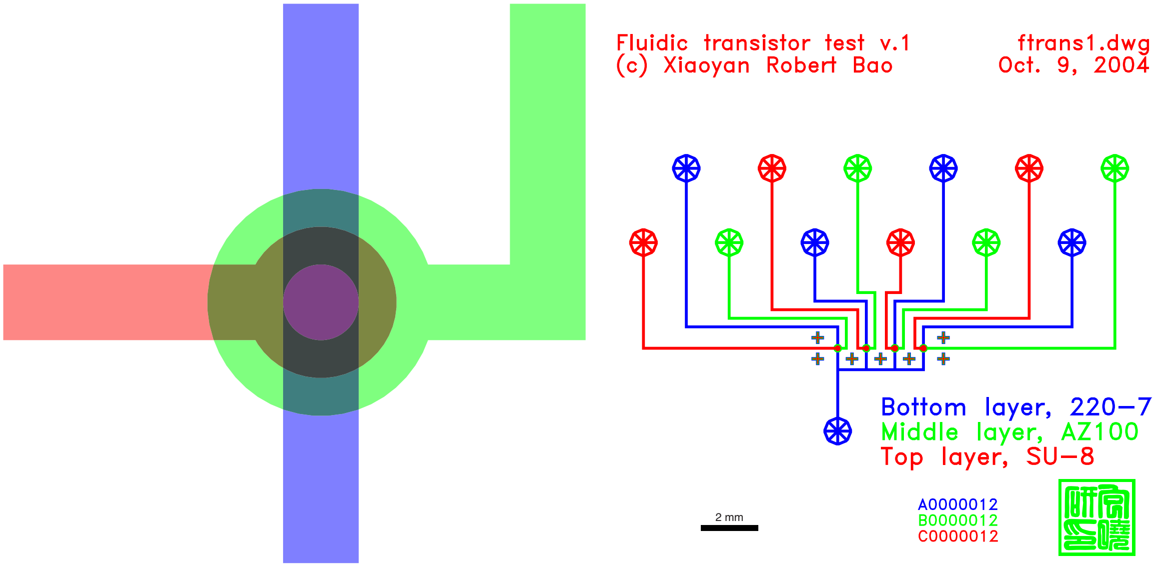

Figure 12.2: Top view of fluidic transistor as fabricated. Control layer in red, flow layer in blue, with intervening cushion layer in green. Left, magnified layout of the transistor itself. Right, layout of the entire test device. Scale bar in black

pressures are always separated from other layers by a layer of PDMS, so the fluid flux from gating valves to the rest of the device arises from molecular diffusion and is rather minimal.

12.2 Device performance and future work

The first-round implementation of the device used fairly standard channel geometries; the layout is shown in fig. 12.2. Amplification was displayed with the devices fabricated as described in Appendix B.3. Fig. 12.3 shows the valves opening and closing when both control and flow lines were drive at 10 psi. Further testing indicated that the valve could gate 13 psi flow with 10 psi in the control layer.

I've also demonstrated gating via pressurization of the cushion layer, i.e., "enhancement" mode for the fluidic FET, albeit with a batch of devices fabricated with a slightly different protocol. In these devices, actuation of the cushion layer at 7 psi was sufficient to

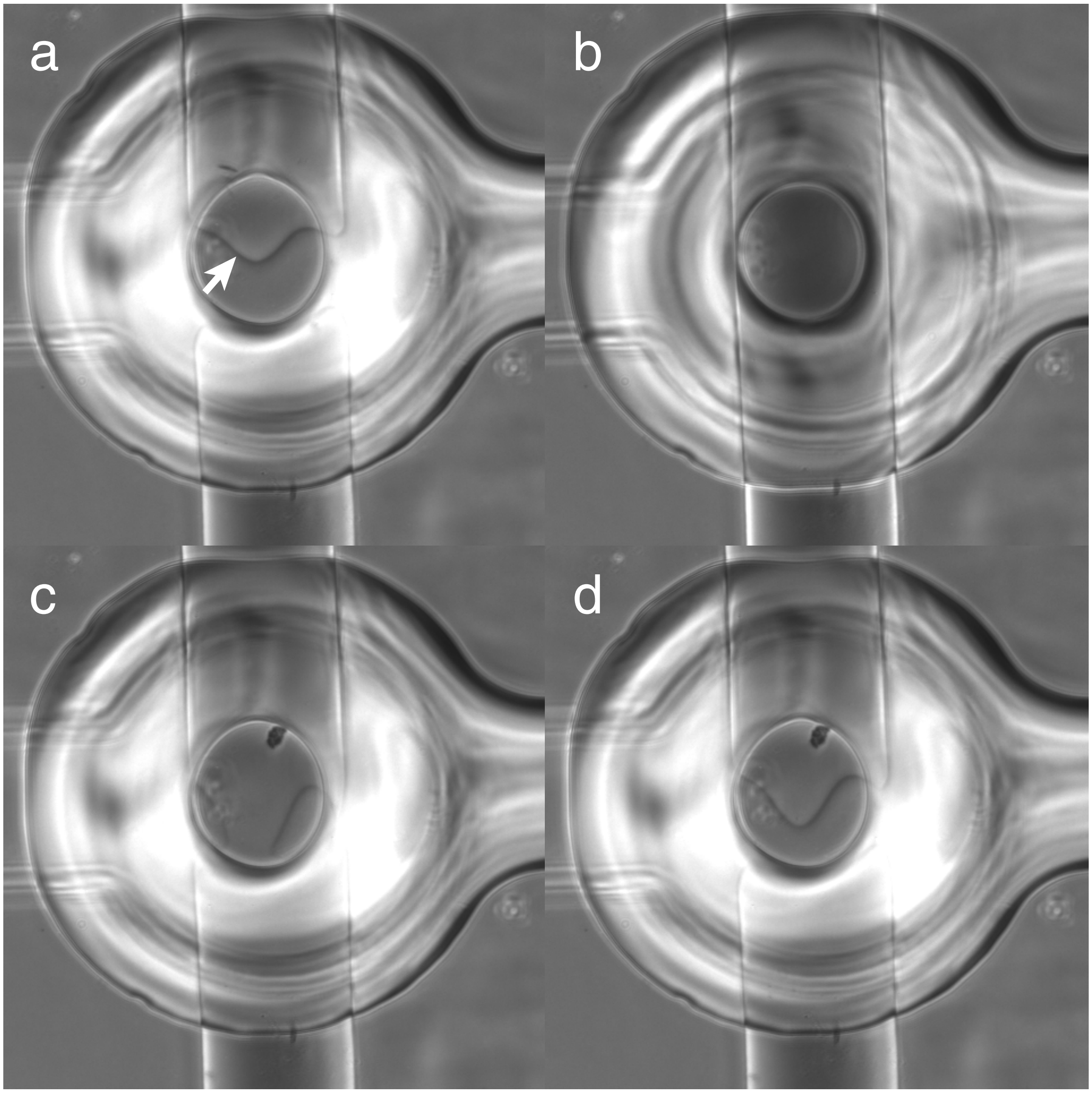

Figure 12.3: Phase contrast images of amplifying valve actuation. Valve layout and orientation are as in fig. 12.2 (left side). Both control and flow layers were driven at 10 psi. (a) initially, with the valve actuated and flow being driven from the top, the valve remains closed, as indicated by the presence of a meniscus indicating the boundary of where the PDMS has sealed against itself (white arrow). (b) Upon release of control layer pressure, the valve opens. (c) Application of pressure at the valve starts the closing process; in this frame there is some contact between channel floor and ceiling but the channel appears still to be open. (d) a fraction of a second later the valve has closed completely.

open the valve closed by application of 25 psi at both control and flow layers.

Having available both modes of switching for fluidic logic circuits would be quite useful, in the same way that complementary pairs of enhancement and depletion MOSFETs lay the foundation for CMOS electronics: with the transistors arranged in push-pull pairs, we can get low output impedance (and hence noise-immunity, as well as switching speed) as well as low quiescent current dissipation [3]. In fact, since the fluidic FET inputs have very large impedances, significant fluid flow rates only occur during transient periods of valve state changes.

Unfortunately, the use of fluidic FETs in push-pull pairs requires a property of the enhancement valve that I haven't yet achieved. Specifically, the enhancement valve, when opened, needs to be able to drain away a lot of pressure, just as the "pull" transistor in a TTL pair is able to drain the voltage at its base to within a diode drop (0.6 V) of ground. This has proven rather difficult to achieve, because of the way the valve is set up: since there is only a thin layer of PDMS separating the cushion layer from the flow layer, the valve cushion itself can act as a gating valve at a high enough pressure difference. Initially, when the flow channel is under high pressure, the enhancement valve works as designed. However, in a push-pull pair used as an inverter, the enhancement valve must be able to pull the output line's pressure down low enough that it can't actuate downstream valves. That means that the valve has to remain open as the pressure difference between cushion layer and flow layer rises; in the few times that I've tried this, the valve doesn't stay open long enough for the pressure to bleed out of the flow layer input far enough.

I must add that I haven't devoted much time to this idea, and that I'm confident the technical problems can be solved with a little effort. In addition, I think that lots of design parameters can be optimized *in silico* with the use of finite element modeling [4]. Combining these amplifying valves with the fabrication of vias in devices should allow us to make fully fluidic analogs of CMOS electronics and greatly enhance the intelligence of soft valve microfluidic devices.

Chapter 13

Virtual walls for very high chamber density

One of the greatest touted benefits of using microfluidic devices is the high degree of integration possible. This allows, for instance, many copies of a basic design to be incorporated into a single device, thus allowing for massive parallelism [1]. One current limitation to the density of chambers that can be fabricated is the fluid-handling plumbing overhead which needs to be present for each chamber. To allow independent addressing of all chambers in a grid requires much more device footprint than a chamber normally occupies [1, 5].

Early in the design phase of the cell signaling project, I determined that one of the most important optimization parameters was efficiency of footprint usage within the part of the device actively being imaged (§9.1). At the same time, I wanted a combinatorial grid of chambers within which to perform experiments, and realized that independently addressing them would require much more fluidic overhead than I was willing to devote. High chamber density is possible as long as the chambers do essentially identical things, as in the digital PCR chip design [6], but I still wanted some reconfigurability in the device.

In the end I noticed that my main stumbling block was trying to pack in valves along with chamber walls and route valve access channels around the areas that needed to be imaged. To sneak around this problem, I simply made a big central chamber that could be

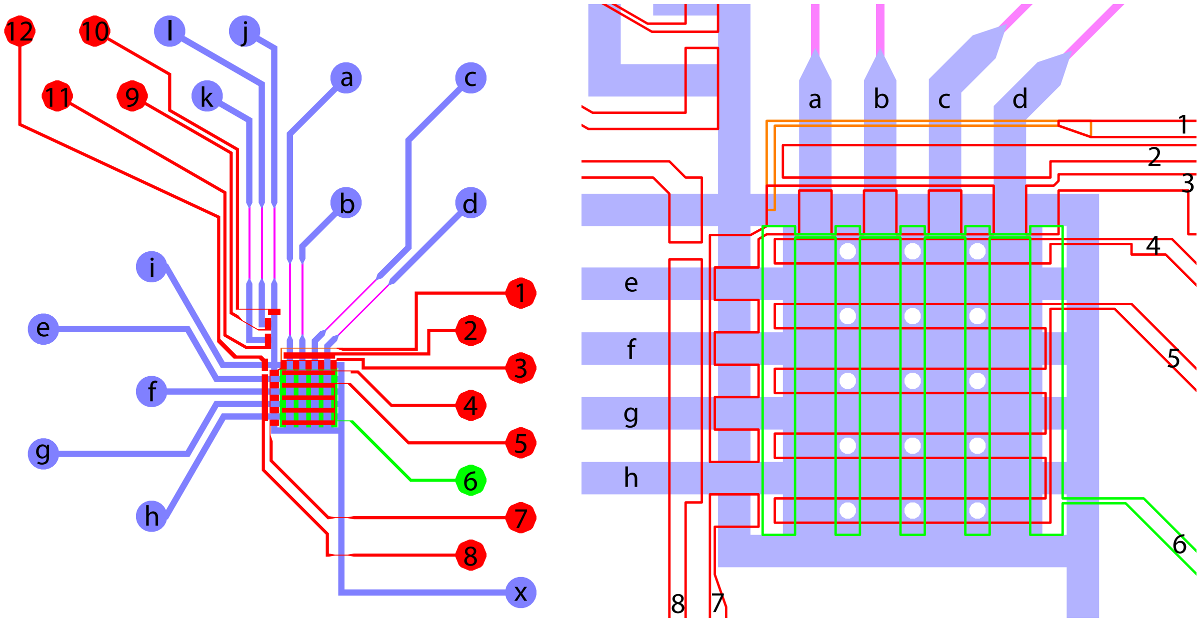

Figure 13.1: Device design using virtual walls, with sixteen experiment chambers which can be addressed either as four columns or four rows. Left, general design layout. Right, close-up of the central region, with the control features in outline for clarity. Control lines are numbered, and flow ports are lettered. Color scheme is essentially the same as that in Fig. 7.1, with the addition of green layer that resides above the flow layer, making a total of three molded layers of PDMS.

subdivided into smaller ones with two sets of valves, one set running lengthwise inside the chamber and the other set running crosswise. I'll call these "ridge valves." Thus, instead of augmenting walls to isolate chambers, the ridge valves, when actuated, formed all the walls separating individual chambers; Prof. Quake suggested the name "virtual walls" for this approach.

Since individual control channels in the same layer cannot cross each other, the two sets of ridge valves must be on separate layers sandwiching the flow layer. When either of the sets of ridge valves are actuated, the chambers can be accessed as either rows or columns. Thus, cells in the chambers can be stimulated on one round in rows, then on the second round in columns, thereby allowing for a combinatorial experiment probing the effects of desensitization and/or pathway crosstalk.

13.1 Device fabrication

The large chamber being subdivided by the virtual walls is a region of very little contact between the flow layer and the push-up control layer. This makes lifting off the push-up layer very difficult if it is to be done with the flow layer. My solution to this problem was to use a “sacrificial” piece of PDMS to transfer the push-up layer from its mold to its PDMS-coated glass substrate (see §B.4). The sacrificial PDMS piece can then be peeled off, and the combined push-down and flow layers aligned and bonded atop the push-up layer to form a completed device. This fabrication has the added benefit that the layer bonds which need to take the most pressure – bonds between the push-down and flow layers, and between the push-up and basement layers – occur fairly early on in the fabrication process and so should be stronger.

I recently learned of a fabrication technique quite similar to this, but using Scotch tape instead of sacrificial PDMS to transfer the thin layer from its mold wafer to its destination (E. Kartalov, personal communication). Presumably that technique could be adapted to this device design, thereby simplifying fabrication.

One problem I had with early versions of the device was delamination of push-up control line inlets as they crossed the flow layer. Clearly the push-up inlets needed to be punched before being bonded to the cover slip, i.e., when the layer was still attached to the sacrificial layer. Thus the corresponding access holes in the push-down and flow layers needed to be punched separately. Initially I used the same inlet mold pattern in the flow layer to denote where to punch those access holes; these patterns had larger footprints than the holes being punched, and it was from those extra spaces that delaminations nucleated (fig. 13.2). Using small dots to guide access hole punches in the flow layer solved this

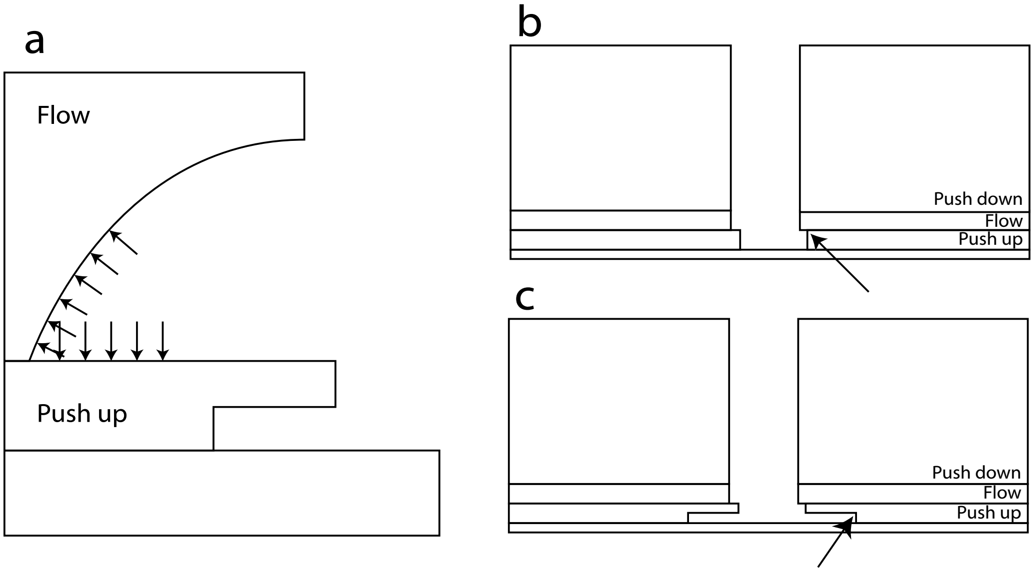

Figure 13.2: Inlet design for four-layer device. (a) initial disposition of control layer inlet, where the flow layer pattern used for guiding hole punching extends beyond the punched hole. Because bonding is weak between flow and push-up layers, applied pressure (indicated by arrows) will tend to peel them apart. (b) Reducing the size of both punching patterns doesn't solve the problem, because positional mismatches arising from alignment errors (black arrow) still give rise to overhangs at which pressure can nucleate delaminations. (c) Using a large punch pattern only on the push-up layer solves the problem: while there are still overhangs, they occur only where the flow layer is bonded to a deformable "flap"; the pressure-drive mechanical load is borne by the (large) area contact between the flow layer and its attached push-up layer flap, and ultimately by the point of attachment of that flap (black arrow). Thus there is no point at which high pressure can force delamination of the bond between flow and push-up layers.

problem and gave much higher control-layer rupture pressures.

13.2 Device function and future work

As shown in fig. 13.3, different configurations of valves allow for different flow geometries. Fig. 13.4 shows placement of adherent HEK293 cells within the device. In this case, the device has been treated with vitronectin (100 μg/ml) with the horizontal ridge valves closed. Those valve surfaces were then passivated with BSA so that, when cells were injected vertically as shown, the cells would be discouraged from adhering to valve surfaces. Note that this works for the most part, with some glaring exceptions: some cells, especially cell clumps, have a tendency to get pinched near the pillared valve crossings (white arrow). The use of lower cell densities and more monodisperse suspensions should make this problem more manageable. Also note that this works even less well for RAW264.7 cells. This is because some RAW cells are in fact able to adhere, though with reduced strength, to PDMS surfaces passivated with BSA. Because there is BSA in the cell suspension media, the adhesion shouldn't happen; presumably the BSA coating isn't complete and RAW cells are able to bind to the PDMS via its scavenger receptors [7]. In fact, RAW cells are able to adhere even to PDMS surfaces coated with poly(ethylene glycol)! This pernicious stickiness of RAW cells, and the fact that I couldn't pack enough cells into each chamber to get a decent population sample, prevented me from using this device for doing actual cell signaling experiments.

The basic idea with the high density array has been demonstrated. With an improved cell seeding technique I'm sure the design will be useful for other adherent cell lines. There are, in addition, other potential applications for this device. For instance, with a small

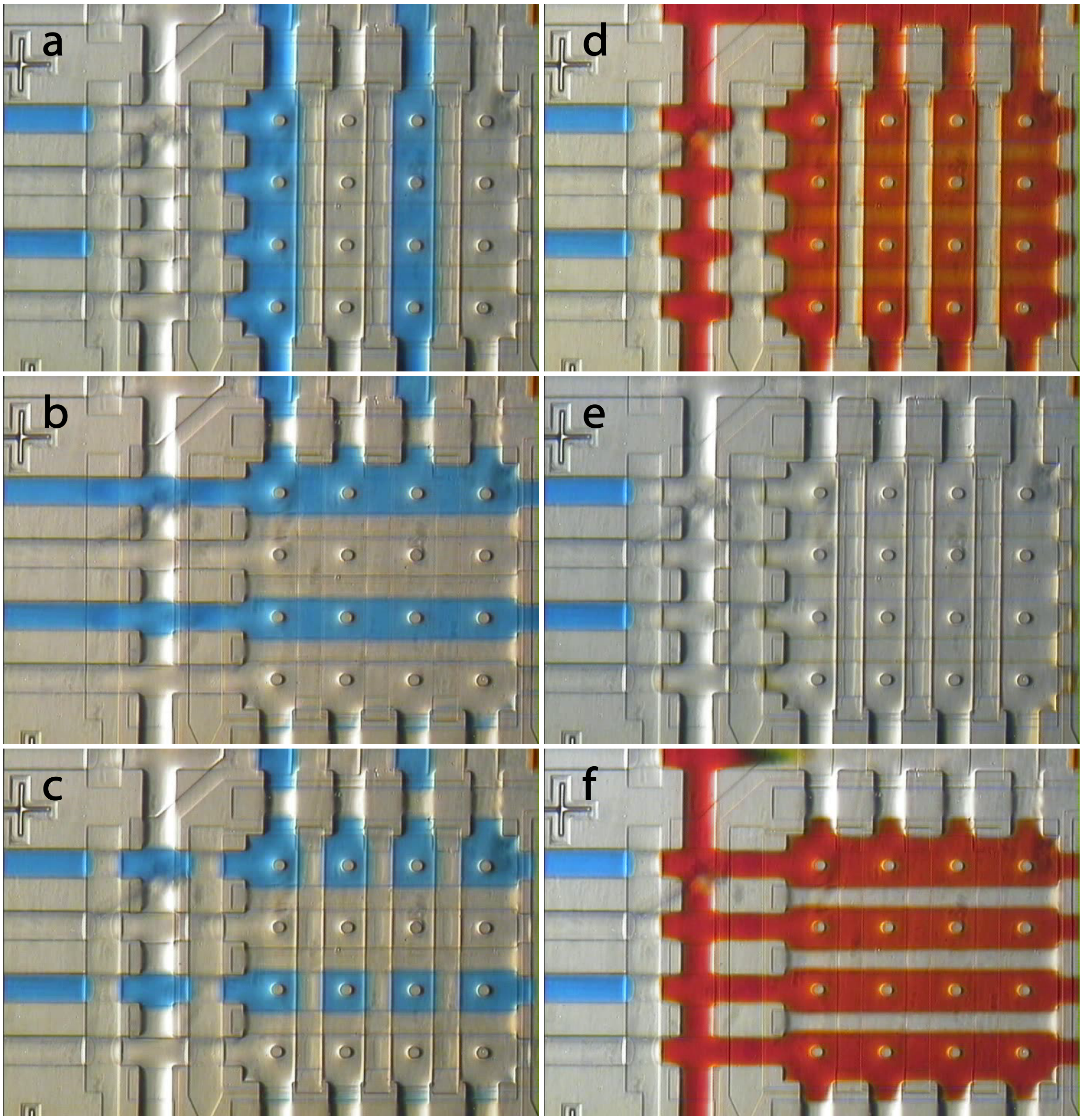

Figure 13.3: Demonstration of different flows achievable with an earlier version of the virtual walls device; the design shown in fig. 13.1 is capable of routing flows in the same way. (a) The chambers in the central grid, with circular pillars at their centers, can be connected columnwise to the column inlet channels and be flushed vertically. (b) Likewise, they can be connected rowwise to the row inlet channels and flushed horizontally. (c) With both sets of barrier valves closed, the channels are isolated from each other, as indicated by the strips of white that now separate the chambers filled with blue dye. (d) We can then flush the entire device with fluid from a manifold inlet which is to the upper left, or (e) with fluid from another manifold inlet. (f) The flush can occur either vertically or horizontally.

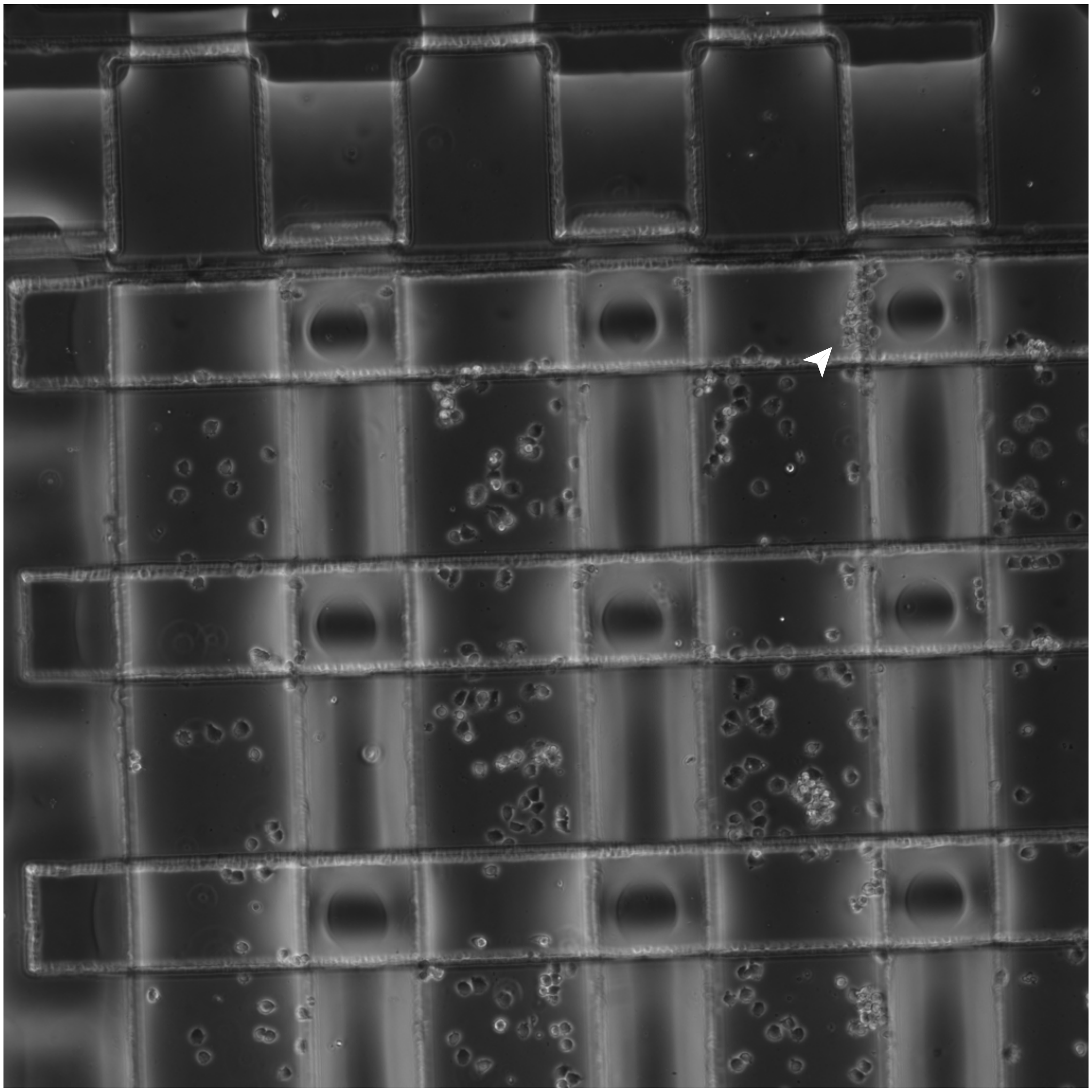

Figure 13.4: HEK293 cells inside a virtual walls device. Device design and orientation are that of fig. 13.1. The use of the dedicated cell injection inlet (flow line i in fig. 13.1), and of BSA passivation, cuts down on cells being trapped in valves and getting crushed by them. This doesn't work completely, though, and the white arrow indicates a clump of cells trapped in a valve area.

tweak in the ridge valve geometry, we should be able to make the valves close in (say) even rows at one pressure and odd rows at a higher pressure. This way we can perform combinatorial mixing experiments at high density, thereby maximizing the use of device footprint and imaging infrastructure.

Bibliography

[1] T. Thorsen, S. J. Maerkl, and S. R. Quake. Microfluidic large scale integration. *Science*, 298:580–584, 2002.

[2] M. L. Adams. *Integration of optoelectronics and microfluidics for biological and chemical sensing*. Ph.D. thesis, California Institute of Technology, 2003.

[3] P. Horowitz and W. Hill. *The Art of Electronics*. Cambridge University Press, 2nd ed., 1989.

[4] V. Studer, G. Hang, A. Pandolfi, M. Ortiz, W. F. Anderson, and S. R. Quake. Scaling properties of a low-actuation pressure microfluidic valve. *J. Appl. Phys.*, 95(1):393–8, 2004.

[5] J. Liu, C. Hansen, and S. R. Quake. Solving the "world-to-chip" interface problem with a microfluidic matrix. *Anal. Chem.*, 75:4718–23, 2003.

[6] E. A. Ottesen, J. W. Hong, S. R. Quake, and J. R. Leadbetter. Microfluidic digital PCR enables multigene analysis of individual environmental bacteria. *Science*, 314(5804):1464–67, 2006.

[7] I. Fraser, D. Hughes, and S. Gordon. Divalent cation-independent macrophage adhesion inhibited by monoclonal antibody to murine scavenger receptor. *Nature*, 364(6435):343–6, 1993.

Part IV

Appendices

Appendix A

Flow rates inside microfluidic channels

I needed to set flow speeds in microfluidic channels by tuning channel resistances (§7.4). For this purpose I give here the design equations used to compute the expected flow rates in microfluidic channels. In addition, since many mammalian cells are sensitive to flow shear, I also consider the surface shear stress induced by fluid flow in channels.

A.1 Rounded channels

Using the creeping flow approximation (low Reynolds number), we have for the flow profile along any given orthogonal channel cross-section:

$$\mu\nabla^2 u = -G, \tag{A.1}$$

where G is the pressure gradient. Assuming that height variations are on a length scale much larger than the heights themselves, we can take $\frac{\partial^2 u}{\partial y^2}$ to be the dominant term in $\nabla^2 u$. So, for a height function $h\left(x\right)$, we have flow profile:

$$u = \frac{G}{2\mu} y \left(h\left(x\right) - y\right). \tag{A.2}$$

Let's take the height to be a parabola with width w: $h\left(x\right)=\frac{4h}{w^2}x\left(w-x\right)$. The flow rate is easy to calculate:

$$\begin{aligned}
\phi &= \int_0^w \mathrm{d}x \int_0^{h(x)} \mathrm{d}y\, u\left(x,y\right) \\
&= \int_0^w \mathrm{d}x\, \frac{2}{3}h\cdot\frac{G}{2\mu}\frac{h^2}{4} \\
&= \frac{G}{12\mu}\int_0^w h^3 \mathrm{d}x \\
&= \frac{G}{12\mu}\left(\frac{4h}{w^2}\right)^3 \int_0^w x^3\left(w-x\right)^3 \mathrm{d}x \\
&= \frac{G}{12\mu}\left(\frac{4h}{w^2}\right)^3 \frac{w^7}{140} \\
&= \frac{4}{105}\frac{G}{\mu}h^3 w, \qquad \text{(A.3)}
\end{aligned}$$

as is the surface stress:

$$\begin{aligned}
\sigma &= \mu\frac{\partial u}{\partial y} \\
&= \frac{Gh\left(x\right)}{2} \qquad \text{(A.4)} \\
&= \frac{h\left(x\right)}{2}\frac{105\mu\phi}{4h^3 w} \qquad \text{(A.5)}
\end{aligned}$$

so that the maximal stress, experienced in the center of the channel, is

$$\sigma_{\max}=\frac{105\mu\phi}{8h^2 w}. \qquad \text{(A.6)}$$

A.2 Square channels

A.2.1 Large aspect ratio approximation

If we take the aspect ratio to be large, i.e., $w \gg h$, we can simply approximate that the edge effects are small. In this case, we still have

$$u = \frac{G}{2\mu} y \left(h - y\right) \tag{A.7}$$

and thus

$$\begin{aligned} \phi &= \frac{G}{2\mu} \frac{2}{3} h w \frac{h^2}{4} \\ &= \frac{G w h^3}{12\mu} \qquad \text{(A.8)} \\ \sigma &= \mu \frac{\partial u}{\partial y} \\ &= \frac{G h}{2}. \qquad \text{(A.9)} \end{aligned}$$

(σ here denotes the stress at the bottom of the channel.)

A.2.2 Exact solution (power expansion)

We need to solve the boundary value problem (eq. A.1) subject to the boundary condition $u = 0$ on the edges $x = 0$, $x = w$, $y = 0$, $y = h$.

To make life easier, let's split u up into two pieces

$$u = u_1 + u_2,$$

where u_1 is just our approximate solution $u_1 = \frac{G}{2\mu} y \left(h - y\right)$. Now u_1 already satisfies the upper and lower boundary conditions, so we just need a harmonic function u_2 (i.e., $\nabla^2 u_2 = 0$) that is zero on the top and bottom edges and cancels out u_1 on the left and right edges: $u_2 = -\frac{G}{2\mu} y\,(h-y)$ on $x = 0$ and $x = w$. Note that we can do a Fourier expansion on the boundary condition:

$$-\frac{G}{2\mu} y\,(h-y) = \sum_{j\,\mathrm{odd}} a_j \sin\frac{\pi j y}{h} \tag{A.10}$$

(j odd since the function is symmetric across $y = \frac{h}{2}$). The sine functions in y give rise to exponentials in the x direction to solve Laplace's equation, so we get our full solution

$$u_2 = \sum_{j\,\mathrm{odd}} a_j \sin\frac{\pi j y}{h} \frac{\cosh\frac{\pi j (x - w/2)}{h}}{\cosh\frac{\pi j w}{h 2}}, \tag{A.11}$$

which is clearly harmonic and satisfies boundary conditions. (N.B.: This is just doing a separation-of-variables on Laplace's equation.) To get the coefficients a_j we just do a Fourier decomposition:

$$\begin{aligned} a_j &= \frac{2}{h}\int_0^h \frac{G}{2\mu} y\,(y-h) \sin\frac{\pi j y}{h}\mathrm{d}y \\ &= -\frac{4Gh^2}{\pi^3 \mu j^3} \end{aligned} \tag{A.12}$$

by Mathematica. So the full velocity field is:

$$u = \frac{G}{2\mu} y\,(h-y) - \frac{4Gh^2}{\pi^3 \mu} \sum_{j\,\mathrm{odd}} \frac{1}{j^3} \sin\frac{\pi j y}{h} \frac{\cosh\frac{\pi j (x - w/2)}{h}}{\cosh\frac{\pi j w}{h 2}}. \tag{A.13}$$

As for the flow rate, let's look at each Fourier component:

$$\begin{aligned}
\phi_j &= \frac{4Gh^2}{\pi^3 j^3 \mu} \int_0^w \mathrm{d}x \int_0^h \mathrm{d}y \, \sin\frac{\pi j y}{h} \frac{\cosh\frac{\pi j(x-w/2)}{h}}{\cosh\frac{\pi j w}{h2}} \\
&= \frac{4Gh^2}{\pi^3 j^3 \mu \cosh\frac{\pi j w}{h2}} \int_0^w \cosh\frac{\pi j(x-w/2)}{h} \mathrm{d}x \int_0^h \sin\frac{\pi j y}{h} \mathrm{d}y \\
&= \frac{4Gh^2}{\pi^3 j^3 \mu \cosh\frac{\pi j w}{h2}} \left(\frac{2h}{\pi j}\right) \left(\frac{2h}{\pi j} \sinh\frac{\pi j w}{2h}\right) \\
&= \frac{16Gh^4}{\pi^5 j^5 \mu} \tanh\frac{\pi j w}{2h}. \qquad \text{(A.14)}
\end{aligned}$$

So, letting $\alpha = w/h$ be the aspect ratio, we have

$$\begin{aligned}
\phi &= \frac{Gwh^3}{12\mu} - \sum_{j\,\mathrm{odd}} \phi_j \\
&= \frac{Gwh^3}{12\mu} - \frac{16Gh^4}{\pi^5 \mu} \sum_{j\,\mathrm{odd}} \frac{1}{j^5} \tanh\frac{\pi j w}{2h} \\
&= \frac{Gwh^3}{12\mu} \left[1 - \frac{192}{\pi^5 \alpha} \sum_{j\,\mathrm{odd}} \frac{1}{j^5} \tanh\frac{\pi j \alpha}{2}\right]. \qquad \text{(A.15)}
\end{aligned}$$

The fifth power in j means that the series converges extremely rapidly at first; taking just the first term is good enough to get within 1% for any reasonable value of α. On the other hand, that correction is first-order in α, so is nonnegligeable even for modestly large values of α.

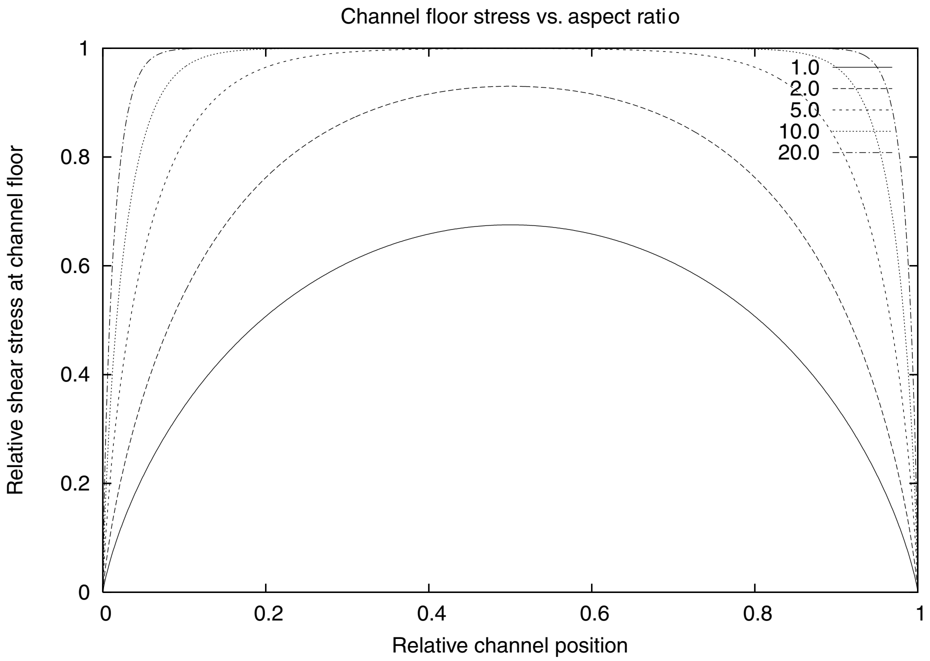

Figure A.1: Shear stress inside a rectangular channel

Finally, the shear stress at the channel floor is:

$$\begin{aligned}
\sigma &= \mu \left.\frac{\partial u}{\partial y}\right|_{y=0} \\
&= \frac{Gh}{2} - \frac{4Gh^2}{\pi^3} \sum_{j\,\mathrm{odd}} \frac{1}{j^3} \frac{\pi j}{h} \frac{\cosh \frac{\pi j (x - w/2)}{h}}{\cosh \frac{\pi j w}{h 2}} \\
&= \frac{Gh}{2} - \frac{4Gh}{\pi^2} \sum_{j\,\mathrm{odd}} \frac{1}{j^2} \frac{\cosh \frac{\pi j (x - w/2)}{h}}{\cosh \frac{\pi j w}{h 2}} \\
&= \frac{Gh}{2} \left[1 - \frac{8}{\pi^2} \sum_{j\,\mathrm{odd}} \frac{1}{j^2} \frac{\cosh \pi j \alpha \left(\frac{x}{w} - \frac{1}{2}\right)}{\cosh \frac{\pi j \alpha}{2}} \right].
\end{aligned} \tag{A.16}$$

The bracketed quantity here is plotted in fig. A.1. Note that the exponent on j is only 2 this time; this is because we're differentiating in the y direction, instead of integrating in both directions, so the higher order Fourier components give more of a contribution. Fortunately, at high enough j, the terms actually decrease exponentially. It's easy to show that $\cosh\left(\frac{\pi j \alpha}{2} - \frac{\pi j x}{h}\right) / \cosh \frac{\pi j \alpha}{2}$ always decreases with increasing j, so that we can provide a lower bound on σ:

$$\begin{aligned}\sigma &> \frac{Gh}{2}\left[1-\frac{8}{\pi^2}\sum_{j\,\mathrm{odd}}\frac{1}{j^2}\frac{\cosh\left(\frac{\pi\alpha}{2}-\frac{\pi x}{h}\right)}{\cosh\frac{\pi\alpha}{2}}\right]\\ &= \frac{Gh}{2}\left[1-\frac{\cosh\left(\frac{\pi\alpha}{2}-\frac{\pi x}{h}\right)}{\cosh\frac{\pi\alpha}{2}}\right]. \qquad \text{(A.17)}\end{aligned}$$

Now, in the case where α is large, we can simplify further:

$$\begin{aligned}\sigma &\gtrsim \frac{Gh}{2}\left[1-\frac{\exp\left(\frac{\pi\alpha}{2}-\frac{\pi x}{h}\right)}{\exp\frac{\pi\alpha}{2}}\right]\\ &= \frac{Gh}{2}\left[1-\exp\left(-\frac{\pi x}{h}\right)\right] \qquad \text{(A.18)}\end{aligned}$$

for $x \ll w$. Thus the characteristic decay length (decaying *towards* the full value as we move away from the side walls) will be at least as short as $\frac{h}{\pi}$.

Appendix B

Fabrication protocols

B.1 General comments

All device fabrication is performed in the Micro/nano fabrication facility at Caltech. Photoresist spinning is done on a Laurell Technologies spin coater, and mask alignment and UV exposure are performed on a Karl Suss MJB-3 mask aligner. PDMS is mixed in a Keyence HM-501 mixer, with a 1 min mix cycle and 5 min degas cycle to remove bubbles from the viscous uncured PDMS mixture. PDMS baking steps are always at 80°C inside a Fisher Scientific Isotemp convection oven. Holes in the PDMS are punched in a Schmidt press with punch tools from Technical Innovations (P/N CR0350255N20R4). Layer alignment is performed by hand on a standard dissection microscope.

Molds are fabricated atop 3-inch silicon wafers, which have enough space for four devices of the sizes used in all my work shown here.

Flow constrictions, and other features that do not require rounding via reflow, are defined using SU8 photoresists. After hard bake steps of ~200°C for 30 min, these features become effectively indestructible. The SU8 developer used to remove uncrosslinked SU8 does tend to leave a trace film that can interfere with further processing, so wafers are always washed with acetone and isopropyl alcohol (IPA) after each development and hard bake step.

Rounded channels are fabricated using photoresists that can be melted and reflowed after development — either AZ-50 or SPR 220-7. SPR 220-7 is used for thin ($\sim$10 μm) features, and the AZ-50 photoresist is used for thicker ($\sim$45 μm after reflow) features; I had been using AZ-100 until it was discontinued. In any case the AZ-100 photoresist, when developed, was much more brittle and temperature-sensitive than AZ-50, so later molds made using AZ-50 were much more durable. Because AZ resists are thick and rather fragile, AZ features are usually applied last.

Photoresist spin steps are 1 min in length, with a typical acceleration parameter of "10" in the Laurell spin controller. Changing acceleration speeds did not appear to have appreciable effects on feature thickness.

The presence of tall SU8 features tends to make the spun layer uneven in thickness, so I let the resist settle for at least 5 min after spinning and before the pre-expose bake step. In addition, the unrounded features introduce air bubbles when a viscous AZ photoresist is spun over them. Small air bubbles usually collapse due to surface tension-induced pressure, but those that remain can expand greatly during the pre-exposure hardening bake step and, when present in feature-bearing regions, can destroy molds. For this reason, when spinning AZ photoresists onto wafers with tall (20-30 μm) SU8 features, I stop the first spin as soon as the AZ photoresist spreads out over the first wafer, add more photoresist to the center of the wafer, and then finish the spin. Air bubbles are then pushed out towards the periphery of the mold and eventually taken off the mold by the excess photoresist. Addition of the extra photoresist needs to occur very soon after the initial resist spread, since later on in the spin process the photoresist begins to dry, preventing the newly added photoresist from mixing with the old.

All photoresist bake steps, unless otherwise indicated, are at 95°C for SU8 and 115°C for AZ50.

Before being used to mold PDMS, molds must be treated with TMCS vapors to prevent bonding to the PDMS being molded. I use treatments lasting about 5 min before each mold use. Long exposures to TMCS tends to ease subsequent removal of the molded PDMS layer.

Devices are fabricated using Dow Corning Sylgard 184, which comes in 1.1 lb (0.5 kg) kits consisting of 1 lb of the uncured elastomer base and 0.1 lb of the curing agent. I use Sylgard for its fast cure time and find that finished devices are no more susceptible to delamination than are those fabricated with GE RTV. Spin coat steps are at speed for 1 min, with acceleration and deceleration occurring over 15 s. Because Sylgard cures so quickly, dishes being cured are not stacked in the oven to reduce uneven heating.

B.2 Cell signaling devices

The two device designs shown in fig. 7.1 use identical mold and device fabrication protocols.

B.2.1 Mold fabrication

Wash silicon wafers with acetone and then IPA on the Laurell spin coater to remove any contaminants that may interfere with processing. Bake at $>$ 100°C to dry.

For flow constrictions and control layer cross-unders, spin SU8-2010 at 3 kprm. Bake at 95°C for 2 min, expose in the mask aligner for 1 min (hard contact), bake at 95°C again for 2 min, and then develop with SU8 developer. Hard bake at 170°C for ¿10 min and then let cool gently. Wash with acetone and IPA on the spin coater.

For unrounded cell channels, spin SU8-2025 at 3 krpm; for control layer channels and pads, spin SU8-2025 at 2 krpm. Bake for 2 min at 65°C, then 5 min at 95°C. Expose for 1 min, and bake again at 95°C for 4 min. The extra post-expose bake time, compared with the manufacturer's recommendation, is to enhance photoresist adhesion to the silicon substrate. Hard bake and wash as above.

Expose the flow layer mold to HMDS vapors for 1.5 min. Spin AZ50 onto the flow layer mold in two steps, as described above, at 1 krpm. AZ50 is kept in the refrigerator and is to be spun cold. After letting the photoresist settle for 5 min, bake for 2.5 min at 65°C, 5 min at 115°C, and then 2.5 min more at 65°C. Expose for 4.5 min, and develop with 1 part 2401 developer mixed into 4 parts distilled, de-ionized water.

Rounding is accomplished by ramping the wafer up from room temperature to 130°C on a hotplate. After the hotplate has spent 5-10 min above 125°C, it is turned off so that the wafer cools down slowly; rapid temperature changes will cause the AZ50 resist to crack.

B.2.2 Device fabrication

TMCS treat control and flow layer molds. Wash four cover slips (24x30 mm or 22x30 mm) with ethanol and then water. Blow them dry.

Pour 7:1 Sylgard (7 parts base to 1 part curing agent) onto the flow layer mold. Degas the flow layer inside a vacuum-pumped bell jar. Spin 7:1 Sylgard onto the cover slips at 4 krpm.

Spin 20:1 Sylgard onto the control layer mold at 1.4 krpm. Note that this is optimized for Sylgard 184 batch #0002342505; other batches require slightly different spin speeds to yield resilient control layers with valves that actuate at reasonable pressures.

Bake the flow layer for 13 min as the spun Sylgard is left to settle. After the flow layer is done curing, bake the spun Sylgard layers for 13 min. While the spun layers are baking, dice the flow layer into four pieces, one for each device. Punch the outlet ports for each of them to allow air to escape after alignment.

After the spun layers are finished baking, remove them. Align the flow layer pieces onto their respective patterns on the control layer mold. Squeeze any remaining air bubbles from between the two layers and bake for 25 min.

Cut the control layer at the edges of the flow layer pieces using a scalpel. Peel the control layers off carefully, making sure that they remain attached to the flow layer and don't tear.

Punch ports into the control/flow layer combinations. The extra membrane on top of flow layer ports protects them from contamination by the PDMS shards that are generated at the punch tool tip.

Press the control/flow layer chunks onto cover slips. Squeeze air bubbles out and bake overnight. Remove promptly, as overbaking reduces gas permeability and increases the chance of an air bubble being generated within the device during an experiment.

B.3 Amplifying valves

The top (control) layer mold was SU8-2010, spun at 1 krpm to give 20 μm high features. The middle (cushion) layer mold was AZ100 spun at 1.2 krpm to give $\simeq$45 μm features. The bottom (flow) layer mold was SPR 220-7 spun at 1.5 krpm to give 12 μm features. All molds were baked in an oven at 170°C for about 2 hrs, to round the channels in the middle and bottom layers and to enhance mold resiliency for all layers; AZ100 and SPR 220-7 feature heights quoted above are after rounding.

From these molds, chips were fabricated as follows: Sylgard mixed in a 5:1 ratio was poured onto the top layer and spun at 4 krpm onto 1.5″x1″ glass slides. Sylgard mixed in a 20:1 ratio was spun onto the middle layer at 1.2 krpm and the top layer at 2.5 krpm. Wafers were baked at 80°C for 25 min; slides were baked for 35 min. The top layer was peeled, punched, aligned to the middle layer, and baked at 80°C for 20 min. These were cut, peeled, punched, aligned to the bottom layer, and again baked for 20 min. They were then cut, peeled, punched, and pressed against the thin Sylgard layer cured atop the glass slides. The completed devices were cured overnight.

B.4 Virtual walls

B.4.1 Device-specific comments

Sacrificial layer cure time is critical. Deviations of 5 min either way, especially on the longer side, may cause fabrication to fail.

This protocol was optimized for Dow Corning Sylgard 184, batch #2180679.

Wafer assignments: A is flow layer. B is push-up layer. C is push-down layer. Mold fabrication is essentially as in §B.2.1, with the C layer fabrication identical to the second control layer SU8 step.

B.4.2 PDMS protocol

Put some TMCS into an incubation chamber (really just a Tupperware container). Put molds A, B, and C, and blank wafer, into the chamber. Seal the lid.

In the 5:1 cup, add 4 g curing agent into 28 g Sylgard base. Mix with program 3.

Meanwhile, add 25 g Sylgard base and 1.2 g curing agent in 20:1 cup, and mix with program 3 when the “5:1” (actually 7:1) is done mixing. Also use tin foil to line all wafer dishes and a fifth dish for the cover slips. At some point blow clean four cover slips (24x30) and put them into the fifth dish.

While 20:1 is mixing, pour 7:1 onto wafer C and start degassing in the bell jar. Leave a few grams for the cover slips.

After 20:1 is done mixing, spin it onto wafer B (40 μm features) at 1000 rpm. Also spin it onto wafer A at 1200 rpm.

Add 0.4 g curing agent to the remaining 20:1 Sylgard and mix again.

While this is mixing, spin 7:1 onto cover slips at 4000 rpm.

When 20:1 is done mixing the second time, pour it over the blank wafer. Press down on the center of the wafer (gently!) to get rid of the trapped air.

Put dishes (5 total) in the oven.

After 13 min, take out the cover slips and wafers A and C. Peel and dice layer C.

After 16 min, take out wafer B.

Align chunks C to patterns on wafer A. Cure this in the oven for 20 min.

After 31 min, take out sacrificial (blank) wafer.

Dice blank PDMS into 4 chunks, approx. 1 in square each. Press them against patterns on wafer B. Cure this in the oven for 20 min.

Slice and peel chunks off of wafer A. Punch the flow layer ports as well as access holes for the control layer, marked by dots in the flow layer. I find it is easy to align the punch tool by centering the punched feature between the tool and its reflection off the PDMS surface.

When sacrificial/B bond is complete, slice and peel chunks off wafer (carefully!). Punch. Press chunks against cover slips. Cure this for 20 min.

Continue to punch flow layer.

When sacrificial/B/cover slip bond is done, don’t take everything out of the oven. Take the cover slips out one by one, and peel the sacrificial layer off immediately after they are taken out of the oven. Be careful not to peel with too much force, as this will crack the cover slip.

Align C chunks to the cover slips. This is made easier if you tape the cover slips by their flanges on to the microscope stage.

Final bonding occurs overnight.

Appendix C

Protocols for cell signaling

C.1 Protocols from the AfCS

Many of the biochemical protocols associated with the signaling project were derived from protocols developed for calcium assays by the Alliance for Cellular Signaling. The relevant protocols can be downloaded from `http://www.signaling-gateway.org`, and are also reproduced here.

AfCS Ligand Protocol

Reagent name: Complement C5a, human, recombinant

Reagent name abbreviation: C5a, human, recombinant

Protocol ID: PL00000016

Version: 01

Volume: 232 µl

Components:

Reagent	Source	Catalog or Protocol No.	F.W. or Stock Conc.	Quantity	Final Concentration
C5a, human, recombinant	Sigma-Aldrich	C5788	8600	100 µg	50 µM
1X PBS/0.4% BSA	None	PS00000609	NA	232 µl	1X

Ligand stock preparation:

1. Add 232 µl of 1X PBS/0.4% BSA to the vial of C5a.
2. Allow solute to dissolve completely and mix thoroughly.
3. Prepare bar codes and label 0.6-ml Eppendorf tubes.
4. Divide 12-µl aliquots into tubes on ice.
5. Freeze in liquid nitrogen and store aliquots at –80 °C.

Storage:

Temperature: –80 °C
Location: _________________
Aliquot size: 12 µl
Special instructions: None

Example: dilution of ligand for treatment of cells at 250 nM for dual ligand screen:*

1. Dilute ligand no earlier than 1 hr before use.
2. Thaw ligand stock on ice.
3. Dilute 10 µl of ligand stock with 90 µl of appropriate assay medium. Pipette up and down with micropipette to mix. This yields a 20X treatment stock.
4. Dilute 50 µl of second dilution in 50 µl of desired assay medium (for treatment with ligand alone) or 50 µl of a 20X stock of another ligand in a 0.6-ml microfuge tube on ice. Invert repeatedly to mix. The final concentration of C5a before use is 2.5 µM.
5. Keep diluted ligand on ice. Immediately before use, warm ligand solution to 37 °C in an environmental chamber.

Author: Keng-Mean Lin

Date: 01/06/04

Approved: Paul Sternweis

***Comments:** For purposes of the dual ligand screen, a 20X stock of individual ligands is prepared initially. From the 20X stock, a 10X stock is prepared by mixing equal volumes with assay medium or another 20X stock of a different ligand. Note that different assays use different assay media and may require different stock concentrations for addition of the ligand to the assay (see protocols for specific assays).

AfCS Ligand Protocol

Reagent name: Uridine 5′-diphosphate sodium salt, 80 millimolar

Reagent name abbreviation: UDP, 80 mM

Protocol ID: PL00000266

Version: 01

Volume: 1 ml

Components:

Reagent	Source	Catalog or Protocol No.	F.W. or Stock Conc.	Quantity	Final Concentration
UDP	Sigma-Aldrich	U4125	511*	40.9 mg	80 mM
Distilled water	Invitrogen	15230162	NA	1 ml	NA

*F.W. can change from lot to lot based on content of water and solvent. Lot used: 042K7052.

Ligand stock preparation:

1. Weigh 40.9 mg of UDP in a 1.5-ml Eppendorf tube.
2. Add 1 ml of distilled water to tube with UDP.
3. Mix thoroughly and allow solute to dissolve completely.
4. Prepare bar codes and label 0.6-ml Eppendorf tubes.
5. Divide 20-µl aliquots into tubes on ice.
6. Freeze in liquid nitrogen and store aliquots at –80 °C.

Storage:

Temperature: –80 °C
Location: _________________
Aliquot size: 20 µl
Special instructions: None

Example: dilution of ligand for treatment of cells at 25 µM for dual ligand screen:†

1. Dilute ligand no earlier than 1 hr before use.
2. Thaw ligand stock on ice.
3. Dilute 10 µl of ligand stock with 90 µl of appropriate assay medium. Pipette up and down with micropipette to mix. Dilute 60 µl of first dilution in 900 µl of desired assay medium in a 1.5-ml microfuge tube on ice. Invert repeatedly to mix. This yields a 20X treatment stock.
4. Dilute 500 µl of second dilution in 500 µl of desired assay medium (for treatment with ligand alone) or 500 µl of a 20X stock of another ligand in a 1.5-ml microfuge tube on ice. Invert repeatedly to mix. The final concentration of UDP before use is 250 µM.
5. Keep diluted ligand on ice. Immediately before use, warm ligand solution to 37 °C in an environmental chamber.

Author: Keng-Mean Lin

Date: 11/21/03

Approved: Paul Sternweis

AfCS Ligand Protocol

Reagent name: L-alpha-phosphatidylcholine, beta-acetyl-gamma-O-alkyl (platelet activating factor), 20 millimolar

Reagent name abbreviation: PAF, 20 mM

Protocol ID: PL00000038

Version: 01

Volume: 477 µl

Components:

Reagent	Source	Catalog or Protocol No.	F.W. or Stock Conc.	Quantity	Final Concentration
PAF	Sigma-Aldrich	P7568	Approx. 524	5 mg	20 mM
Ethanol	Aaper Alcohol	030801	100%	477 L	100%

Ligand stock preparation:

1. Add 477 µl of ethanol to the vial of PAF.
2. Mix thoroughly and allow solute to dissolve completely.
3. Prepare barcodes and label amber glass vials.
4. Divide 100-µl aliquots into barcoded vials.
5. Fill vials with argon gas and seal vials.
6. Store aliquots at –80 °C.

Storage:

Temperature: –80 °C
Location: ___________________
Aliquot size: 100 µl
Special instructions: None

Dilution for treatment of cells at 100 nM:*

1. Dilute the ligand no earlier than 1 hr before use.
2. Thaw the ligand stock on ice.
3. Dilute 10 µl of ligand stock in 990 µl of Supplemented Iscove's Modified Dulbecco's Medium (SIMDM) in a 2-ml Eppendorf tube on ice. Invert several times to mix. Dilute 75 µl of the first dilution in 1425 µl of SIMDM in a 2-ml Eppendorf tube on ice, and invert several times to mix. Dilute 150 µl of the second dilution in 1350 µl of SIMDM in a 2-ml Eppendorf tube on ice, and invert several times to mix. The final concentration before use is 1 µM.
4. Keep the diluted ligand on ice until ready to use. Warm the ligand solution to 37 °C in an environmental chamber immediately before use.

Author: Robert Hsueh

Date: 07/03/02

Approved: Zhen Yan

***Comments:** Our preliminary experiments did not show positive responses in primary B cells at a concentration as high as 4 nM. Therefore, we chose this concentration based on previous findings by Zhang et al. (J Biol Chem, 277[5]:2851, 1999). For use in calcium assays, dilute the ligand in Hanks' Balanced Salt Solution—Bovine Serum Albumin (HBSS-BSA), following the same procedure.

AfCS Solution Protocol

Reagent name: RAW 264.7 growth medium 1

Reagent name abbreviation: RAWGM1

Protocol ID: PS00000510

Version: 01

Volume: 500 ml

Components:

Reagent	Source	Catalog or Protocol No.	F.W. or Stock Conc.	Quantity	Final Concentration
Dulbecco's Modified Eagle's Medium (DMEM)	ATCC	30-2002	1X	435 ml	0.87X
Heat-inactivated fetal bovine serum (FBS)	Gemini Bio-Products	100-500 lot# A40802W	100%	50 ml	10%
HEPES	Invitrogen	15630080	1 M	10 ml	20 mM
L-Glutamine	Invitrogen	25030081	200 mM	5 ml	2 mM

Preparation:

1. The serum should be heat inactivated, as described in AfCS protocol PS00000247.
2. Pour 250 ml of DMEM into the top chamber of a 0.2- m 1-L Nalgene SFCA filter unit in hood using the gradations on the top chamber.
3. Add the non-medium components with a pipette.
4. Bring the solution in the top chamber to volume with DMEM.
5. Cover and apply suction to filter.
6. Remove filter compartment and cap. Swirl to mix.

Storage:

Temperature: 4 °C
Location: ________________
Aliquot size: NA
Special instructions: None

Author: Robert Hsueh and Tamara Roach

Date: 08/20/03

Approved: Paul Sternweis

Comments: Macrophages are extremely sensitive to lipopolysaccharide (LPS) endotoxin from Gram-negative bacteria. All solutions, buffers, and media should be made with sterile, tissue-culture grade, endotoxin-tested water. To limit potential LPS contamination, use disposable sterile plastic rather than laboratory glassware.

AfCS Solution Protocol

Reagent name: Hanks' balanced salt solution-bovine serum albumin with 2.5 mM probenecid, pH 7.45, low LPS

Reagent name abbreviation: HBSS-BSA-probenecid, pH 7.45, low LPS

Protocol ID: PS00000589

Version: 01

Volume: 50 ml

Components:

Reagent	Source	Catalog or Protocol No.	F.W. or Stock Conc.	Quantity	Final Concentration
HEPES-HBSS, 1X, low LPS	None	PS00000628	1X	48.98 ml	1X
Probenecid, low LPS	None	PS00000604	500 mM	0.25 ml	2.5 mM
Bovine serum albumin (BSA)	Sigma-Aldrich	A8918	35%	714 l	0.5 %
Sodium hydroxide (NaOH), low LPS	None	PS00000576	1 N	50 l	NA

Preparation:

1. Combine liquid ingredients into a sterile, pyrogen-free 50-ml conical tube.
2. Close and mix well by inversion.
3. Remove a small aliquot to verify that pH is between 7.35 and 7.45.
4. If pH is below 7.35, add small amount of NaOH to buffer.
5. Repeat steps 3 and 4 until pH is 7.45.

Storage:

Temperature: Room temperature
Location: _________________
Aliquot size: NA
Special instructions: None

Author: Mary Verghese

Date: 11/03/03

Approved: Grischa Chandy

Comments: Macrophages are extremely sensitive to lipopolysaccharide (LPS) endotoxin from Gram-negative bacteria. All solutions, buffers, and media should be made with sterile, tissue-culture grade, endotoxin-tested water. To limit potential LPS contamination, use disposable, sterile plastic rather than laboratory glassware.

AfCS Solution Protocol

Reagent name: Fmin solution, 5X

Reagent name abbreviation: 5X Fmin solution

Protocol ID: PS00000607

Version: 01

Volume: 2 ml

Components:

Reagent	Source	Catalog or Protocol No.	F.W. or Stock Conc.	Quantity	Final Concentration
Ionomycin, 10 mM	None	PS00000570	10 mM	10 l	50 M
Thapsigargin, 1 mM	None	PS00000569	1 mM	10 l	5 M
0.1 M EGTA, pH 7.6	None	PS00000420	0.1 M	200 l	10 mM
HBSS-BSA-probenecid, pH 7.45	None	PS00000574	NA	1.78 ml	NA

Preparation:

1. Measure the HBSS-BSA-probenecid solution into a 15-ml Falcon tube. Add the other components listed above in the quantities indicated.
2. Vortex briefly to ensure thorough mixing.
3. Use immediately or store on ice (less than 30 min). Warm in a 37 °C water bath directly prior to use.

Storage:

Temperature: NA
Location: ___________________
Aliquot size: NA
Special instructions: Do not store solution. Prepare fresh for each use.

Author: David Quan

Date: 01/05/03

Approved: Tamara Roach

Comments: None

AfCS Solution Protocol

Reagent name: Fmax solution, 6X

Reagent name abbreviation: 6X Fmax solution

Protocol ID: PS00000608

Version: 01

Volume: 2 ml

Components:

Reagent	Source	Catalog or Protocol No.	F.W. or Stock Conc.	Quantity	Final Concentration
Calcium chloride ($CaCl_2$), 1 M	None	PS00000422	1 M	240 l	120 mM
HBSS-BSA-probenecid, pH 7.45	None	PS00000574	NA	1.76 ml	NA

Preparation:

1. Add the HBSS-BSA-probenecid to a 15-ml Falcon tube using a P1000 pipetman, then add the 1 M $CaCl_2$.
2. Vortex briefly to ensure thorough mixing.
3. Use immediately or store on ice (for less than 1 hr). Warm in a 37 °C water bath directly prior to use.

Storage:

Temperature: NA
Location: ___________________
Aliquot size: NA
Special instructions: Do not store solution. Prepare fresh for each use.

Author: David Quan

Date: 01/05/04

Approved: Tamara Roach

Comments: None

Live Single-Cell Fura-2 Measurements to Determine the Intracellular Free Calcium in RAW 264.7 Cells (with Olympus IX81)

AfCS Procedure Protocol PP00000188
Version 1, 2/10/04

This protocol describes a method to assess concentrations of free cytoplasmic calcium, $[Ca^{2+}]_i$, for cultured adherent RAW 264.7 cells in an 8-well coverglass. This objective is accomplished using the Ca^{2+}-sensitive fluorescent dye, fura-2 acetoxymethyl (AM), which permeates cell membranes as an ester and is hydrolyzed in the cell to its Ca^{2+}-sensitive acidic form. Fluorescence for the adherent cells is measured over time with cells that have been washed free of extracellular dye. Free $[Ca^{2+}]$ is estimated as described below (see *Image and Data Processing*).

Description of Microscope and Imaging Setup

1. The microscope is an automated Olympus IX81 with a 0.30 NA 10X UPLANFl air objective.
2. The excitation light source is a TILL monochromator polychrome IV with a 150 Watt xenon bulb. Excitation wavelengths (340 nm and 380 nm) are delivered to the back of the microscope via a TILL condenser.
3. A fura filter cube with 400 long pass dichroic and D510/40m emission band pass is used.
4. A cooled charge-coupled-device (CCD) camera is attached to the Yokagawa head for image acquisition.
5. Hardware control and image acquisition are performed with Metafluor software.

Loading Cells with Intracellular Free Calcium Indicator Fura-2 AM

6. Plate RAW 264.7 cells at 4 x 10^4 cells/well of an 8-well coverglass one day prior to experiment. In the case of a duplex RNAi transfection experiment or lentivirus-infected cell plating, density is adjusted to that similar to uninfected cells. Duplex RNAi-transfected cells can be plated up to two days prior to the experiment.
7. Incubate plated cells at 37 °C in air and 5% CO_2 for 18 to 24 hr.
8. Wash cells once with Hanks' balanced salt solution-bovine serum albumin with 2.5 mM probenecid, pH 7.45, low LPS (HBSS-BSA-probenecid, low LPS).
9. Remove most of the buffer from each well.
10. Add 200 μl of 5 μM fura-2 AM solution to each well. Incubate the plate in the dark at room temperature (21 °C) for 30 min.
11. Wash all the wells once with HBSS-BSS-probenecid, low LPS. Wash the well to be assayed immediately four more times. Leave 300 μl of the same buffer in well.

Description of Acquisition Parameters

12. Twelve-bit images (intensity values of 0 to 4095) are acquired with the camera binning set to 2 x 2. This, combined with the 10X objective and 6.5 x 6.5 μm CCD chip pixel dimensions, results in images that have pixel dimensions of 1.3 x 1.3 μm.
13. Camera exposure time is usually set to 250 msec and 200 msec for images excited at 340 and 380 nm, respectively. Specific exposure times may vary, and these are tracked in the database.

14. A field of about 100 to 1000 evenly distributed cells is selected for the assay.
15. The assay is typically a 21-min time series during which a baseline is collected for the first minute. Images are acquired every second during ligand stimulation and every 5 sec during calibration.
16. A 100 μl solution of ligand (4X) is added gently to the well 1 min after the start of the time series.
17. At 10 min after ligand addition, 100 μl of single-cell Rmin solution is added. Single-cell Rmin solution is a 5X stock that, when diluted, results in 10 μM of thapsigargin and 1 μM of ionomycin to release calcium from intracellular stores and 2 mM of EGTA to chelate extracellular calcium.
18. Five min after the addition of the Rmin solution, 200 μl of single-cell Rmax solution is added to the well. The time series is continued for the next 5 min. Single-cell Rmax solution is a 3.5X stock of calcium chloride ($CaCl_2$) so that the final concentration of external calcium will be 25 mM in order to raise intracellular calcium and obtain the Rmax value.

Image and Data Processing

19. Using the Metafluor software, a region of the image is selected to represent the background and assigned as the first region of interest (ROI).
20. Another ROI containing the whole field is assigned as the second ROI. This ROI represents the average response of all the cells.
21. ROIs are drawn around each cell.
22. The average value of the background region is subtracted from each plane of the experimental time series, and each image is separately thresholded to identify bright pixels. Thresholds of 10 and 40 are typically used for the 340 and 380 nm excitation images, respectively.
23. Average intensities at 340 and 380 nm excitation and the 340/380 ratio for each cell are measured. Calcium is estimated using the following equation.

    $$[Ca^{2+}] = K_d * \frac{S_f}{S_b} * \frac{R - R_{\min}}{R_{\max} - R}$$

    Where the K_d of fura-2 for Ca^{2+} is assumed to be 250 nM (Ross PE, Ehring GR, Cahalan MD. JCB. 1997 Sep 8;138(5):987-98); S_f is the maximum value at 380 nm; S_b is the minimum value at 380 nm; R is the measured ratio; R_{min} is the ratio value measured in the presence of store depletion and external EGTA; and R_{max} is the ratio value measured under saturating Ca^{2+}.

    See Grynkiewicz G, Poenie M, Tsien RY. (JBC. 1985 Mar 25;260(6):3440-50) for a complete derivation and explanation of the equation.
24. A perl script converts the ratio values to estimated calcium concentration and removes cells that have unexpected values (e.g., ratio values that drop to 0).
25. Both the raw log files that contain all the measured values as well as the parsed files are uploaded to the Web site to be used by others.

Reagents and Materials

Motorized microscope stand: Olympus, Inc.; model number IX81

U-plan fluorite 10X objective: Olympus, Inc.; catalog no. 1-UB523

Monochromator: TILL Photonics GmbH; catalog no. Polychrome IV

Fura-2 filter cube: Chroma Technology Corp.; catalog no. 71000

Cooled CCD camera, Photometrics CoolSNAP HQ: Roper Scientific; catalog no. CoolSNAP HQ

Image acquisition and analysis software, the latest version of Metafluor: Universal Imaging Corp.; catalog no. 31290

2.4 GHz Pentium IV computer manufactured by Omni Tech Corporation with 1 GigaByte of RAM: Universal Imaging Corp.; catalog nos. OT3020, OT3510, OT3810

Hanks' balanced salt solution-bovine serum albumin with 2.5 mM probenecid, pH 7.45, low LPS (HBSS-BSA-probenecid, pH 7.45, low LPS): AfCS Solution Protocol ID PS00000589

Fura-2 acetoxymethyl (AM), 5 µM: AfCS Solution Protocol ID PS00000592

Rmin solution, single cell: AfCS Solution Protocol ID PS00000587

Rmax solution, single cell: AfCS Solution Protocol ID PS00000622

Author: Grischa Chandy and Mary Verghese

Date: 2/20/04

Approved: Grischa Chandy

C.2 Calibration solutions

Because of problems with small hydrophobic molecules leeching into the PDMS, I had to alter the “min” and “max” calibration buffers for use within PDMS microfluidic devices.

Start with 96.5 μl of HBP. Add 0.5 μl each of 10 mM ionomycin (Calbiochem #407950), 1 mM thapsigargin (Calbiochem #586005), and 10 mM A23187 (Sigma-Aldrich #C7522). Mix and split into two aliquots of 49 μl each.

To one aliquot, add 1.25 μl 500 mM EGTA. This is the “min” calibration solution.

To the other aliquot, add 0.9 μl 2 M $CaCl_2$. This is the “max” calibration solution.

Concentrations of all reagents involved are quite a bit higher than in the AfCS protocols (§C.1).

Both solutions are perfused during experiments, so that the EGTA essentially never mixes with the exogenously added Ca^{2+}, and hence the pH of the solutions should remain mostly constant throughout.